

NONLINEAR RHEOLOGICAL CHARACTERIZATION AND MODELING OF
COMPLEX FLUIDS UNDER LARGE AMPLITUDE OSCILLATORY SHEAR (LAOS)

By

Christopher Joseph Hershey

A DISSERTATION

Submitted to
Michigan State University
in partial fulfillment of the requirements
for the degree of

Chemical Engineering – Doctor of Philosophy

2018

ABSTRACT

NONLINEAR RHEOLOGICAL CHARACTERIZATION AND MODELING OF COMPLEX FLUIDS UNDER LARGE AMPLITUDE OSCILLATORY SHEAR (LAOS)

By

Christopher Joseph Hershey

Dynamic oscillatory shear tests have historically been one of the most common ways a rheologist probes the material response for complex fluid systems including neat polymer melts and solutions, blends, and composites. In small angle oscillatory shear (SAOS) testing, the material functions G' and G'' describe the linear viscoelasticity of the complex fluid and may be related to the morphological changes occurring in the system. However, typical processing conditions occur at fast flow rates and generate large deformations resulting in a strain dependence on the rheological properties.

In this research, the nonlinear viscoelastic behavior of polypropylene (PP) nanocomposite melts and oligomer modified polyamide (PA) blends under large amplitude oscillatory shear (LAOS) flows was investigated using Fourier transform (FT) rheology and stress decomposition (SD) techniques. With the development of high performance data acquisition (DAQ) cards in recent years, raw voltages of angular displacement (strain) and torque (stress) from the rheometer may be Fourier transformed into discrete harmonics to probe a material's nonlinear response. These higher order harmonics are strongly correlated to the chain dynamics and morphological changes in a polymer system.

Polypropylene-clay nanocomposites were produced using concentrations of 3 and 5 wt% of silane treated nanoclay to ensure that the system was dilute, and the filler-network contribution was negligible. To promote particle-polymer interactions, the silane treated clay was reacted with a maleated polypropylene compatibilizer. The nonlinear intensity ratio $I_{3/1}$ of the third order

harmonic to the first order harmonic of the shear stress as well as the zero-strain limit nonlinearity parameter Q_0 were determined through FT rheology experiments. To describe the trends in $I_{3/1}$ and Q_0 for polymer nanocomposite systems, a nonlinear viscoelastic differential model was developed for LAOS type flows.

Blends consisting of a PA6/PA66 copolymer in an 80:20 mixture by weight were melt mixed with varying concentrations (5 and 10 wt%) and molecular weights ($M_w = 750$ and 1000) of an elastomeric polyisobutylene succinic anhydride (PIBSA) oligomer and tested under LAOS conditions. The low molecular weight PIBSA acts as a plasticizer on the matrix blend, reducing its shear stress with increasing concentration. The SD technique separates the elastic (σ') and viscous (σ'') contributions of the stress waveform, much like G' and G'' in SAOS flows. It was found that by increasing the concentration of PIBSA, the normally viscous response of the PA blend matrix transitioned to an elastic response. By combining SD with FT rheology, it was found that the $I_{3/1}$ ratio were nearly identical for both PA blends with 0wt% and 5wt% PIBSA, while much larger values of $I_{3/1}$ were identified for 10wt% PIBSA blends at lower strains.

Copyright by
CHRISTOPHER JOSEPH HERSHEY
2018

DEDICATED
TO
MY PARENTS & GRANDMA

ACKNOWLEDGMENTS

I have been very fortunate during my time here at Michigan State University for the education that I received during both my undergraduate and graduate studies, the lifelong friends that I have made and the memories that we have shared. There have been many individuals that have impacted my life in such a tremendous way, for whom without I would not be where I am today. I must first thank my academic advisor, Dr. K. Jayaraman, for encouraging me to pursue my ideas and challenging me to be a better researcher. If I had not met him during my time as an undergraduate research assistant, my life may have taken me in a direction away from the polymer sciences, a field which I can say I truly love. Thank you, Dr. Jay, for taking me on as your student then and for sticking with me to the very end.

I would like to thank my committee members, Dr. A. Lee, Dr. R. Averill, and Dr. D. Liu, for their suggestions and teachings during my graduate career. I would also like to take the time to thank my colleagues, Weijie, who took the time to help me get acclimated to the research group, and Xinting and Xing, whom provided me with valuable insight through the discussions we have shared. I would like to thank Mike Rich for his counsel and sharing with me many wonderful stories. I am especially thankful to the CHEMS office staff, who keep the department running smoothly. I am also very grateful for my closest friends, Jacob, Steve, Mike and Joel, whom I have memories with that will last a lifetime and stories that will last two.

I want to give my deepest love and thanks to my family. My Mom, Dad and Grandma have always instilled the value of education in me. They have always pushed me to be the best person that I can be and have supported me in all of my endeavors. It is to them that I dedicate this dissertation as a symbol of my love and appreciation for everything they have done.

TABLE OF CONTENTS

LIST OF TABLES	ix
LIST OF FIGURES	x
CHAPTER 1	1
INTRODUCTION	1
1.1 Research Background and Motivation.....	1
1.2 Dynamics of Entangled Polymer Chains	3
1.3 Dynamics of Polymer Composites.....	6
1.4 Dynamic Shear Rheology	8
1.5 Research Objectives.....	14
1.6 Scope of Thesis	15
CHAPTER 2	18
NONLINEAR CHARACTERIZATION TECHNIQUES USING LARGE AMPLITUDE OSCILLATORY SHEAR FLOW	18
2.1 Introduction.....	18
2.2 Data Acquisition	18
2.3 Pre-Processing.....	24
2.4 Post-Processing – Representative Figures	27
2.4.1 Lissajous-Bowditch Curves	28
2.4.2 Fourier Transform Rheology	29
2.4.3 Stress Decomposition.....	32
2.5 Conclusions.....	33
CHAPTER 3	34
DYNAMICS OF ENTANGLED POLYMER CHAINS WITH NANOPARTICLES ATTACHMENT UNDER LARGE AMPLITUDE OSCILLATORY SHEAR (LAOS)	34
3.1 Introduction.....	34
3.2 Theory	37
3.2.1 Model for Polymer Nanocomposites	37
3.2.2 LAOS Simulation Scheme.....	40
3.2.3 Asymptotic Analysis for $Q_0(\omega)$	41
3.3 Results and Discussion	43
3.3.1 Linear Viscoelasticity	43
3.3.2 LAOS Strain Sweeps	45
3.3.3 $Q_0(\omega)$ Asymptotic Solution	56
3.4 Conclusions.....	62

CHAPTER 4	65
FOURIER TRANSFORM RHEOLOGY OF POLYPROPYLENE-LAYERED SILICATE NANOCOMPOSITES	65
4.1 Introduction.....	65
4.2 Experimental.....	67
4.2.1 Materials	67
4.2.2 Sample Preparation	68
4.2.3 Linear Rheology.....	68
4.2.4 Nonlinear Rheology	69
4.2.5 Fourier Transform Rheology	69
4.3 Results and Discussion	72
4.3.1 Dynamic Frequency Sweep Tests	72
4.3.2 Fourier Transform Rheology	73
4.4 Conclusions.....	82
 CHAPTER 5	 83
EFFECTS OF REACTIVE OLIGOMER ADDITIVES ON MELT RHEOLOGY OF NYLONS: FOURIER TRANSFORM RHEOLOGY	83
5.1 Introduction.....	83
5.2 Experimental.....	84
5.2.1 Materials	84
5.2.2 Blend Preparation.....	84
5.2.3 Dynamic Shear Rheology	84
5.2.4 Nonlinear Analysis.....	85
5.3 Results and Discussion	85
5.3.1 Linear Viscoelasticity	85
5.3.2 Nonlinear Viscoelasticity.....	86
5.4 Conclusions and Recommendations	91
 CHAPTER 6	 92
CONCLUSIONS AND RECOMMENDATIONS	92
6.1 Conclusions.....	92
6.2 Recommendations.....	95
 BIBLIOGRAPHY.....	 97

LIST OF TABLES

Table 1.1	Voltage ranges for 2K FRTN1 torque transducer equipped to ARES rheometer..	21
Table 3.1	Relationship between De^{ij} and De for each entanglement pair	43
Table 3.2	Definition of r^{ij} for each free and attached chain entanglement pair	57
Table 4.1	Formulations for Different Nanocomposites	68

LIST OF FIGURES

Figure 1.1	Schematic of reptation theory showing test chain in a tube entangled with matrix chains	4
Figure 1.2	Schematic of stress relaxation test and relaxation regimes with corresponding relaxation timescales	5
Figure 1.3	Dynamic shear tests using (a) frequency sweeps and (b) strain sweeps	8
Figure 1.4	Methods to quantify nonlinearities in (a) strain and stress waveforms using (b) Lissajous-Bowditch curves (c) FT rheology and (d) stress decomposition techniques	10
Figure 1.5	Schematic showing trends found in Lissajous-Bowditch curves.....	11
Figure 2.1	Illustration of a typical rheometer designed for testing LAOS flows	19
Figure 2.2	Rear panel connections for TA Instruments ARES-Classic rheometer	21
Figure 2.3	Raw voltages of torque and angular displacement for an entire LAOS test.....	24
Figure 2.4	Schematic illustrating the effect of oversampling number on a noisy waveform..	25
Figure 2.5	Oversampled and clipped stress and strain waveforms of polypropylene homopolymer at $\gamma_0 = 1.56$ and 1 rad/s.....	27
Figure 2.6	Lissajous-Bowditch curves for polypropylene at 1 rad/s showing effect of strain on viscoelasticity and steady-state behavior	28
Figure 2.7	Fourier intensity spectrum for polypropylene at 1 rad/s and $\gamma_0=1.56$ showing (a) correct (b) low and (c) high oversampling numbers	30
Figure 2.8	FT rheology parameters for polypropylene at 1 rad/s showing (a) $I_{3/1}$ and (b) Q	31
Figure 2.9	Elastic and viscous stress waveforms relative to total stress waveform for polypropylene at 1 rad/s and $\gamma_0=1.56$	33
Figure 3.1	Asymptotic solutions for linear viscoelastic storage modulus with (a) varying strength of attachment c and fixed $\phi_a = 0.1$; (b) varying volume fraction of attached chains ϕ_a and fixed $c = 20$	44

Figure 3.2	Numerical predictions of dynamic storage modulus with strain amplitude and $\beta^a = \beta^f = 1$ for (a) matrix; (b) composite with $\phi_a = 0.1$ and $c = 5$; (c) composite with $\phi_a = 0.1$ and $c = 20$	47
Figure 3.3	Numerical predictions of $I_{3/1}$ with strain amplitude and $\beta^a = \beta^f = 1$ for (a) matrix; (b) composite with $\phi_a = 0.1$ and $c = 5$; (c) composite with $\phi_a = 0.1$ and $c = 20$.	48
Figure 3.4	Numerical predictions of Q with strain amplitude and $\beta^a = \beta^f = 1$ for (a) matrix; (b) composite with $\phi_a = 0.1$ and $c = 5$; (c) composite with $\phi_a = 0.1$ and $c = 20$.	50
Figure 3.5	Effect of uniform CCR rates for composites with $\phi_a = 0.1$ and $c = 20$ at $De = 0.2$ on (a) $I_{3/1}$; (b) Q . Stretch parameters: $r^a = r^f = 0.01$ and $b^a = b^f = 100$	51
Figure 3.6	$I_{3/1}$ predicted with (a) $\beta^a > \beta^f$ and (b) $\beta^a < \beta^f$ for nanocomposites with $\phi_a = 0.1$ and $c = 20$ at $De = 0.2$	53
Figure 3.7	Predicted Q with $\beta^a < \beta^f$ and $\beta^a > \beta^f$ for composites with $\phi_a = 0.1$ and $c = 20$ at $De = 0.2$	54
Figure 3.8	Component stresses with increasing strain amplitude and $\beta^a > \beta^f$ for composites with $\phi_a = 0.1$ and $c = 20$ at $De = 0.2$ showing (a) normalized storage modulus; (b) third harmonic ratio.....	55
Figure 3.9	Asymptotic solutions of Q_0 showing effect of c for $\phi_a = 0.1$ and $\beta^a = \beta^f = 1$. Results of simulations are also plotted for comparison	58
Figure 3.10	Comparison of Q_0 plots obtained from linear averaging (Equation 3.1) and double reptation (Equation 3.4) mixing rules for composites with $\phi_a = 0.1$, $c = 20$ and $\beta^a = \beta^f = 1$	59
Figure 3.11	Asymptotic solution of Q_0 for $c = 20$ and (a) uniform CCR rates, $\beta^f = \beta^a = 1$ and (b) independent CCR rates, $\beta^f = 1$, $\beta^a = 5$	60
Figure 3.12	The low De maximum of Q_0 relative to the high De plateau of Q_0 for $c = 20$ with (a) uniform CCR rates, varying $\beta^a = \beta^f$ and (b) independent CCR rates, varying β^a with fixed $\beta^f = 1$	62
Figure 4.1	(a) Storage modulus and (b) loss modulus of nanocomposites with varying loading and the matrix	73
Figure 4.2	Dynamic storage modulus for composites and matrix at 200°C for (a) 1 rad/s with corresponding (b) $I_{3/1}$ parameter (c) Q parameter and (d) relative intensities acquired using FT rheology at $\gamma_0 = 0.8$. Relative intensities shift factors are 1, 10, 100 for PP, PPNC3, and PPNC5, respectively	74

Figure 4.3	Dynamic storage modulus against strain amplitude at various frequencies for (a) matrix (b) 3wt% clay nanocomposite and (c) 5wt% clay nanocomposite.....	76
Figure 4.4	Relative third harmonic ratio against strain amplitude at various frequencies for (a) matrix (b) 3wt% clay nanocomposite and (c) 5wt% clay nanocomposite.....	78
Figure 4.5	Nonlinear parameter Q against strain amplitude at various frequencies for (a) matrix (b) 3wt% clay nanocomposite and (c) 5wt% clay nanocomposite	80
Figure 4.6	Frequency dependence of $Q_0 \equiv Q(\gamma_0=0.5)$ for nanocomposites and matrix	81
Figure 5.1	Dynamic storage modulus comparing effect of oligomer addition	86
Figure 5.2	Lissajous curves with corresponding elastic stresses for varying oligomer concentration and strain amplitude at (a) $\omega = 0.1$ rad/s, and (b) $\omega = 1$ rad/s	87
Figure 5.3	Elastic and viscous stress waveforms at $\gamma_0=1.14$ and $\omega=1$ rad/s for (a) nylon copolymer matrix (b) 5 wt% oligomer and (c) 10 wt% oligomer.....	88
Figure 5.4	Normalized elastic stress against strain amplitude for $\omega = 1$ rad/s.....	89
Figure 5.5	Effect of oligomer addition on the nonlinear $I_{3/1}$ parameter for $\omega = 1$ rad/s	90

CHAPTER 1

INTRODUCTION

1.1 Research Background and Motivation

Rheology describes the flow and deformation of a material under an applied mechanical force. It is the branch of physics which acts as a bridge connecting fluid and solid continuum mechanics. This encompasses a breadth of materials from liquids to solids particularly to complex fluids such as polymer melts. Understanding the rheology of a material proves invaluable for the manufacturing everyday goods.

The manufacturing of plastic parts through polymer processing involve a variety of methods such as injection molding, extrusion, compression molding, film blowing, film casting and thermoforming. Processing temperature, speed and part size are some of the most important parameters controlling the final quality of the part. Polymer melts are highly sensitive to processing temperature through their viscosity. With increasing temperatures, viscosity decreases resulting in less resistance to flow and faster flow rates. Speed and dimension are directly related to the rate of deformation (strain rate) and deformation amplitude (strain), respectively.

Polymer melts are viscoelastic fluids, meaning that their stress response is both viscous and elastic in nature. In a purely viscous response, stress grows proportionally to the applied strain rate; a purely elastic response show stress growth proportional with strain amplitude. When a material undergoes a deformation, the molecules or atoms making up that material need time to conform. In other words, each material has a characteristic structural relaxation time. For Newtonian fluids, such as water, the relaxation time is much faster than the time scale associated with the strain rate leading to a purely viscous response. Conversely for elastic solids, such as

metals, the relaxation time is very long leading to a purely elastic response. Due to the molecular weight, topology and entanglements in polymer melts, the structural relaxation times are on the order of the deformation rate. Purely viscous and elastic responses are classified as linear responses since the stress grows proportional to the strain rate and strain, respectively. The same linear response behavior is observed in viscoelastic materials when both the strain rate and strain are small. However, when the strain deformation or strain rate is large enough to disrupt the equilibrium structure of the polymer chains, then a deformation dependent material response is observed: the nonlinear viscoelastic region[1].

The linear viscoelastic region may be probed by a rheologist through various shear flow tests on a rheometer when the deformation and rate are kept small. These include steady tests such as steady shear, stress relaxation and creep, as well as dynamic tests (oscillatory shear) such as frequency and strain sweep tests. Material functions such as the plateau modulus, G_N^0 , shear stress relaxation modulus, $G(t)$, creep compliance, $J(t)$, zero-shear viscosity, η_0 and the dynamic storage, G' and loss, G'' moduli are all obtainable through at least one of these tests. These parameters may then be used to determine features such as the polymer characteristic relaxation times, molecular weight and even polydispersity[2].

Dynamic shear strain sweep tests operate by compressing a material between two parallel plates or similar shear geometry in a rheometer. One plate is then subjected to an excitation deformation at a set frequency, while the resulting stress is measured on the other plate. From the stress-strain relationship, the dynamic moduli are obtained and as the deformation increases from small strains to large strains, these moduli become dependent on the strain amplitude marking the onset of nonlinearity and hence the nonlinear region. This particular test probes what is now known as large amplitude oscillatory shear (LAOS) flows[3, 4]. Over the past 20 years, rheologists

have begun to investigate the nonlinear region through LAOS[5]. Before LAOS, the nonlinear region was only described qualitatively with an increase/decrease in G' described as strain stiffening/softening and an increase/decrease in G'' as strain thickening/thinning. Now quantitative interpretations of LAOS flows through Fourier transform (FT) rheology[6-14] and stress decomposition (SD) methods[15-18] have been developed. These methods have frequently cited in the literature for systems including: neat polymers[12], branch-type polymers[8, 9, 12], blends[19-21], and composites[6, 7, 20, 22-24].

However, interpretations of LAOS flows using FT rheology and SD methods are still in their early stages. While the method development has been refined extensively in the literature for various types of systems, the quantity and variety of these systems is lacking. Particularly the area of polymer nanocomposites, a class of viscoelastic materials highly utilized in industry. What literature that does exist are concerned primarily with highly loaded nanocomposites[6, 7, 25], where the nonlinear response is dominated by particle-particle interactions. Therefore, this research focuses on dilute nanocomposites where particle-polymer interactions govern the rheology and nonlinear response. This also requires the development of nonlinear viscoelastic constitutive models for polymer nanocomposites to relate the nonlinear response to particle-polymer chain dynamics.

1.2 Dynamics of Entangled Polymer Chains

The dynamics associated with entangled polymer melts are considered here. The dynamics of polymers are well represented by reptation-based tube models[26]. Reptation of polymers, originally proposed by de Gennes[27] and later refined by Doi and Edwards[28-31], was developed to describe the diffusive motion of a polymer chain, i.e. “primitive chain”, around a

series of obstacles. These obstacles, made up of other polymer chains, form entanglements with the primitive chain to create a temporary cage, i.e. “tube”. A schematic is shown in Figure 1.1.

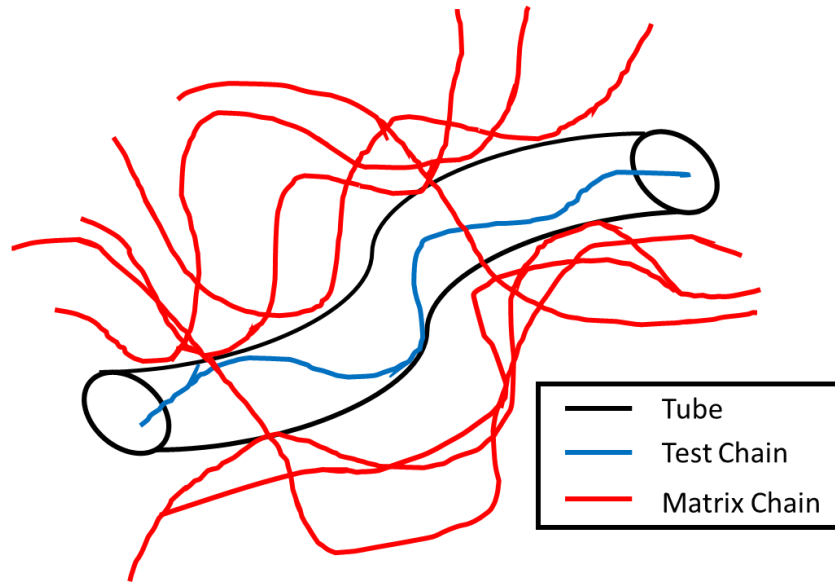


Figure 1.1 Schematic of reptation theory showing test chain in a tube entangled with matrix chains.

The number of entanglements and rate at which they are removed dictate the stress relaxation behavior of the polymer chain. For linear, entangled monodisperse polymer chains, several stress relaxation mechanisms occur in the linear viscoelastic region: Rouse motions, reptation and constraint release[26]. The effect that these relaxation mechanisms have on the stress relaxation is best presented using a steady shear stress relaxation master curve shown in Figure 1.2.

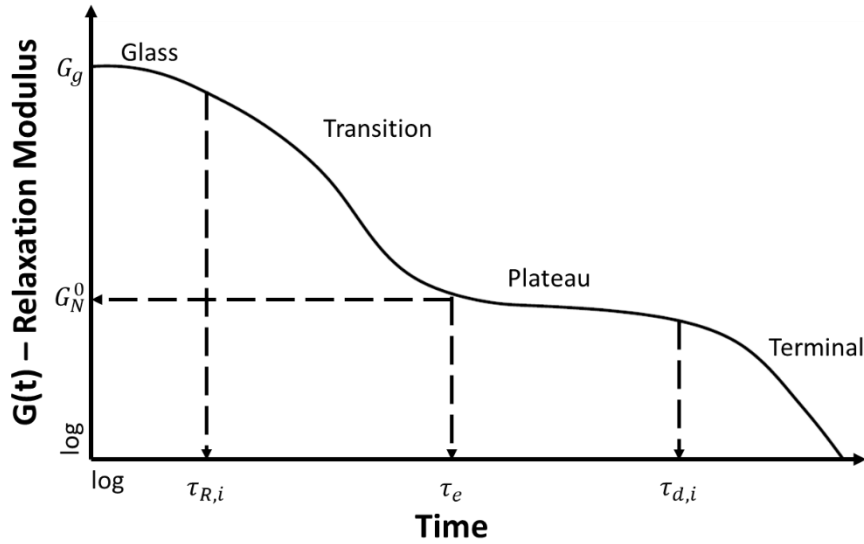


Figure 1.2 Schematic of stress relaxation test and relaxation regimes with corresponding relaxation timescales.

When an instantaneous strain deformation is applied to the sample, an increase in the stress (shear modulus) is observed and the relaxation is recorded over time. At very short times, polymer chains are frozen and behave as a glass for which this region is appropriately named the glassy region. The glass transition region marks the onset of stress relaxation through Rouse motions of chain segments, or fast thermal vibrations, having a distribution of very short Rouse relaxation times τ_R . At the equilibration time which is twice the longest Rouse time, $\tau_e = 2\tau_R$, test chain segments begin to enter the “tube” described by tube theory resulting in the aptly named plateau region, characterized by the plateau modulus G_N^0 for which all polymer chains are now highly entangled with adjacent polymer chains. Given enough time, polymers enter the terminal region whereby the chains diffuse out of their tube through large thermal motions. This relaxation mechanism is reptation and is characterized by the reptation or disengagement time, τ_D , until all remaining stress is relaxed. An additional linear mechanism, constraint release (double reptation), considers both the reptation of the primitive chain as well as the surrounding matrix chains which

form the entanglements. With constraint release, the reptation timescale is reduced resulting in faster stress relaxation and an earlier onset in terminal behavior.

When the strain deformation is large, additional nonlinear relaxation mechanisms are present: convective constraint release and chain retraction after stretching. Due to the velocity gradient in simple shear flows, tube entanglements flow at different rates due to their position along neighboring streamlines. The inclusion of convective constraint release (CCR) reduces the polymer stress by removing these entanglements at a rate proportional to the shear rate[32]. The result is a plateau in the shear stress with increasing shear rate, unlike the original Doi-Edwards model which predicted that stress would go through a maximum leading to excessive shear thinning. In extensional flow, CCR is less significant since there is no gradient along the streamlines[26]. Instead, chains are subjected to stretching, leading to their stress buildup. Only after chains have retracted to their equilibrium length are they then able to reptate out of their tube. Large amplitude shear flows are able to stretch chains to some degree, though not as severely as extensional flows. In comparison with Figure 1.2, the faster relaxing chain retraction mechanism occurs on the order of Rouse times, while the CCR effect would be observed in the terminal region.

1.3 Dynamics of Polymer Composites

Polymer composites are heterogenous mixtures consisting of at least a polymer matrix and a filler material. Common fillers include fibers (one-dimensional), platelet particles (two-dimensional) and spherical particles (three-dimensional). The filler type, concentration, size, shape, and chemical compatibility with the polymer matrix are all factors which affect the rheology of composites[33]. Composites are desired in commercial products for their increased toughness and large strength-to-weight ratio as well as their flame retardancy and improved barrier properties[34].

Three types of interactions are present in polymer composites which lead to their desired mechanical properties: particle-particle, particle-polymer, and polymer-polymer[33, 35]. Particle-particle interactions are prominent in highly loaded systems where the filler content is high and the interparticle spacing between particles are small leading to a percolated filler network[36]. These interactions also exist if the interparticle spacing is small enough to allow attachment of polymer chains between two separate particles i.e. bridging. Once a filler network forms, a sharp liquid-to-solid transition is present, forcing the viscoelastic properties to become elastic-dominant. In dynamic shear rheology, this effect is marked by an increase in the storage modulus (elastic response) at low frequencies relative to the unfilled polymer matrix[33]. The chain confinement of the polymer matrix between the filler particles lead to hindered mobility and thus longer relaxation times resulting in a loss of the observable terminal region. Since the inverse of time is frequency, the long-time terminal behavior for steady shear in Fig. 1.2 corresponds with the low frequency terminal behavior in dynamic shear tests.

Dilute polymer composites are able to have a similar rheological response to filler network systems through strong particle-polymer interactions. Surface modification of the filler surface can create attachment sites for the polymer matrix resulting in particle-attached chains with reduced mobility. Some filler types, such as montmorillonite clay, exist naturally with free oxygen and hydroxyl groups which provide the basis for chemical attachment. Further silylation of these layered-silicate fillers have been shown to react both covalently with the hydroxyl groups and through hydrogen bonding with the oxygen groups on the clay edges and faces, respectively[37, 38]. Improvements in nanocomposite properties have been shown using an amine functionalized silane[38, 39], which are able to further react to long chain maleated polypropylene result in attached chains with hindered mobility as characterized by an increase in the low frequency

dynamic moduli. In addition to the reduced chain mobility, the large molecular weight of the maleated polypropylene compatibilizer created entanglements with the free polypropylene matrix chains.

Reduced relaxation dynamics in filler networks and entanglement networks between particle-attached chains and free chains are also accompanied by a smaller linear viscoelastic processing window. At large deformations and deformation rates, the networks break down resulting in strain softening (decreased elastic response) of the material. This is known as the Payne effect for the breakdown of filler networks, though more recently it has been used to describe the breakup of particle-attached entanglement networks[40].

1.4 Dynamic Shear Rheology

Dynamic (oscillatory) shear rheology determines both the viscous and elastic material response using an oscillatory excitation force at a desired strain amplitude γ_0 and frequency ω ,

$$\gamma = \gamma_0 \sin(\omega t) \quad (1.1)$$

The most common tests include frequency sweeps (constant strain amplitude, varied frequency) and strain sweeps (constant frequency, varied strain amplitude). Illustrative examples of these tests are shown in Figure 1.3.

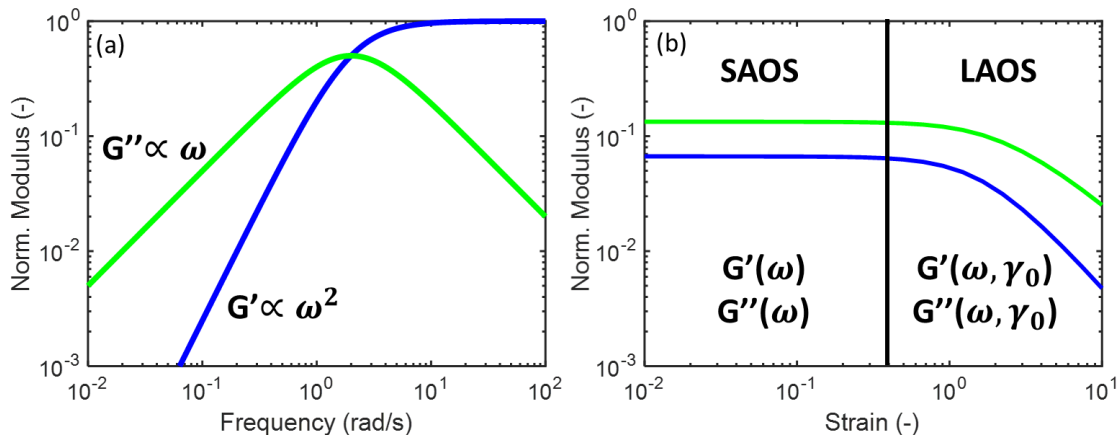


Figure 1.3 Dynamic shear tests using (a) frequency sweeps and (b) strain sweeps.

Frequency sweeps shown in Figure 1.3(a) are useful in identifying the relaxation rates associated with reptation mechanisms. As mentioned earlier, the disengagement time, τ_d , is the timescale by which stress is relaxed through reptative motions. In steady shear relaxation, for times greater than the reptation time, the terminal regime is observed. Similarly, this terminal region is observed in dynamic shear tests at low frequencies i.e. the inverse of long scale reptation times. The terminal region is easily identified by the quadratic scaling of storage modulus, G' with frequency (i.e. $G' \propto \omega^2$) and the linear scaling of the loss modulus, G'' , with frequency (i.e. $G'' \propto \omega$). While frequency sweep tests occur over a range of frequencies, the strain amplitude is kept small ensuring the sample is tested in the linear region. The linear region is identified through strain sweep tests depicted in Figure 1.3(b). At a fixed frequency, the material undergoes a series of increasing deformations. The linear region is associated with a strain independent behavior in the viscoelastic moduli. At a critical strain, the moduli eventually show a strain dependence and either decrease or increase in magnitude, depending on the type of material. This strain marks the onset of nonlinearity and it is a useful measure to separate out the linear and nonlinear regimes. Recent literature in dynamic shear rheology concerning strain sweep tests have coined the term small angle oscillatory shear (SAOS) and large amplitude oscillatory shear (LAOS) for linear and nonlinear testing, respectively[5].

During both SAOS and LAOS testing, oscillatory deformations following Equation 1.1 are applied and the resulting shear stress is determined,

$$\sigma = \sum_{n,odd} \sigma_n \sin(n\omega t + \delta_n) \quad (1.2)$$

Where σ_n and δ_n are the Fourier transform amplitude and phase angles for the n harmonic. In the linear viscoelastic regime (SAOS) only the first harmonic ($n = 1$) is present. During LAOS flows, the nonlinear relaxation mechanisms described in the previous sections lead to increases in the

higher order harmonics which are quantified by FT rheology using Equation 1.2. Before the designation of LAOS flows, measurements of the nonlinear response were limited to a rheometer effectively reporting only the first harmonic in stress across all strain amplitudes. This restricted the rheologist to only qualitatively identify strain stiffening/softening (G' increase/decrease) and shear thickening/thinning (G'' increase/decrease) behavior as well as determine the onset of nonlinearity for a given material. Relations to the structural morphology of the system were limited. However, in recent years, LAOS flows are accompanied by qualitative, quantitative, and semi-quantitative techniques such as Lissajous-Bowditch analysis, Fourier transform (FT) rheology and stress decomposition. Examples of these analyses are given in Figure 1.4.

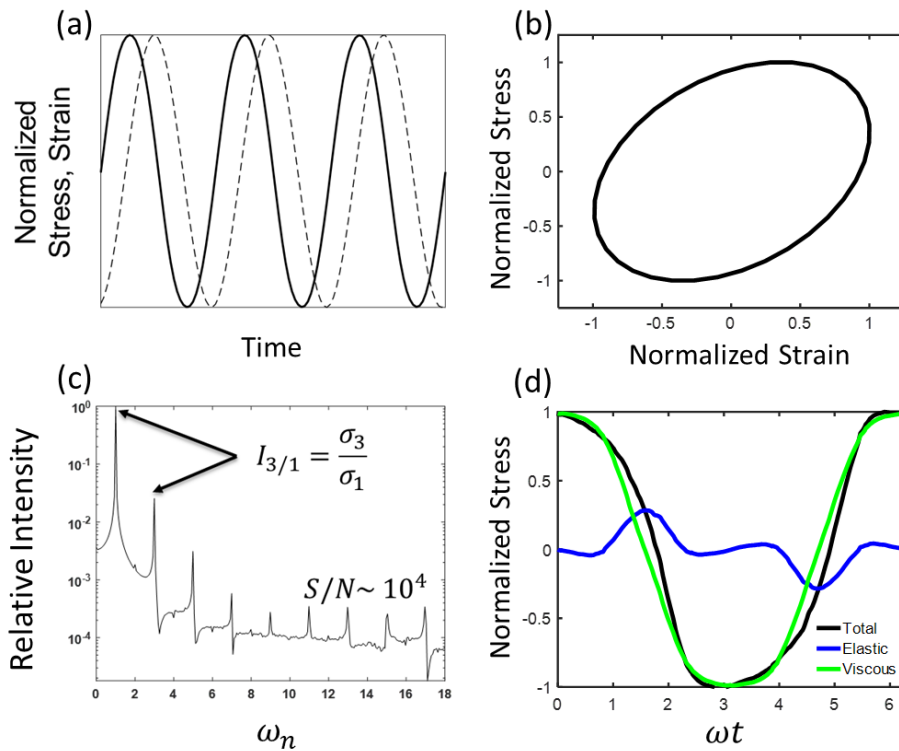


Figure 1.4 Methods to quantify nonlinearities in (a) strain and stress waveforms using (b) Lissajous-Bowditch curves (c) FT rheology and (d) stress decomposition techniques.

A brief overview concerning the types of LAOS techniques is presented here, with a more complete discussion given in Chapter 2. An essential component for any LAOS test are the strain

and stress waveforms from the rheometer during testing depicted in Figure 1.4(a). Obtaining these waveforms from a rheometer using the raw voltages of torque and angular displacement through a high-speed data acquisition (DAQ) card has been the standard implementation in literature[11, 13, 14]. In more recent years, commercial rheometers provided by companies such as TA instruments and Anton-Paar, have incorporated LAOS test procedures directly into their software.

Plotting the normalized stress waveform against the normalized strain waveform yield the qualitative Lissajous-Bowditch curves in Figure 1.4(b). The shape of these curves are useful in determining the type of response the material undergoes during deformation. They can go from completely circular (purely viscous) to ellipsoidal (viscoelastic) to a straight line (purely elastic) as seen in Figure 1.5.

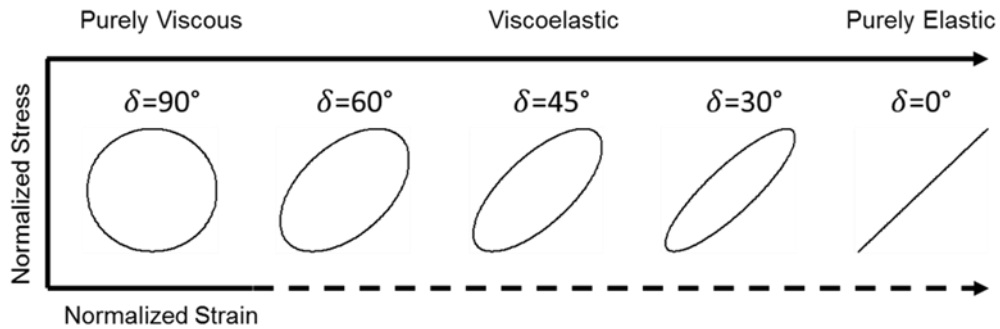


Figure 1.5 Schematic showing trends found in Lissajous-Bowditch curves.

An equivalent measure of viscoelasticity is provided in SAOS tests by using δ_1 , the first harmonic phase angle. Additional nonlinearities at large deformations due to microstructural changes[8, 12, 41], entanglement and filler network breakup[25, 42], or even systematic errors due to wall slip and edge fracture are all picked up through Lissajous-Bowditch curves. A requirement for additional LAOS analyses, such as FT rheology, is the acquisition of oscillatory data at steady

state. Lissajous-Bowditch curves provide a useful measure in the steady-state response since a transient response (i.e. decaying amplitude with time) lead to spiral curves instead of closed loops.

Fourier transform rheology is the interpretation of higher order harmonics in the stress waveform at large deformations. Fourier transformation translates the time-dependent stress response into a frequency-dependent stress response at each strain amplitude. The result are intensities or stress amplitudes σ_n corresponding to the higher order harmonics, which are some integer multiple of the fundamental testing frequency i.e. the frequency imposed by the rheometer. An example of the intensity plot from FT rheology is given in Figure 1.4(c). Stress is an odd function of strain (i.e. $\sigma(\gamma_0) = -\sigma(-\gamma_0)$) resulting in the observance of only odd harmonics. By normalizing the intensities with respect to the first harmonic, a relative intensity at each harmonic is obtained with the largest corresponding to the third harmonic, $I_{3/1}$. This parameter is a characteristic measure of FT rheology and is the basis for all other nonlinear parameters such as $Q(\omega, \gamma_0)$ and the zero-strain intrinsic nonlinearity $Q_0(\omega)$ [10]. More details are provided in Chapter 2 regarding these parameters.

The onset of nonlinearity has been loosely defined in FT rheology to occur at the strain amplitude where the value of $I_{3/1}$ is greater than 0.5% of stress response (i.e. $I_{3/1} > 0.005$)[5]. This is the direct result of a major limitation in FT rheology: electronic noise. By definition, the SAOS regime should only have first harmonic contributions to the stress when the strain amplitude is kept low. For most polymer melts and solutions these low strains lead to low stresses (i.e. low voltages) which are more susceptible to electronic noise generated by the torque transducer. Fourier transformation of the noise can lead to erroneous data and an incorrect interpretation in the LAOS behavior. Thus, a requirement for FT rheology is the oversampling of the raw voltage waveforms[11]. Oversampling is an averaging technique used in combination with high-speed

DAQ cards and multiple oscillation cycles per strain. By averaging several thousand data points per second or more depending on the testing frequency and DAQ rate, the signal-to-noise (S/N) ratio can be significantly improved after Fourier transforming the stress waveform. An S/N ratio of 10,000 is observed in Figure 1.4(c), which is typical for polymer melts, while polymer solutions can have S/N ratios as high as 100,000[13].

Stress decomposition is the final LAOS technique discussed in this section. In SAOS dynamic testing, the stress waveform is decomposed into the storage modulus (elastic response) and the loss modulus (viscous response). These responses can be attributed to the magnitude of the phase lag δ_1 since $G' = G^* \cos(\delta_1)$ and $G'' = G^* \sin(\delta_1)$ where $G^* = \sigma_1/\gamma_0$ is the complex modulus. In a purely elastic material, an instantaneous or in-phase stress response is observed upon deformation (i.e. $\delta_1 = 0$) while in a purely viscous material the stress response is completely out-of-phase with the strain deformation (i.e. $\delta_1 = \pi/2$). Thus, the elastic and viscous responses are dependent on the relative position between the stress and strain waveforms. In the nonlinear regime, the stress waveform is no longer sinusoidal resulting in phase angles at higher order harmonics δ_n . Stress decomposition techniques utilize this nonlinear phase lag to decompose the stress waveform into elastic and viscous contributions as shown in Figure 1.4(d). This was first done geometrically by Cho et. al.[15] and later a mathematical derivation using orthogonal Chebyshev polynomials was applied by Ewoldt et. al.[17]. The linear viscoelastic moduli are recovered via SD techniques; however a more accurate representation of these moduli are calculated in the nonlinear regime. The nonlinear viscoelastic moduli also hold the same physical meaning as their linear viscoelastic counterparts. Additionally, the example in Figure 1.4(d) show a total stress waveform and viscous waveform being nearly identical in amplitude and phase, suggesting that the material response is viscous dominant. The elastic waveform has a much lower

amplitude and takes on an exotic shape allowing the rheologist to classify the nonlinearity as an elastic or solid-like response.

The LAOS techniques introduced in this section are considered the most useful measures of nonlinear rheology developed to date. While each have their own unique advantages, associating the nonlinear viscoelastic behavior with polymer architecture, morphological changes and chain dynamics still proves challenging due to the relative newness of this field. Therefore, more variety in the systems tested as well as relationships between the nonlinear parameters to chain dynamics through viscoelastic models are much needed.

1.5 Research Objectives

The motivation of this work stems from the lack of experimental and theoretical research concerning large amplitude oscillatory shear flows. Particularly in the area of polymer nanocomposites, where the current research is concerned primarily with highly loaded systems where particle-particle interactions govern the rheology. Dilute nanocomposites with strong particle-polymer interactions have been researched extensively in linear viscoelasticity, though no such research exists concerning nonlinear viscoelasticity under LAOS. This also implies that the dynamics associated with these systems are not well understood in LAOS flows. This research seeks to accomplish the following objectives:

(1) To design and implement LAOS functionality in the current rheometer setup and develop a numerical framework for interpreting LAOS flows using techniques such as Lissajous-Bowditch curves, Fourier transform rheology, and stress decomposition.

(2) To develop a nonlinear viscoelastic model for polymer nanocomposites and relate the dynamics associated with free and attached chain entanglements to the nonlinear trends observed in nonlinear rheology particularly those concerning FT rheology.

(3) To test dilute polymer nanocomposites under LAOS flows to determine the effect of entanglement network breakdown on the nonlinear rheology and relate these effects to dynamics associated with model predictions.

(4) To use FT rheology and stress decomposition methods to determine the elastic effect imparted by low-molecular weight oligomers in polyamide blends.

1.6 Scope of Thesis

This thesis is concerned with the nonlinear viscoelasticity of complex fluids. Particularly, how complex fluids behave under large amplitude oscillatory shear (LAOS) flow. In recent years, LAOS flows have been successfully utilized to relate the observed nonlinearity of polymers, blends and composites to their respective chain dynamics, molecular topology, and structural morphology. Interpretations of LAOS flows are made possible through qualitative and quantitative methods.

The first portion of this thesis (Chapter 2) describes the framework necessary for interpreting LAOS flows. This chapter is applicable to both LAOS flows tested experimentally and those simulated numerically using viscoelastic constitutive models. Firstly, experimental tests require an initial step in the data acquisition of the torque and angular displacement at discrete points in time during strain sweep testing using raw voltages from the rheometer instrument. After data acquisition, the resulting voltages are then converted to their corresponding stress and strain values. This pre-processing step is then followed by post-processing used for both experiments and simulations. Post-processing involve several techniques to interpret LAOS flows for which the algorithms are discussed in detail. Plots of shear stress versus shear strain, known as Lissajous-Bowditch plots, offer a graphical way to evaluate the viscoelasticity of a material as a function of strain and frequency. Additionally, the stress decomposition (SD) technique can further classify

the nonlinear mechanism by decomposing the shear stress component into its viscous and elastic contributions. Finally, the most sensitive method to interpret LAOS flows is by utilizing Fourier transform (FT) rheology. In FT rheology, the time-dependent stress waveform is Fourier transformed into higher order harmonics, giving a quantitative value to the nonlinear behavior.

The second portion of this thesis (Chapters 3-4) is concerned with the dynamics of polymer nanocomposites under LAOS flows. Graphical methods like the Lissajous-Bowditch plots are excellent tools for quickly interpreting the viscoelasticity of a material, however they do little in describing the dynamics of polymer systems. In polymer nanocomposites, the chain dynamics associated with polymer-particle attached chains increase the solid-like (elastic) behavior of the polymer matrix as well as the nonlinearity at large strain amplitudes. This effect is captured by the higher order harmonics in FT rheology. In an effort to relate the nonlinear parameters in FT rheology to the chain dynamics of particle-attached chains, a nonlinear viscoelastic constitutive model was developed. This model, which accounts for entanglement networks formed by free polymer chains and particle-attached chains, is subjected to LAOS flows using both numerical simulations and asymptotic solutions. Chain relaxation mechanisms such as double reptation, convective constraint release, chain stretch, and finite extensibility are all accounted for in the model and are explained in further detail in the next section. Chapter 4 further expands the experimental understanding of polymer layered silicate nanocomposites tested under LAOS flows. With surface treated montmorillonite clay nanofillers reacted to maleated polypropylene chains, particle-polymer chain dynamics are investigated using FT rheology. Furthermore, where most research is concerned with the effect of particle-particle interactions, the systems presented here consist of primarily particle-polymer and polymer-polymer interactions.

The final portion (Chapter 5) investigates the formulation of polyamide blends reacted with a functionalized elastomeric oligomer under LAOS flows. The oligomer of interest is polyisobutylene succinic anhydride (PIBSA). For this research both FT rheology and stress decomposition are utilized to in the nonlinear analysis. In viscoelastic materials, stress relaxation is dependent on both its viscous (energy dissipation) and elastic (energy storage) behavior. In nonlinear rheology, the less dominant component is typically associated with the nonlinear behavior. For polyamides, which are viscous dominant, the degree of nonlinearity is probed by added varying concentrations of the elastic dominant PIBSA. Even with a low molecular weight, variation in PIBSA concentration show distinct transitions in the elastic nonlinear behavior suggesting the possibility of phase separation indicating suitable homogenous blend formulations.

CHAPTER 2

NONLINEAR CHARACTERIZATION TECHNIQUES USING LARGE AMPLITUDE OSCILLATORY SHEAR FLOW

2.1 Introduction

The subject of this thesis is the nonlinear characterization of complex fluids under large amplitude oscillatory shear (LAOS) flows. As the name suggests, LAOS tests involve dynamic testing of a material in a shear rheometer using large amplitude shear deformations. While all dynamic shear rheometers are capable of imposing large strains onto a material, special hardware and software is needed to interpret the nonlinear response. The implementation of the required hardware (i.e. high-speed data acquisition card) and the design of the necessary software are explained in detail here. The software developed for this research was written using MATLAB. Similar packages to interpret LAOS flows include the MITLaos package developed by Ewoldt[43] as well as a LabView implementation designed by Wilhelm[13] and are freely available upon request.

2.2 Data Acquisition

The rheometer used in this study was an ARES-Classic manufactured by TA instruments. It is classified as a separated motor transducer (SMT) rheometer, where the two platens which compress the sample rotate independently from one another; the bottom plate applies the deformation (i.e. strain) while the top plate measures the torque (i.e. stress). A 2K FRTN1 force rebalance torque transducer is equipped capable of measuring torques up to 2000 g-cm as well as simultaneously measuring normal forces during testing. A schematic of the rheometer test setup

as suggested by Wilhelm[13] for LAOS flows is given in Figure 2.1 to help facilitate the discussion.

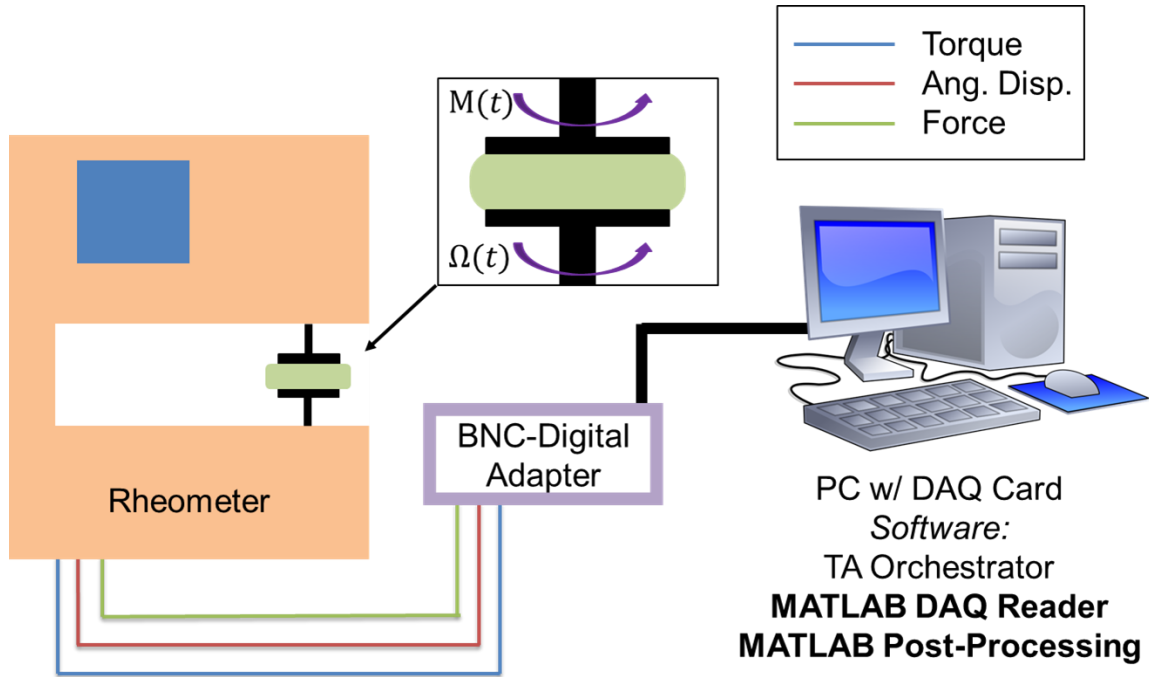


Figure 2.1 Illustration of a typical rheometer designed for testing LAOS flows.

A parallel plate geometry is depicted in Figure 2.1, though any shear geometry may be used for testing LAOS flows. Couette geometries are useful for quantify low viscosity fluids such as dilute polymer solutions. Torsion bars test solid samples that are below the glass transition temperature or at elevated temperatures below the melting point of the sample. Cone and plate and parallel plate geometries are used for the more viscous polymer melts, with the latter being the subject of this research. Giacomini et. al.[44] compared the FT rheology results between cone and plate and parallel plates and found that the nonlinear ratio $I_{3/1}$ for parallel plates needed to be multiplied by $3/2$ to match the nonlinear results of cone and plates. Linear viscoelasticity needs no correction, though care must be taken when comparing nonlinear results.

In order to probe the nonlinear rheology of a sample under LAOS flows using one of the techniques introduced in the previous chapter (i.e. Lissajous-Bowditch, FT rheology and stress decomposition), raw voltages of the angular displacement (i.e. strain) and torque (i.e. stress) waveforms must first be acquired during testing from the rheometer. Several components are required for the acquisition of these waveforms:

- (1) A rheometer capable of outputting voltages of angular displacement and torque through BNC (Bayonet Neill-Concelman) connectors
- (2) Double shielded BNC cables to prevent electronic noise
- (3) An analog-to-digital (A/D) BNC adapter
- (4) High-speed data acquisition (DAQ) card
- (5) A computer with sufficient random-access memory (RAM) installed
- (6) Software for communicating with rheometer, DAQ card and for post-processing LAOS data

For the ARES used in this study, several BNC connections are available on the back-side of the rheometer depicted in Figure 2.2.

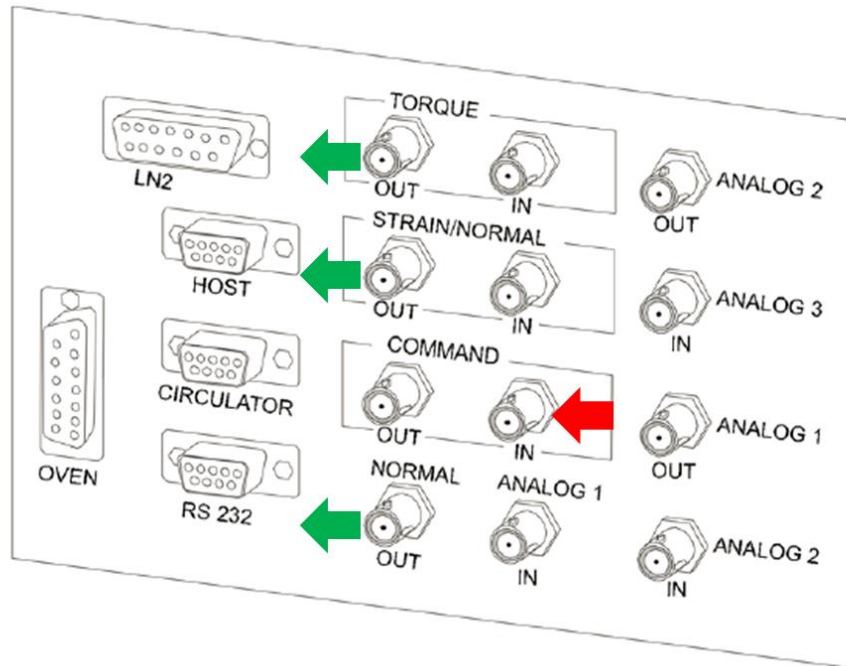


Figure 2.2 Rear panel connections for TA Instruments ARES-Classice rheometer.

Doubled shielded BNC cables were connected to the Torque, Strain and Normal outputs in Figure 2.1. The output voltages for each of these connections are summarized in Table 1.1.

Table 1.1 Voltage ranges for 2K FRTN1 torque transducer equipped to ARES rheometer

Connector	Voltage Range
Strain (angular displacement)	0 Volts = 0 radians, ± 5 Volts = ± 0.5 radians
Low Torque Calibration	0 Volts = 0 g-cm, ± 5 Volts = ± 200 g-cm
High Torque Calibration	0 Volts = 0 g-cm, ± 5 Volts = ± 2000 g-cm
Normal Force	0 Volts = 0 gmf, ± 10 Volts = ± 2000 gmf

Identifying the range of voltages is an important step in the acquisition of accurate LAOS data as these can vary depending on the rheometer and transducer installed. The torque voltages listed in Table 1.1 have two regimes for the 2K FRTN1 transducer: low torque and high torque. The rheometer automatically switches to the appropriate calibration depending on the measured

stress during testing. This will be made more clearly in the next section, though it should be recognized that this transition can create a challenge in separating out the waveforms at individual strains during LAOS post-processing. An additional input in Figure 2.2 labeled “command in” can be used to input a raw voltage corresponding to a strain waveform, adhering to the voltages in Table 1.1. Klein et. al.[45] reconstructed stress data by mathematically superimposing several strain waveforms in the form of sine, rectangular, triangular and sawtooth shapes which were found to correspond to the linear response, strain thinning, shear thickening and wall slip characteristics, respectively. By fitting these responses to the stress waveform, they were able to quantify each linear and nonlinear contribution based on the harmonics from FT rheology. Experimentally, this could be validated by testing these exotic waveforms using the “command in” connection, though this feature was not explored for the work presented in this thesis.

Data acquisition was achieved using a 16-bit resolution high-speed DAQ card (PCIe-6341 X series) by National Instruments with a 100 kS/sec/channel sampling rate (kS = kilo Samples). Resolution determines the number of discrete voltages that can be measured from the rheometer. For a 16-bit resolution, there are 2^{16} measurable voltages for the ranges listed in Table 1.1. Sampling rate controls the number of voltages recorded over time. Early high-speed data acquisition of LAOS flows by van Dusschoten and Wilhelm[11] used a 16-bit resolution DAQ card with a 33 kS/sec/channel sampling rate. The sampling rate they suggested needed to be large enough to allow for oversampling of the data, taking several thousand data points (time, stress, strain etc.) and averaging them into a single data point. Thus a 100 kS/sec sampling rate with an oversampling number of 1000 would generate 100 data points per second. Oversampling serves two purposes: increasing the S/N ratio after Fourier transformation and to decrease file sizes. The former is more important than the latter since large digital storage capacity has become more

affordable in recent years. Oversampling is still reported as an “on-the-fly” process meaning that during testing the data is averaged according to a fixed oversampling number. With larger storage devices and the fact that oversampling and S/N ratios are correlated, it is suggested here that averaging of the waveforms should occur in the pre-processing step outlined in the next section and not during the data acquisition step.

The ARES rheometer is controlled by the TA Orchestrator software while data acquisition was accomplished via MATLAB using the built-in DAQ module. This module is able to communicate directly with the National Instruments DAQ card. Strain sweep tests are defined with the following parameters: frequency, initial strain, final strain, points per decade and cycles before measurement. The total experiment runtime is dependent on frequency, points per decade and the number of cycles as follows,

$$t_{exp}(s) = \frac{2\pi(P+1)(C+1)}{\omega} \quad (2.1)$$

Where ω is the testing frequency, P is the number of points per decade and C is the number of cycles before measurement. The cycles before measurement represent a delay before the final measurement cycle i.e. the cycle used for determining the viscoelastic moduli. The testing time should be evaluated before every test to ensure that the material will remain thermally stable. In addition, file sizes generated from high-speed data acquisition may also be estimated in megabytes,

$$Size (MB) = \frac{8NF_s t_{exp}}{10^6} \quad (2.2)$$

Where N is the number of channels (i.e. time, stress, strain), F_s is the DAQ sampling rate and the prefactor 8 are the number of bytes in a double-precision floating point number. Clearly an increase in the number of strain amplitudes and cycles before measurement lead to larger file sizes, though these offer an increase in resolution and S/N ratios, respectively, for nonlinear analyses. The size of the file may be reduced significantly in the pre-processing stage after oversampling.

2.3 Pre-Processing

The input for pre-processing is a single file containing the angular displacement, torque, and normal force voltages as well as time from a single LAOS test over several strain amplitudes. The pre-processing stage serves three purposes: oversampling the raw data, converting angular displacement and torque into strain and stress, and cropping the waveforms to their corresponding strain amplitudes.

An example of the raw voltage waveforms for a polypropylene homopolymer at 1 rad/s is shown in Figure 2.3.

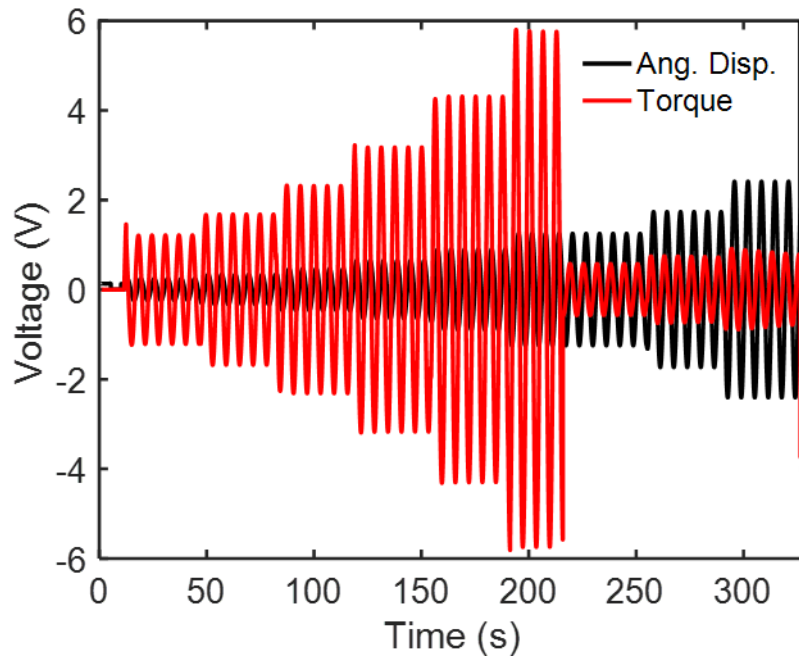


Figure 2.3 Raw voltages of torque and angular displacement for an entire LAOS test.

Inspection of the raw data show two trends that are typical in data collected during LAOS tests. The first is a short dead time which is attributed to the time between starting data collection and beginning the strain sweep test from the TA Orchestrator software. The time at which testing begins is manually recorded and the dead time is trimmed for post-processing. The second feature is a sharp voltage drop in torque at 220 sec. This corresponds to the rheometer switching between

low and high torque calibrations, which is unavoidable. In addition to the voltage drop, the rheometer re-tests the strain amplitude which includes delaying for a set number of cycles, prolonging the experiment. Post-processing is unaffected if the data is trimmed at the point where the high torque calibration occurs. Hence, for raw voltage waveforms similar to Figure 2.3, the low torque and high torque calibrations are post-processed individually.

As it was mentioned earlier, oversampling improves the S/N ratio by averaging over several thousand data points to create a smooth waveform. This is illustrated in Figure 2.4, for a simple sinusoidal waveform generated statistical noise for different oversampling numbers, $No.$,

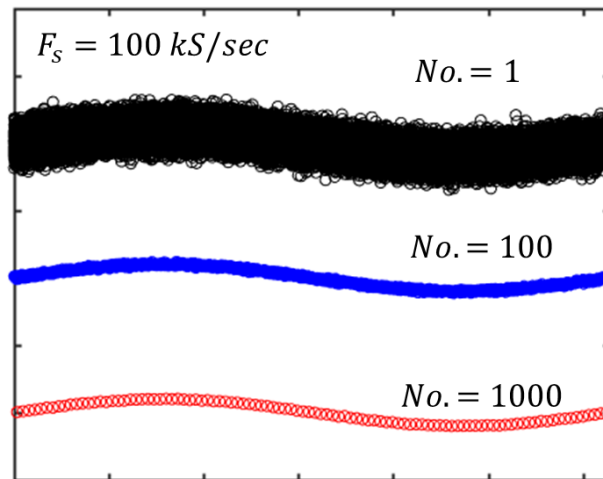


Figure 2.4. Schematic illustrating the effect of oversampling number on a noisy waveform.

All three cases in Figure 2.4 have features characteristic of a sine wave regardless of the amount of noise present. For $No. = 1$, where there is no oversampling, the noise would contribute to higher order harmonics after Fourier transformation preventing the reconstruction of the original sine wave. This noise is almost completely reduced for $No. = 1000$, where the original sine wave is recovered.

When interpreting real data, the choice in oversampling number is not arbitrarily made as in Figure 2.4. Instead, the oversampling number is calculated based on the DAQ rate and excitation frequency,

$$No. \equiv \frac{F_s}{2nf_0} = \frac{\pi F_s}{n\omega_0} \quad (2.3)$$

Where F_s is the DAQ sampling frequency, $\omega_0 = 2\pi f_0$ is the excitation frequency and n is the maximum observable harmonic in the nonlinear spectrum. Due to the harmonic dependence on the oversampling number, the nonlinearity must be approximated before testing if oversampling were to occur “on-the-fly”. By saving the data and oversampling after testing, a range of oversampling numbers can be tested to identify which harmonic generates the greatest S/N ratio.

After oversampling the raw voltages, the data is clipped to individual strain amplitudes and converted from angular displacement and torque to strain and stress. For parallel plates, the conversion of angular displacement θ follows to strain amplitude γ_0 follows,

$$\gamma_0 = \frac{\theta R}{H} \quad (2.4)$$

Where R is the plate radius and H is the gap height. Converting torque M to shear stress σ follows,

$$\sigma = \frac{2MG_c}{\pi R^3} \quad (2.5)$$

Where G_c is the gravitational constant.

Using the example polypropylene shown in Figure 2.3, the converted strain and stress waveforms at $\gamma_0=1.56$ and 1 rad/s are shown in Figure 2.5.

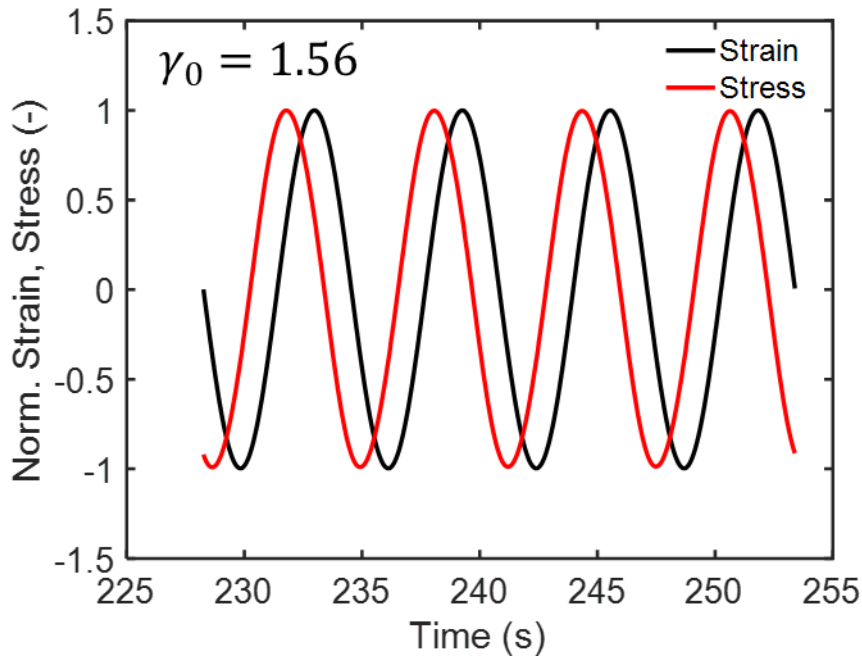


Figure 2.5 Oversampled and clipped stress and strain waveforms of polypropylene homopolymer at $\gamma_0 = 1.56$ and 1 rad/s.

The LAOS test conducted to generate these waveforms was implemented using a 4-cycle delay before measurement with the rheometer running an extra cycle after delay resulting in 5 cycles per strain shown in Figure 2.3. Transitions between increasing strain amplitudes result in the occasional flow instability. Thus, the first cycle is always neglected in LAOS analysis which explains why Figure 2.5 has 4 cycles. Once the waveforms are appropriately scaled with Equations 2.4-2.5 and clipped as in Figure 2.5, each strain is ready for LAOS analysis thus concluding the pre-processing step.

2.4 Post-Processing – Representative Figures

The MATLAB code developed for this research focuses on the three primary analyses for interpreting LAOS flows: Lissajous-Bowditch plots, FT rheology and stress decomposition. This section details the type of curves obtained through the MATLAB code written for this thesis. A full review of these methods is available elsewhere[5].

2.4.1 Lissajous-Bowditch Curves

Lissajous-Bowditch plots are easily prepared by plotting the normalized stress waveform against the strain waveform. They offer a quick qualitative interpretation into the viscoelasticity of a system. Lissajous-Bowditch plots for polypropylene at 1 rad/s at several strains are shown in Figure 2.6.

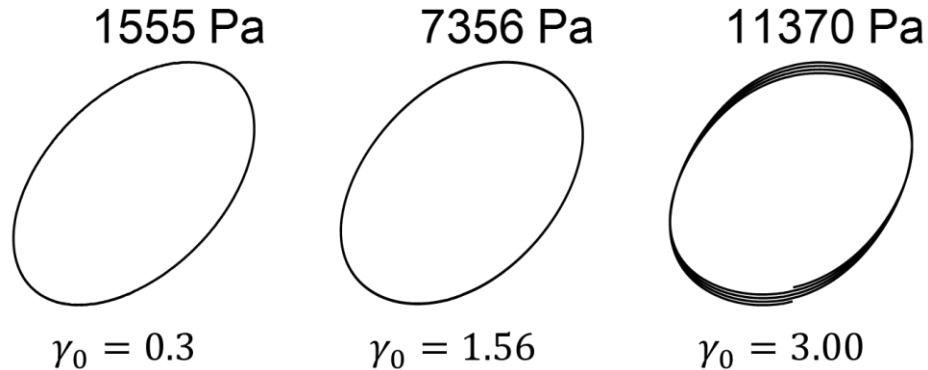


Figure 2.6 Lissajous-Bowditch curves for polypropylene at 1 rad/s showing effect of strain on viscoelasticity and steady-state behavior.

Each strain presented in Figure 2.6 occurs in the LAOS region for this particular polypropylene. From $\gamma_0 = 0.3$ to 1.56 the ellipsoidal shape begins to transition toward a more spherical behavior suggesting a viscous or liquid-like response associated with the disentanglement of chains at large strains. A secondary purpose for Lissajous-Bowditch plots is identifying the steady state behavior of the polymer during testing. Each Lissajous-Bowditch curve in Figure 2.6 is the superposition of 4 deformation cycles. At large strains where $\gamma_0 = 3$, it is clear that a transient behavior is observed. This transient may be due to melt edge fracture or sample drooling and should be neglected in a LAOS analysis such as FT rheology, since the transient behavior will affect the higher order harmonic contributions to stress.

2.4.2 Fourier Transform Rheology

Fourier transform rheology was first introduced nearly two decades ago with the introduction of high speed data acquisition cards and pioneered by Wilhelm. The LabView program written by Wilhelm implemented a discrete Fourier transform (DFT) algorithm to determine the Fourier coefficients and phase angles in Equation 1.2. Similarly, the MATLAB code presented here computes the discrete Fourier transform using MATLAB's fast Fourier transform (FFT) algorithm,

$$Y(k) = \sum_{j=1}^n X(j)e^{(-2\pi i)(j-1)(k-1)/n} \quad (2.6)$$

Where $X(j)$ is a generalized discretized time-domain vector of length n , $Y(k)$ is the corresponding imaginary frequency-domain Fourier spectrum vector. Any imaginary number including $Y(k)$ are generalized to the form $a + bi$ and the complex magnitude of this number yield the corresponding Fourier intensities,

$$I_n = \sqrt{a^2 + b^2} \quad (2.7)$$

With corresponding phase angles,

$$\delta_n = \text{atan}\left(\frac{b}{a}\right) \quad (2.8)$$

To determine the true viscoelastic phase angle, the strain waveform must also be Fourier transformed and the resulting phase angle subtracted from the stress phase angle.

With the Fourier intensities determined from Equation 2.7, the corresponding intensity plots can be constructed as a function of the higher order harmonics. The S/N ratio is evaluated from these figures and are sensitive to the choice in oversampling number. The effect of oversampling number on the Fourier transform intensities are compared for the polypropylene sample at $\gamma_0 = 1.56$ and 1 rad/s in Figure 2.7.

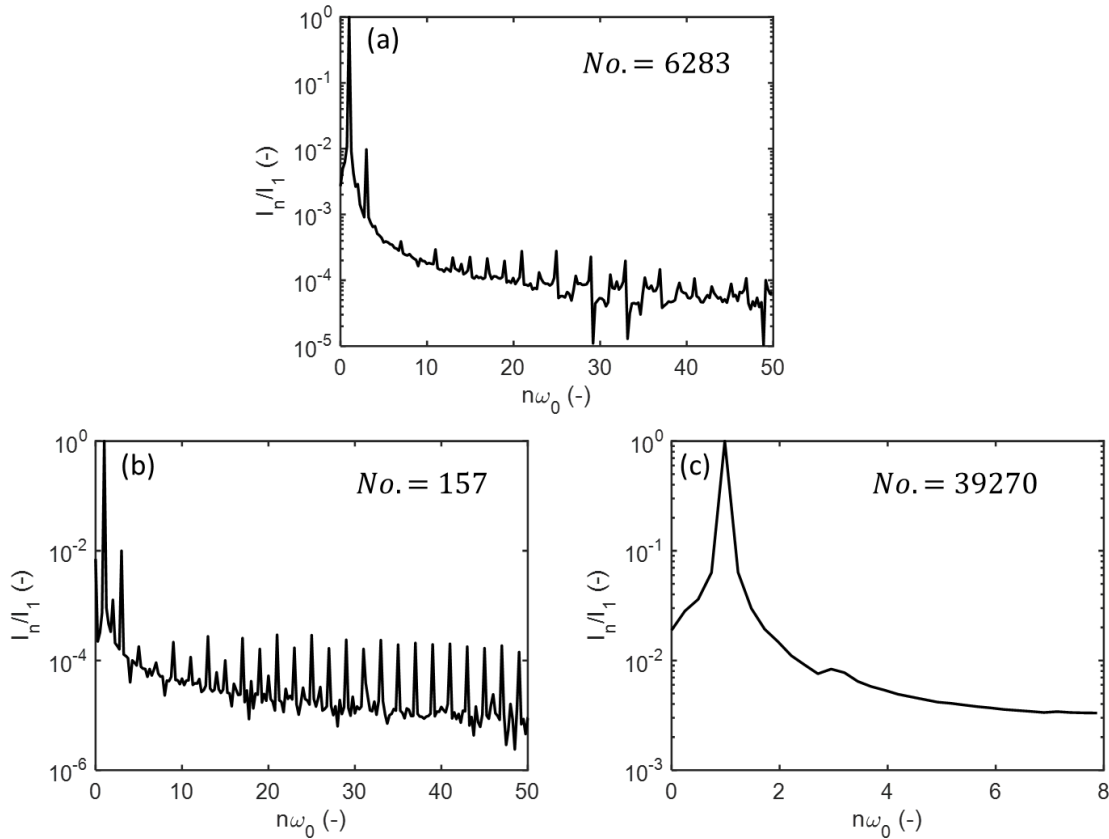


Figure 2.7 Fourier intensity spectrum for polypropylene at 1 rad/s and $\gamma_0=1.56$ showing (a) correct (b) low and (c) high oversampling numbers.

An example of an ideal oversampling number is shown in Figure 2.7(a), where the S/N ratio is 10,000:1, typical of polymer melts. When the oversampling number is too low, as in Figure 2.7(b), the S/N ratio is still quite high, however the presence of many higher harmonics results from the Fourier transform fitting noise instead of the true stress waveform. Conversely, when the oversampling number is too large, as in Fig 2.7(c), the S/N ratio is too low and no distinguishable harmonics are present.

The third harmonic intensity is the largest nonlinear contribution making it an ideal measure for nonlinear rheology. This is the motivation for using the $I_{3/1}$ parameter as a means to quantify structural morphologies and polymer topology. For many neat polymers, $I_{3/1}$ has been shown to increase quadratically with strain amplitude. This feature is also predicted by all

constitutive models. Due to the quadratic nature of $I_{3/1}$, Hyun and Wilhelm formulated a nonlinear parameter Q [10],

$$Q(\omega, \gamma_0) = \frac{I_{3/1}}{\gamma_0^2} \quad (2.9)$$

Since the quadratic dependence of $I_{3/1}$ is normalized in Q , a low strain plateau region is expected resulting in qualitative features similar to the linear viscoelastic moduli (i.e. strain stiffening/softening). By taking the limit of Q at low strains, the strain dependence can be completely removed resulting in a frequency dependent nonlinear parameter known as the zero-strain intrinsic nonlinearity Q_0 ,

$$Q_0(\omega) = \lim_{\gamma_0 \rightarrow 0} Q = \lim_{\gamma_0 \rightarrow 0} \frac{I_{3/1}}{\gamma_0^2} \quad (2.10)$$

The nonlinear parameters $I_{3/1}$, Q and Q_0 are plotted for polypropylene at 1 rad/s in Figure 2.8.

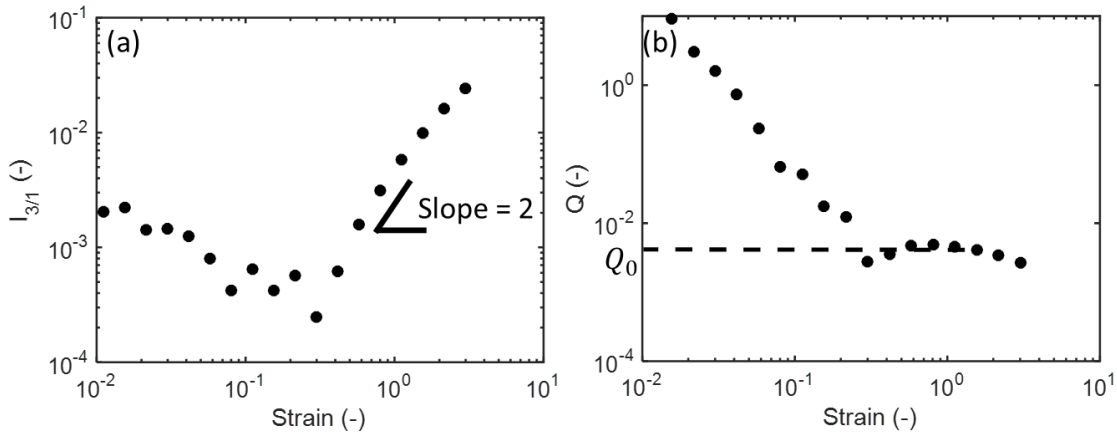


Figure 2.8 FT rheology parameters for polypropylene at 1 rad/s showing (a) $I_{3/1}$ and (b) Q .

Higher order harmonic contributions are by definition zero in the linear viscoelastic limit. The nonlinear harmonic contribution in Figure 2.8(a) at low strains is the result of electronic noise from the rheometer. With increasing strain amplitude, the nonlinearity grows quadratically with strain amplitude indicating the onset of nonlinearity and the start of the LAOS regime at $\gamma_0=0.4$.

Similarly, at this strain a plateau is observed in Q which can be extrapolated to the limit of zero-strain to get a value of the Q_0 parameter.

2.4.3 Stress Decomposition

The final LAOS analysis is a semi-qualitative technique known as stress decomposition where the shear stress is decomposed into elastic and viscous contributions, similar to the linear viscoelastic moduli except applicable to the nonlinear regime. The original description of this technique was done by Cho et. al.[15] and later refined by Ewoldt et. al.[17] through the use of Chebyshev polynomials to calculate the elastic and viscous stresses. An equivalent method for determining these stresses is by using the Fourier coefficients and phase angles from FT rheology[16],

$$\sigma' = \sum_{k=0}^{\infty} I_{2k+1} \cos(\delta_{2k+1}) \sin[(2k + 1)\omega t] \quad (2.11)$$

$$\sigma'' = \sum_{k=0}^{\infty} I_{2k+1} \sin(\delta_{2k+1}) \cos[(2k + 1)\omega t] \quad (2.12)$$

These stresses are compared to the total stress for polypropylene at $\gamma_0 = 1.56$ at 1 rad/s in Figure 2.9. The shape and magnitude of the elastic and viscous stresses relative to the overall shear stress is useful in determining the type of nonlinearity. In Figure 2.9, the overall stress is most closely related to the viscous stress suggesting a liquid like response and the resulting nonlinearity is due to the elastic stress. For more complex systems such as polymer nanocomposites where particle-particle interactions dominate, the elastic and viscous stresses are highly sensitive to the breakup of any filler network that forms[18].

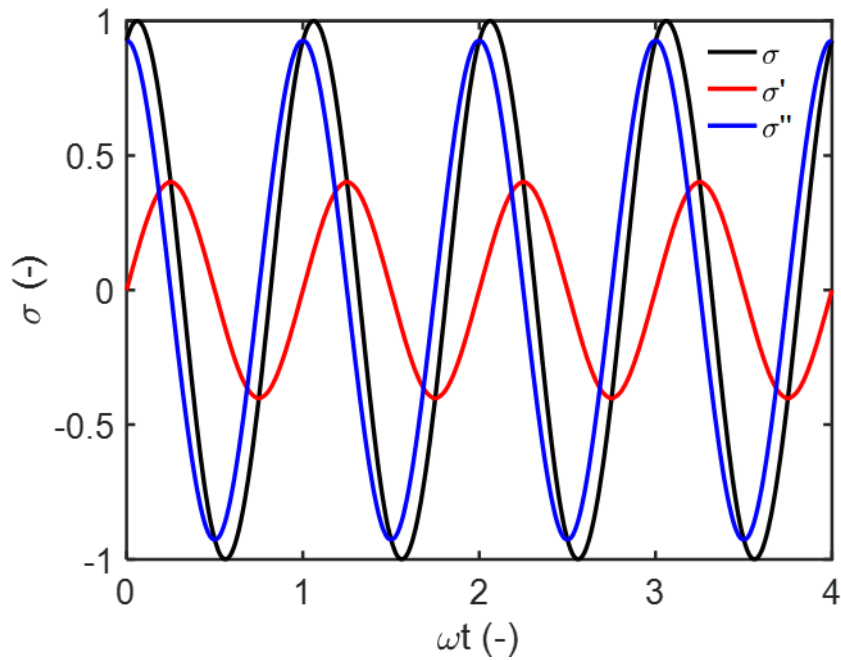


Figure 2.9 Elastic and viscous stress waveforms relative to total stress waveform for polypropylene at 1 rad/s and $\gamma_0=1.56$.

2.5 Conclusions

This chapter focuses on the necessary framework for testing the nonlinear rheology of complex fluids under large amplitude oscillatory shear flows. A rheometer capable of outputting raw voltages of stress and strain has the capability of testing LAOS flows so long as a high-speed data acquisition card is used to collect the data. Faster sampling rates provide a greater S/N ratio which is essential to determine the nonlinearity present in a system. These nonlinearities are interpreted through several techniques such as Lissajous-Bowditch plots, Fourier transform rheology and stress decomposition. The most sensitive method, FT rheology, has been recently cited in the literature as being able to detect structural morphologies, polymer topology such as long chain branching, and even percolation thresholds in polymer nanocomposites.

CHAPTER 3

DYNAMICS OF ENTANGLED POLYMER CHAINS WITH NANOPARTICLES ATTACHMENT UNDER LARGE AMPLITUDE OSCILLATORY SHEAR (LAOS)

3.1 Introduction

The rheology of polymer melts reinforced with nanoparticles is of continued interest[36, 39, 40, 46-49] because of the broad range of potential applications for these materials. In addition to varying the loading of nanoparticles, particle-particle interactions and polymer-particle interactions may be varied producing a variety of structural features with associated rheological signatures. For particle volume fractions above the percolation threshold, a filler network may be formed by direct particle-particle interactions or indirectly through bridging chains between nanoparticle surfaces. The nonlinear viscoelastic behavior of such polymer nanocomposites has been attributed largely to the breakup of the filler networks. Polymer-particle interactions may lead to a shell of adsorbed chains around the particles that have greatly reduced mobility.[50-54] Furthermore, the attached polymer in this shell may be highly stretched.[52] Entanglement networks between free polymer chains and polymer chains attached to nanoparticles are also present.[55] Since polymer chains may be attached to nanoparticles with varying levels of interaction using different coupling agents and at different sites[38, 56, 57] like edges and faces of nanolayers, it is important to understand the contribution that entangled chains attached to nanoparticles make to the rheology of the nanocomposite melts.

When a polymer nanocomposite melt is subjected to large amplitude oscillatory shear (LAOS), the filler network is the first to breakdown leading to a strain amplitude dependence of

the viscoelastic moduli known as the Payne effect.[36, 40, 46] The Payne effect has also been reported in nanocomposites with very low volume fractions of nanoparticles[58] where polymer-particle interactions dominate. The stress response in large amplitude oscillatory flows may be analyzed using Fourier transform (FT) rheology[11, 13, 14] and stress decomposition[15-17, 20, 59] (SD). In FT rheology, the combination of fast data acquisition[14] rates and oversampling[11] allow detection of higher harmonic content in the torque response- in particular the ratio $I_{3/1}$ of the third harmonic to the base harmonic. Hassanabadi et al.[7] have noted that the intensity ratio increases progressively with volume fraction of nanoparticles in an EVA melt; the power law exponent of the intensity ratio against strain amplitude decreases progressively from the value of 2 observed with the unfilled melt. An important point to note here is that the strain amplitude range for LAOS tests on polymer melts in rotational rheometers is limited by the onset of edge fracture. In another paper comparing the responses of polyethylene nanocomposites with carbon nanotube loading below and above the percolation threshold, Ahirwal et al.[6] report different trends in the intrinsic nonlinearity parameter Q_0 with frequency.

The dynamics of entangled polymer chains are well represented by reptation-based tube models.[26] One such model is the Marrucci-Ianniruberto[60] constitutive equation. Reptation of polymers, originally proposed by de Gennes[27] and later refined by Doi and Edwards,[28-31] was developed to describe the diffusive motion of a polymer chain, i.e. “primitive chain”, around a series of obstacles. These obstacles, made up of other polymer chains, form entanglements with the primitive chain to create a temporary cage, i.e. “tube”. The timescale for the primitive chain to diffuse out of the tube is referred to as the reptation time or disengagement time. The primitive chain and tube are progressively longer with increasing molecular weight, resulting in more entanglements and hence longer reptation times. Since the inception of the tube model, additional

relaxation mechanisms have been introduced. Specifically, in the single mode Marrucci-Ianniruberto model, these are: double reptation, convective constraint release (CCR), chain stretch, and finite extensibility effects.

The dynamics of a mixture of free polymer chains and polymer chains attached to nanoparticles has been modeled recently by Sarvestani.[61] The stress was obtained by linear averaging over volume fractions (ϕ) of the two types of chains

$$\boldsymbol{\sigma} = \phi_f \boldsymbol{\sigma}^f + \phi_a \boldsymbol{\sigma}^a \quad (3.1)$$

denoted by the indices f and a . The stress contribution for each type of chain was predicted with a single mode Marrucci-Ianniruberto constitutive equation used to describe the chain dynamics. The relaxation times of the nanoparticle-attached chains were taken to be much greater than those of the free chains. Results of computations were presented to show that disentanglement of the attached chains by convective constraint release (CCR), a mechanism relevant to fast flows, could lead to strong nonlinear viscoelastic effects including the strain softening of the dynamic moduli. The present work seeks to address two limitations of the mixture model presented by Sarvestani.[61] First, linear averaging over volume fraction is inconsistent with the double reptation formulation of the Marrucci-Ianniruberto model required for representing the mixture of chains. Furthermore, the CCR parameter which was assumed to be the same for both types of chains in that work, will in general be different for the two types of chains, as explained in the following sections.

The objective of this paper is to present a different version of the Sarvestani[61] model with FT rheology results from numerical computations as well as an asymptotic analysis for the zero-strain intrinsic nonlinearity parameter Q_0 . This model incorporates (a) an averaging scheme consistent with the double reptation formulation for a mixture of different types of entangled

chains based on types of entanglements and (b) different CCR parameters for the two types of chains in describing the nonlinear viscoelastic response to large amplitude oscillatory shear of nanoparticle filled polymer melts.

3.2 Theory

3.2.1 Model for Polymer Nanocomposites

The entanglement network in polymer nanocomposites arises from a mixture of two chain types: free matrix chains and particle-attached chains. A proper mixing rule is necessary to model the entanglement contribution to the stress. The mixing rule used here for such bi-disperse blends is given in Equation 2.

$$\sigma = \sum_{i,j} \phi_i \phi_j \sigma^{ij} \quad (3.2)$$

A bilinear averaging scheme weighted with the volume fraction of chains ϕ is used for the stress tensor σ^{ij} where the indexing corresponds to the i-th “test” chain entangled with the j-th “tube” chain. Test chains are able to remove entanglements with tube chains by a process known as reptation at a time scale τ_D , the reptation time. Similarly, tube chains undergo the same reptative relaxation mechanism resulting in an additional loss of entanglements with the test chains. The combined loss of entanglements between both test and tube chains through reptation is known as double reptation.[26] The timescale associated with the loss of entanglements through double reptation is given as,

$$\frac{1}{\tau_D^{ij}} = \frac{1}{\tau_D^i} + \frac{1}{\tau_D^j} \quad (3.3)$$

For polymer nanocomposites, the mixing rule in Equation 2 is expanded as follows.

$$\sigma = (1 - \phi_a)^2 \sigma^{ff} + (1 - \phi_a) \phi_a \sigma^{fa} + (1 - \phi_a) \phi_a \sigma^{af} + \phi_a^2 \sigma^{aa} \quad (3.4)$$

where the superscripts i, j have been replaced with f, a to denote free and attached chains, respectively. The free chain volume fraction is taken as $\phi_f = 1 - \phi_a$, where ϕ_a is the volume fraction of attached chains.

The stress tensor, $\boldsymbol{\sigma}^{ij}$ obeys the relation given by Marrucci and Ianniruberto,[60]

$$\boldsymbol{\sigma}^{ij} = 3G_N^0 f^{ij} \mathbf{A}^{ij} \quad (3.5)$$

where G_N^0 is the plateau modulus determined from linear viscoelasticity and \mathbf{A}^{ij} is the coupled orientation-stretch tensor, unique to the Marrucci-Ianniruberto model. For large amplitude flows, chain stretch is likely to occur and thus a complete model should incorporate a finite extensibility parameter[62] f^{ij} ,

$$f^{ij} = \frac{b^i - 1}{b^i - \text{tr} \mathbf{A}^{ij}} \quad (3.6)$$

Here, b^i is comparable to the square of the maximum chain stretch of the i -th chain.

The coupled orientation and chain stretch tensor, \mathbf{A}^{ij} , is solved using the single mode differential Marrucci-Ianniruberto model,

$$\frac{d\mathbf{A}^{ij}}{dt} = \boldsymbol{\kappa} \cdot \mathbf{A}^{ij} + \mathbf{A}^{ij} \cdot \boldsymbol{\kappa}^T - \frac{f^{ij}}{\tau_{or}^{ij}} \left(\mathbf{A}^{ij} - \frac{1}{3} \text{tr} \mathbf{A}^{ij} \mathbf{I} \right) - \frac{1}{3\tau_s^i} (f^{ij} \text{tr} \mathbf{A}^{ij} - 1) \mathbf{I} \quad (3.7)$$

where $\boldsymbol{\kappa}$ is the velocity gradient tensor. The last two terms on the right-hand side of Equation 7 correspond to the reptation and chain stretch relaxation mechanisms, respectively. The characteristic relaxation times are given as the orientation time, τ_{or}^{ij} and the chain stretch relaxation time, τ_s^i . By taking the trace of Equation 7, the chain stretch equation takes the form,

$$\frac{d(\text{tr} \mathbf{A}^{ij})}{dt} = 2\boldsymbol{\kappa} : \mathbf{A}^{ij} - \frac{1}{\tau_s^i} (f^{ij} \text{tr} \mathbf{A}^{ij} - 1) \quad (3.8)$$

From the derivation of the coupled orientation-stretch tensor \mathbf{A}^{ij} , the trace of \mathbf{A}^{ij} is equivalent to the square of chain stretch.[60] For which it is clear that the rate of chain stretch is controlled by the stretch relaxation time.

As a consequence of the mixing rule in Equation 4, the orientation time originally derived by Marrucci and Ianniruberto [60] is modified to take the form,

$$\frac{1}{\tau_{or}^{ij}} = \left(\frac{1}{\tau_D^i} + \frac{1}{\tau_D^j} \right) + \left[\frac{1}{\tau_S^i} - \left(\frac{1}{\tau_D^i} + \frac{1}{\tau_D^j} \right) \right] \frac{\beta^j (f^{ij} tr \mathbf{A}^{ij-1})}{1 + \beta^j (f^{ij} tr \mathbf{A}^{ij-1})} \quad (3.9)$$

where τ_S is the stretch relaxation time and β^j is the CCR parameter for the tube chains.

For small amplitude oscillatory shear (SAOS) flows, the speed and deformation are not sufficient in magnitude to cause chains to stretch (i.e. $tr \mathbf{A}^{ij} \approx 1$) forcing the orientation time in Equation 3.9 to follow the double reptation timescale shown in Equation 3.3. For LAOS flows, chain stretch can occur and the CCR effect, the second term on the right-hand side of Equation 3.9, decreases the orientation time through the removal of entanglements. The rate at which these entanglements are removed is controlled by the CCR parameter. It should be noted that in SAOS flows, where chain stretch does not occur, there is symmetry between free-attached and attached-free entanglements (i.e. $\sigma^{fa} = \sigma^{af}$). This is not necessarily true, however, for LAOS flows as the CCR effect and chain stretch relaxation time in Equation 3.9 may reduce the orientation time at different rates for each entanglement.

In this model characteristic relaxations times were defined as a set of dimensionless quantities,

$$c = \tau_D^a / \tau_D^f \quad (3.10)$$

$$r^f = \tau_S^f / \tau_D^f \quad (3.11)$$

$$r^a = \tau_S^a / \tau_D^f \quad (3.12)$$

$$s = \tau_S^a / \tau_S^f = r^a / r^f \quad (3.13)$$

Here it should be noted ratio of reptation times, c in Equation 3.10, was originally described by Sarvestani [55] and is referred to in this work as the relative strength of attachment, with strong

attachment yielding greater values of c . The quantities in Equations 3.11-3.12 are referred to as the relative stretch times and are related by the parameter s , defined in Equation 3.13.

3.2.2 LAOS Simulation Scheme

The shear stress components, σ_{12}^{ij} , in Equation 3.4 for simple shear flows are calculated using the component forms of Equation 3.7 for each entanglement pair,

$$\frac{dA_{12}^{ij}}{dt} = \omega\gamma_0 \cos(\omega t) A_{22}^{ij} - \frac{f^{ij}A_{12}^{ij}}{\tau_{or}^{ij}} \quad (3.14)$$

$$\frac{dA_{22}^{ij}}{dt} = -\frac{f^{ij}(A_{22}^{ij} - \text{tr}A^{ij}/3)}{\tau_{or}^{ij}} - \frac{f^{ij}\text{tr}A^{ij-1}}{3\tau_S^i} \quad (3.15)$$

$$\frac{d(\text{tr}A^{ij})}{dt} = 2\omega\gamma_0 \cos(\omega t) A_{12}^{ij} - \frac{f^{ij}\text{tr}A^{ij-1}}{\tau_S^i} \quad (3.16)$$

where the orientation time, τ_{or}^{ij} is defined in Equation 3.9.

Two types of simulations are performed: strain sweep tests and frequency sweep tests. Strain sweep tests are conducted to investigate trends at large strains. For low and moderate strains, an asymptotic solution is derived and discussed in the next section. Frequency sweep tests are simulated to validate the asymptotic solution. For both tests, the shear stress component in Equation 3.5 is solved for each entanglement pair by first solving the coupled ordinary differential equations in Equations 3.14-3.16 using MATLAB. The result are four shear stresses, each corresponding to a different entanglement pair, which are combined into a total shear stress according to the mixing rule in Equation 3.4. Using MATLAB's fast Fourier transformation (FFT) package, the total shear stress is evaluated using a Fourier series expansion,[3]

$$\sigma_{12}(t) = \sum_{n,odd} I_n \sin(n\omega t + \delta_n) \quad (3.17)$$

where I_n and δ_n are the Fourier coefficients and phase angles for the n^{th} harmonic, respectively. Representing the stress as a Fourier series as in Equation 3.17 begins the analysis known as Fourier transform (FT) rheology.[13]

Using the first harmonic ($n = 1$), the linear viscoelastic storage modulus, G' and loss modulus G'' are obtained,

$$G'(\omega, \gamma_0) = I_1 \cos(\delta_1) / \gamma_0 \quad (3.18)$$

$$G''(\omega, \gamma_0) = I_1 \sin(\delta_1) / \gamma_0 \quad (3.19)$$

A characteristic measure for FT rheology is the relative third harmonic ratio, $I_{3/1}$, defined as,

$$I_{3/1}(\omega, \gamma_0) \equiv I_3 / I_1 \quad (3.20)$$

The relative third harmonic ratio is reported to scale quadratically with strain,[5, 10] a trend predicted by all constitutive models[63] including the one presented in this work, as will be discussed in a later section.

Noting the quadratic dependence of $I_{3/1}$ with strain, Hyun and Wilhelm[10] derived a nonlinear parameter Q ,

$$Q(\omega, \gamma_0) = I_{3/1} / \gamma_0^2 \quad (3.21)$$

At low strains, Q becomes independent of strain leading to a new nonlinear parameter Q_0 ,

$$Q_0(\omega) \equiv \lim_{\gamma_0 \rightarrow 0} Q(\omega, \gamma_0) = \lim_{\gamma_0 \rightarrow 0} \frac{I_{3/1}(\omega, \gamma_0)}{\gamma_0^2} \quad (3.22)$$

where Q_0 is now referred to as the *zero-strain intrinsic nonlinearity*, a frequency dependent parameter.

3.2.3 Asymptotic Analysis for $Q_0(\omega)$

Since Q_0 is a zero-strain limit parameter, a low strain asymptotic solution is derived by expanding the tensor \mathbf{A}^{ij} using a power series expansion of the strain amplitude, γ_0 ,

$$\mathbf{A}^{ij} = \frac{1}{3}[\mathbf{I} + \mathbf{a}_1^{ij}\gamma_0 + \mathbf{a}_2^{ij}\gamma_0^2 + O(\gamma_0^3)] \quad (3.23)$$

and the chain stretch, which is equivalent to the trace of \mathbf{A}^{ij} , is written as

$$\text{tr}\mathbf{A}^{ij} = 1 + \frac{1}{3}[\text{tr}\mathbf{a}_1^{ij}\gamma_0 + \text{tr}\mathbf{a}_2^{ij}\gamma_0^2 + O(\gamma_0^3)] \quad (3.24)$$

Substitution of Equations 3.23-3.24 into Equations 3.7-3.8 yields a set of differential equations which are solved analytically and substituted into Equation 3.5 to obtain the low strain asymptote of shear stress, $\sigma_{12}^{ij}(t)$ for each entanglement pair.

The real, $I'_{n,ij}$ and imaginary, $I''_{n,ij}$ Fourier components are determined from the stress waveform for the n^{th} harmonic as follows,

$$I'_{n,ij} = \frac{\omega}{\pi} \int_{-\frac{\pi}{\omega}}^{\frac{\pi}{\omega}} \sigma_{12}^{ij}(t) \sin(n\omega t) dt \quad (3.25)$$

$$I''_{n,ij} = \frac{\omega}{\pi} \int_{-\frac{\pi}{\omega}}^{\frac{\pi}{\omega}} \sigma_{12}^{ij}(t) \cos(n\omega t) dt \quad (3.26)$$

The real and imaginary Fourier components in Equations 3.25-3.26 are then combined using the mixing rule in Equation 3.2 for each n -th harmonic,

$$I'_n = \sum_{i,j} \phi_i \phi_j I'_{n,ij} \quad (3.27)$$

$$I''_n = \sum_{i,j} \phi_i \phi_j I''_{n,ij} \quad (3.28)$$

where the storage and loss moduli for each harmonic take the form,

$$G'_n = I'_n / \gamma_0^n \quad (3.29)$$

$$G''_n = I''_n / \gamma_0^n \quad (3.30)$$

Finally, the asymptotic expression for Q_0 is obtained as,

$$Q_0(\omega) = \frac{\sqrt{(I'_3)^2 + (I''_3)^2}}{\sqrt{(I'_1)^2 + (I''_1)^2}} \cdot \frac{1}{\gamma_0^2} \quad (3.31)$$

3.3 Results and Discussion

3.3.1 Linear Viscoelasticity

Linear viscoelastic frequency sweeps are first investigated using an asymptotic analysis as outlined in the previous section. By integrating the shear stress using Equations 3.25-3.26, the real and imaginary first harmonic intensities for the entanglement pairs are obtained as,

$$I'_{1,ij} = \frac{G_N^0 De^{ij^2}}{1+De^{ij^2}} \gamma_0 \quad (3.32)$$

$$I''_{1,ij} = \frac{G_N^0 De^{ij}}{1+De^{ij^2}} \gamma_0 \quad (3.33)$$

where, for generality, the Deborah number, $De^{ij} = \omega \tau_D^{ij}$, is defined using the characteristic timescale for double reptation given in Equation 3.3. It is more convenient and practical to express these numbers in terms of the Deborah number defined with the free chain reptation time, $De = \omega \tau_D^f$. The relationship between De^{ij} and De is given in Table 3.1.

Table 3.1 Relationship between De^{ij} and De for each entanglement pair

	f, f	f, a	a, f	a, a
De^{ij}	$\frac{De}{2}$	$\frac{cDe}{c+1}$	$\frac{cDe}{c+1}$	$\frac{cDe}{2}$

Combining Equation 3.32 with Equations 3.27 and 3.29, the linear viscoelastic storage modulus is given as,

$$\frac{G'_0}{G_N^0} = \sum_{i,j} \frac{\phi_i \phi_j De^{ij^2}}{1+De^{ij^2}} \quad (3.34)$$

An expression for the loss modulus may also be obtained in the same fashion. The storage modulus, which scales quadratically with frequency in the terminal region, is most sensitive to relaxation phenomena and is therefore investigated in this section.

It is evident from Table 3.1 and Equation 3.34 that two parameters govern the trends in the linear viscoelastic storage modulus: the strength of individual chain attachment c and the volume fraction of attached chains ϕ_a . The effects of these parameters on the storage modulus are shown in Figure 3.1.

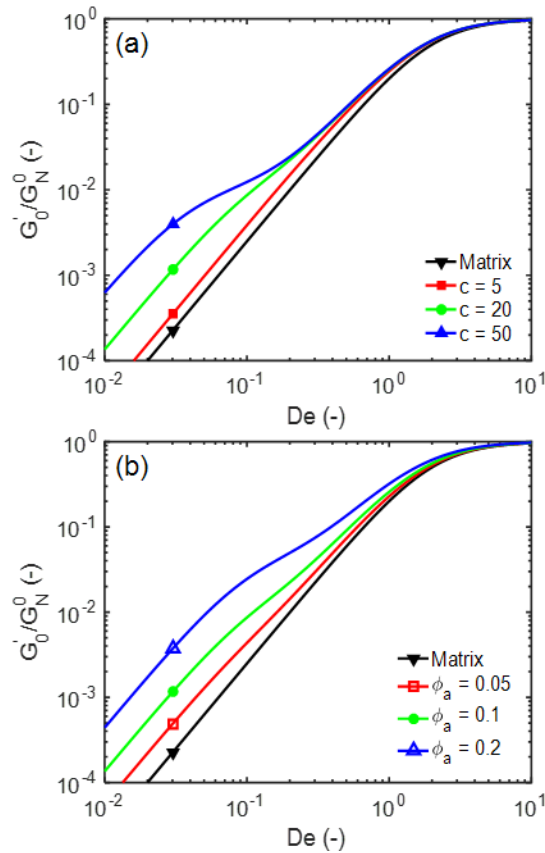


Figure 3.1 Asymptotic solutions for linear viscoelastic storage modulus with (a) varying strength of attachment c and fixed $\phi_a = 0.1$; (b) varying volume fraction of attached chains ϕ_a and fixed $c = 20$.

It is seen from Figure 3.1(a) that with increasing values of c at a fixed value of $\phi_a = 0.1$, an increase in the modulus is observed, particularly at lower frequencies. The increase in modulus for nanocomposites, particularly at low frequencies, is well known for systems where polymer-particle interactions occur. Surface treatment of the filler, which increases the number of active sites for attachment with the matrix, is one method to promote polymer-particle interactions. Figure 3.1(b)

shows that an increase in ϕ_a with a fixed value of $c = 20$, also increases the magnitude of the storage modulus at low frequencies. With increasing values of c and ϕ_a , the “low frequency plateau” in the storage modulus is observed at low Deborah numbers, starting at $De=2/c$. This corresponds to the normalized inverse of the attached chain relaxation time, where the factor of 2 comes from double reptation.

In the next section, the nonlinear viscoelastic regime is discussed where additional nonlinear relaxation mechanisms relax the stress: convective constraint release, chain retraction and finite extensibility.

3.3.2 LAOS Strain Sweeps

Strain sweep simulations conducted using 24 logarithmically spaced strain amplitudes ranging from 0.01 to 10 are tested over varying Deborah numbers. For each strain, 1000 cycles with 2^{16} data points per cycle are simulated. The number of data points per cycle is chosen to improve the signal-to-noise ratio during Fourier transform rheology calculations.[9] The choice in cycle number is necessary to reduce numerical error[8] and validate numerical simulations with asymptotic solutions.

Strain sweep simulations are used to probe the nonlinear behavior of the model. At large amplitudes, several nonlinear relaxation mechanisms occur: CCR, chain stretch and finite extensibility effects. In slow to moderate flows (i.e. $De < 1/\tau_S$), the CCR relaxation has a pronounced effect on the nonlinearity. Uniform CCR rates having $\beta^a = \beta^f$, for both free and attached chains are presented first and followed by independently varying CCR rates, $\beta^a \neq \beta^f$. Chain stretch relaxation and finite extensibility parameters are taken from Marrucci and Ianniruberto[60] as $r^f = r^a = 0.01$ and $b^f = b^a = 100$, respectively, and remained constant for the

analysis of this work. This is a reasonable choice since chains become fully stretched only for flows with $De > 1/\tau_S$, which are not discussed in this work.

Four types of entanglements are present in the system: those in an attached chain environment (i.e. attached and free test chains entangled with attached tube chains) and those in a free chain environment (i.e. attached and free test chains entangled with free tube chains). For uniform CCR rates where $\beta^a = \beta^f$, the stress magnitudes follow: $\sigma^{aa} > \sigma^{af} = \sigma^{fa} > \sigma^{ff}$ where the larger stresses have slower relaxation rates. The equality for mixed chain entanglements may be inferred from orientation time in Equation 3.9 when the reptation, CCR and chain stretch relaxation modes are equivalent. Since these entanglements are indistinguishable, they contribute equally to the overall system stress and nonlinearity.

The strain dependence of the storage modulus for the matrix ($\phi_a = 0$) and two nanocomposites ($\phi_a = 0.1$) having both weak ($c = 5$) and strong ($c = 20$) polymer-particle interactions with for $\beta^a = \beta^f = 1$ is shown in Figure 3.2. For all cases, $De = 1$ has an onset of nonlinearity near $\gamma_0 = 1$ and demonstrates the most intense strain softening effect. For $De = 0.1$, the composites onset are $\gamma_0 = 2$ and 0.5 for $c = 5$ and 20 , respectively, where the matrix onset occurs near $\gamma_0 = 4$. The decrease in onset strain amplitude with increase in particle-polymer attachment is similar to the Payne effect, however for dilute systems the effect is associated with the breakdown of entanglement networks and not a filler network. At low Deborah numbers ($De = 2/c$), the strain softening is due to the breakdown of attached-attached networks. At high Deborah numbers ($De > 2$), all entanglements are lost resulting in the greatest degree of strain softening. To further investigate the nonlinearity in Figure 3.2, the accompanying third harmonic ratio $I_{3/1}$ from FT rheology is presented in Figure 3.3.

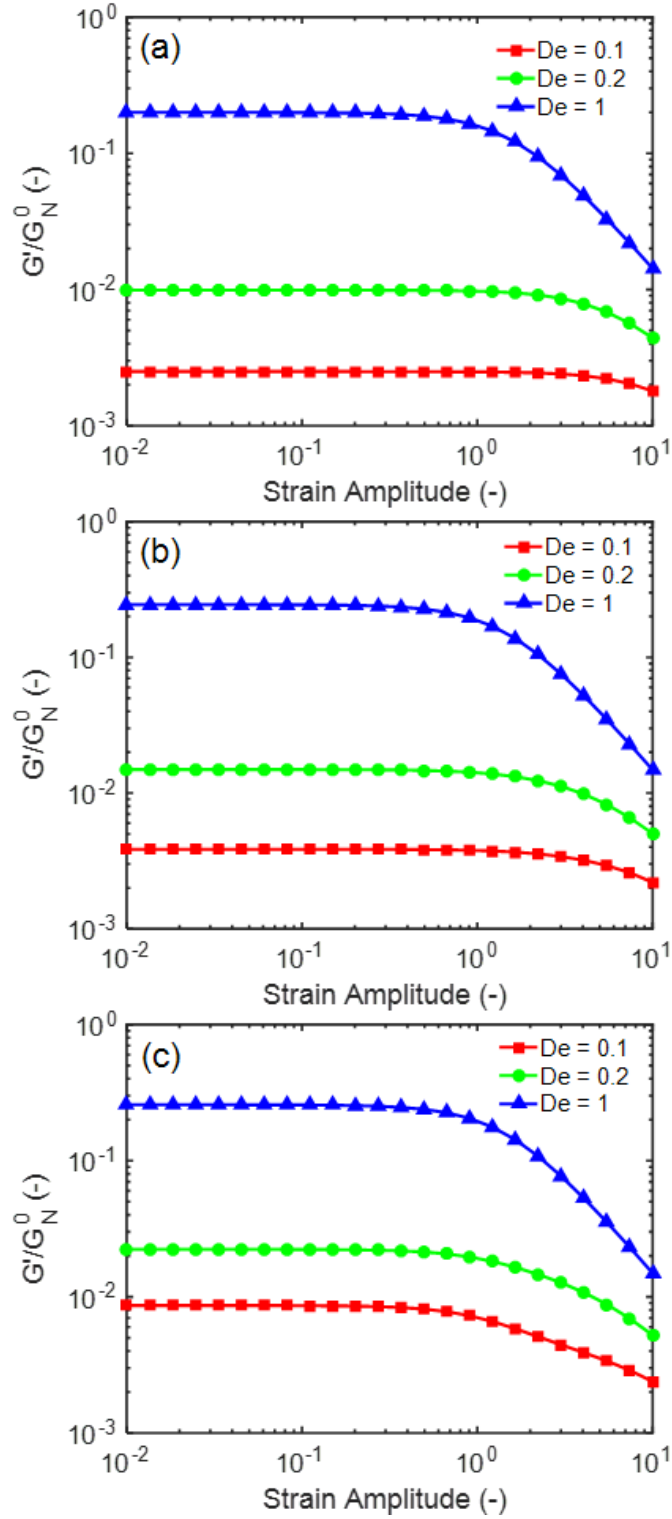


Figure 3.2 Numerical predictions of dynamic storage modulus with strain amplitude and $\beta^a = \beta^f = 1$ for (a) matrix; (b) composite with $\phi_a = 0.1$ and $c = 5$; (c) composite with $\phi_a = 0.1$ and $c = 20$.

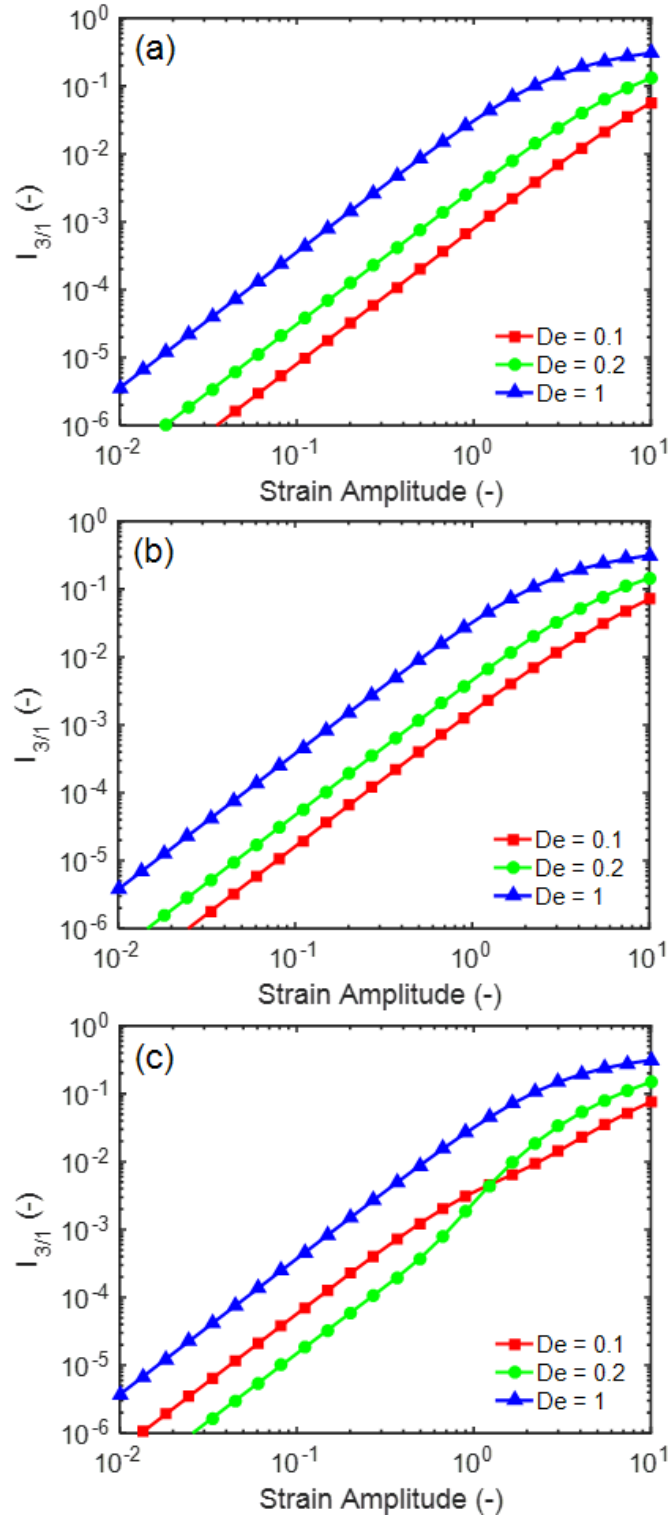


Figure 3.3 Numerical predictions of $I_{3/1}$ with strain amplitude and $\beta^a = \beta^f = 1$ for (a) matrix; (b) composite with $\phi_a = 0.1$ and $c = 5$; (c) composite with $\phi_a = 0.1$ and $c = 20$.

In all cases, the $I_{3/1}$ is shown to scale quadratically with strain amplitude. Deviation from this scaling is considered the onset of nonlinearity,[5] shown in Figure 3.2. Comparing the matrix and $c = 5$ cases, a monotonic increase in the $I_{3/1}$ magnitude with increasing Deborah number is observed, with the value for the composite being slightly greater at all Deborah numbers. A clear reversal in the $I_{3/1}$ trends at $De = 0.1$ and 0.2 for $c = 20$ is shown in Figure 3.3(c). Here, the nonlinearity goes through a minimum at $De = 0.2$ from $De = 0.1$ to 1 for the stronger attachment. The Deborah number where this minimum occurs corresponds to the low De plateau observed from the linear viscoelastic frequency sweeps in Figure 3.1. For $De = 0.2$ in Figure 3.3(c), the nonlinearity deviates from a quadratic scaling with strain amplitude and exhibits a greater power law exponent with strain near $\gamma_0 = 1$ than the matrix and $c = 5$ cases, which still show a power law exponent of 2. The contrast between $c = 20$ and $c = 5$ is more strongly evident in the plots of another nonlinear parameter Q , defined in Equation 3.21 and presented in Figure 3.4.

With increasing strain amplitude, a decrease in Q is observed for all cases except $c = 20$, where instead an overshoot is observed for $De = 0.2$. This overshoot in Q is reported for comb polymers with highly entangled arms experimentally by Hyun and Wilhelm[10] and numerically predicted by Hyun et al.[9] using the pom-pom model. In comb polymers and branched polymers, to which the pom-pom model applies, the backbone can relax substantially only after the branches relax.[27] This is not the case in polymer nanocomposites, where both the attached chain entanglements and free chain entanglements are able to relax simultaneously. Only decreases in Q with strain amplitude have been reported for nanocomposites-- possibly because the LAOS testing was not done in the low frequency region. At this time, more research in the area of nanocomposites is needed to verify trends in Q .

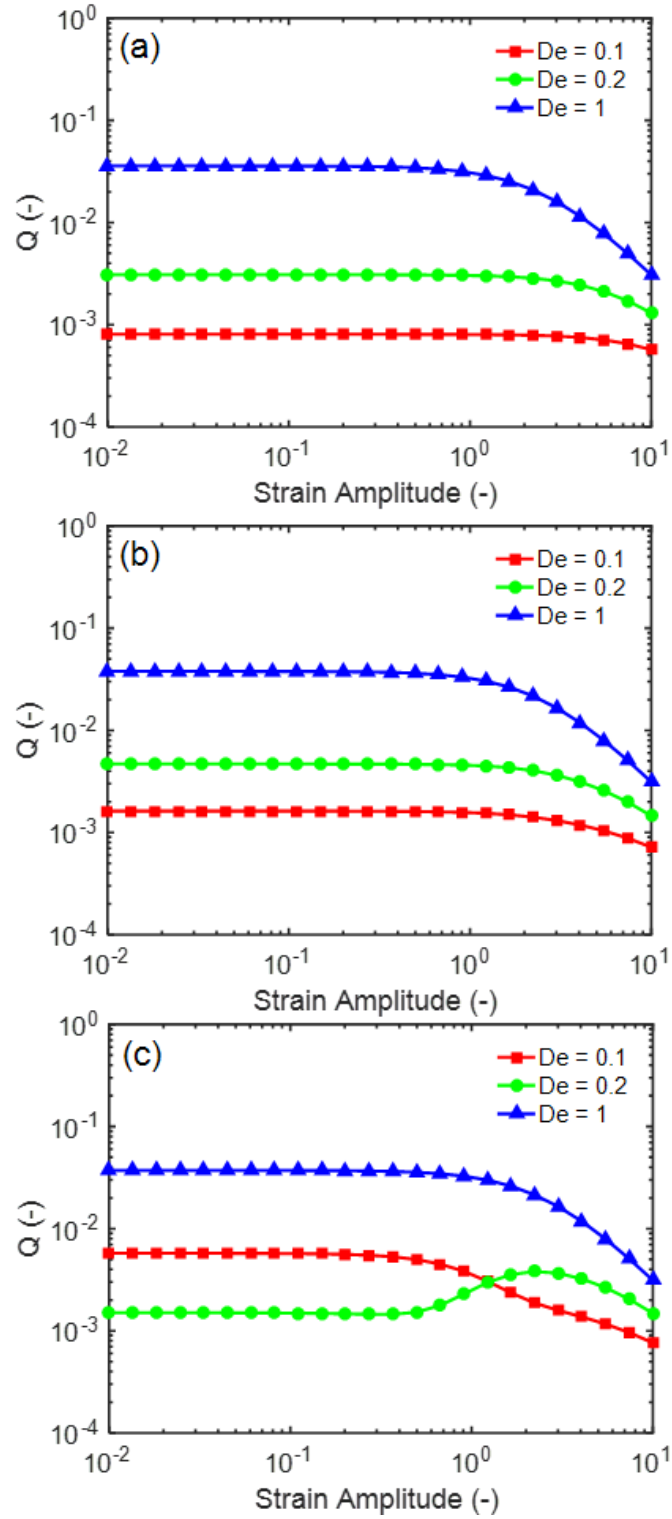


Figure 3.4 Numerical predictions of Q with strain amplitude and $\beta^a = \beta^f = 1$ for (a) matrix; (b) composite with $\phi_a = 0.1$ and $c = 5$; (c) composite with $\phi_a = 0.1$ and $c = 20$.

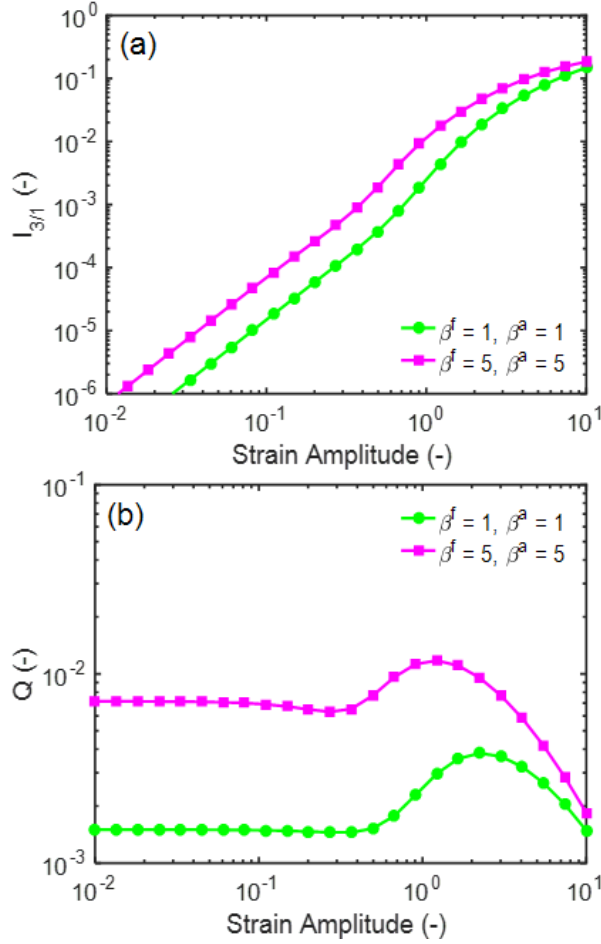


Figure 3.5 Effect of uniform CCR rates for composites with $\phi_a = 0.1$ and $c = 20$ at $De = 0.2$ on (a) $I_{3/1}$; (b) Q . Stretch parameters: $r^a = r^f = 0.01$ and $b^a = b^f = 100$.

The effect of varying CCR on the overshoot in Q is examined first with uniform CCR rates: $\beta^a = \beta^f$ and next with independently varying CCR rates where $\beta^a \neq \beta^f$. Two cases of uniform CCR rates are shown in Figure 3.5. An increase in $\beta^a = \beta^f$ from 1 to 5 leads to increases in $I_{3/1}$ and Q . The qualitative trends in both parameters are preserved with an increase in the CCR parameter: an increase in the power law exponent of $I_{3/1}$ with strain amplitude and the presence of an overshoot in Q . An increase in nonlinearity with increasing CCR parameter is also reported by Sarvestani[61] in his model computations with respect to the dynamic storage modulus at large strains.

The choice of independently varying CCR rates, where $\beta^a \neq \beta^f$, is proposed to control the rate of release of entanglements during flow for each network. The motivation for this stems from the reported configurations of attached chains especially close to the nanoparticle surface. Holt et al.[52] also simulated particle-polymer interactions of varying strengths and molecular weights and found that for stronger chain attachment through covalent bonding, particle-attached chains are stretched near the particle surface, while still entangled with the bulk matrix far away from the surface. Senses and Akcora[64] derived a mechanistic model to predict the elastic stress buildup in polystyrene/silica nanocomposites under LAOS flows and found that the model matches well with experiments when chains near the filler surface are stretched. These results imply that a distribution of stretching occurs along the attached chain segments during flow. Stretched chains are unable to form entanglements until fully retracted,[26] thus a distribution of stretching in the attached chains would lead to fewer entanglements than with unstretched chains. Hence we have chosen to represent this effect with a higher CCR parameter for the attached chains; i.e. $\beta^a > \beta^f$. For large β^a , τ_{or}^{fa} for the free-attached entanglements approaches τ_s^f resulting in faster relaxation than the attached-free entanglements. This faster relaxation leads to the following ordering of component stresses from different types of entanglements: $\sigma^{aa} > \sigma^{af} > \sigma^{fa} > \sigma^{ff}$, where now the component stresses of mixed chain entanglements are no longer equal as they are with uniform CCR rates allowing each entanglement to uniquely contribute to the stress and nonlinearity. Conversely, it follows that attached chains convected at a slower rate will require $\beta^a < \beta^f$ in which τ_{or}^{af} approaches τ_s^a and the stresses follow: $\sigma^{aa} > \sigma^{fa} > \sigma^{af} > \sigma^{ff}$. It is the effect of CCR on the chain environment (i.e. attached and free chains entangled with attached tubes) and the mixing of these entanglement networks which show differences in the nonlinearity for $\beta^a > \beta^f$ and $\beta^a < \beta^f$.

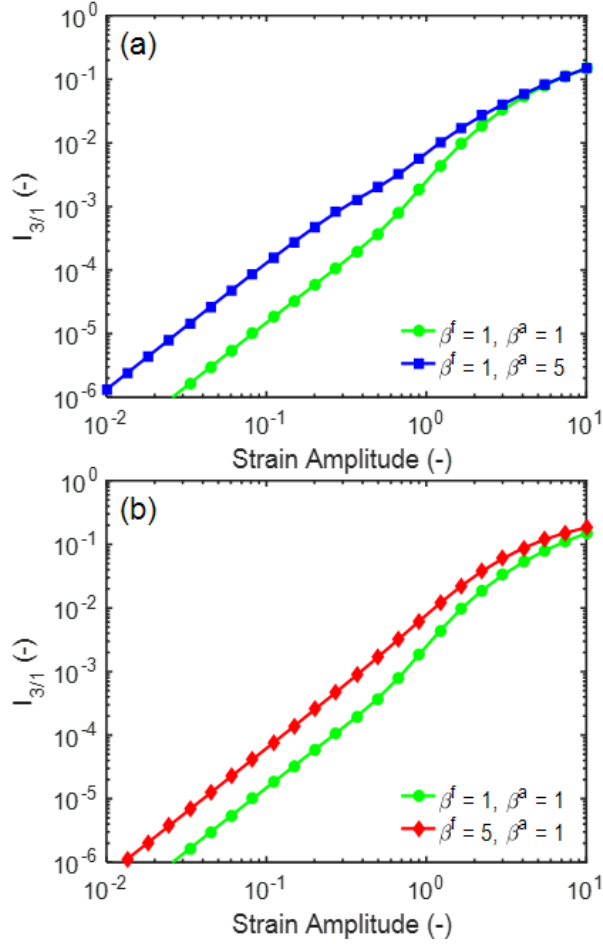


Figure 3.6 $I_{3/1}$ predicted with (a) $\beta^a > \beta^f$ and (b) $\beta^a < \beta^f$ for nanocomposites with $\phi_a = 0.1$ and $c = 20$ at $De = 0.2$.

The third harmonic ratio predicted with $\beta^a > \beta^f$ is presented in Figure 3.6(a) and the result predicted with $\beta^a < \beta^f$ is presented in Figure 3.6(b), both at $De = 0.2$. The $\beta^a = \beta^f = 1$ case from Figure 3.5(a) is plotted for comparison. The increase in logarithmic slope obtained with $\beta^a = \beta^f$ is not observed in either case with unequal CCR parameters. For $\beta^a > \beta^f$ in Figure 3.6(a), a decrease from the quadratic scaling is observed near $\gamma_0 = 0.6$. While for $\beta^a < \beta^f$ in Figure 3.6(b), $I_{3/1}$ follows very nearly a quadratic scaling with strain amplitude for larger strains.

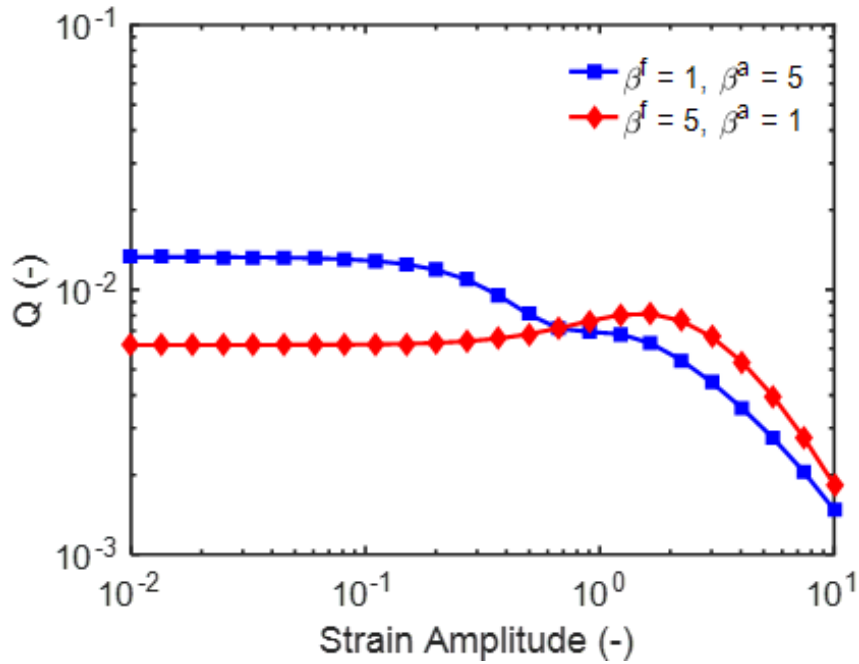


Figure 3.7 Predicted Q with $\beta^a < \beta^f$ and $\beta^a > \beta^f$ for composites with $\phi_a = 0.1$ and $c = 20$ at $De = 0.2$.

The effect that varying CCR rates have on the attached and free chain environments is more clearly depicted in a plot of Q , presented in Figure 3.7. A weak overshoot is observed in Figure 3.7 for the $\beta^a < \beta^f$ while similar low strain asymptote is observed when compared with $\beta^a = \beta^f = 5$ in Figure 3.5(b). The Q plot for $\beta^a > \beta^f$ however, clearly shows no overshoot and a progressive decrease in magnitude with increasing strain amplitude. The disappearance of the overshoot may be attributed to an increase in nonlinearity in the low strain region. This indicates that the nonlinearity is more sensitive to the dynamics of the slower relaxing attached chains and the entanglements they participate in. It has already been mentioned that only a decrease in Q with increasing strain amplitude for nanocomposites are reported in the literature. Therefore, we focus the discussion now on nonlinear trends caused by the removal of entanglements by CCR for the case $\beta^a > \beta^f$.

For $\beta^a > \beta^f$, the component stresses σ^{aa} , σ^{fa} , σ^{af} , σ^{ff} are evaluated at varying strain amplitudes and plotted in Figure 3.8(a). This figure illustrates the order of breakup of the entanglement networks and their contribution to the nonlinearity. Specifically, the onset of nonlinearity in Figure 3.8(a) follows the order: σ^{aa} , σ^{fa} , σ^{af} , σ^{ff} . Similar trends in the $I_{3/1}$ parameter in Figure 3.8(b) confirm that attached chain entanglements contribute greatest to the nonlinearity at each strain amplitude.

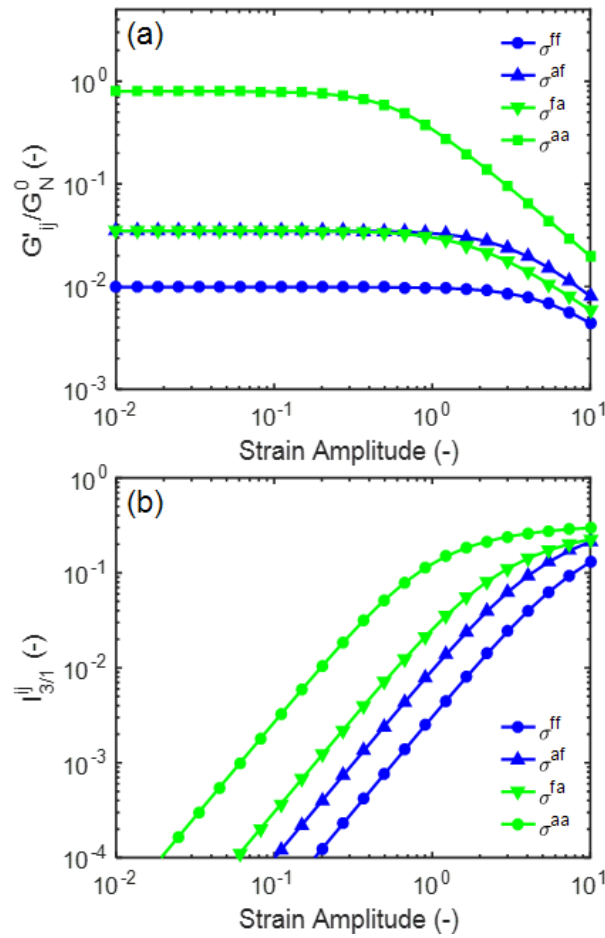


Figure 3.8 Component stresses with increasing strain amplitude and $\beta^a > \beta^f$ for composites with $\phi_a = 0.1$ and $c = 20$ at $De = 0.2$ showing (a) normalized storage modulus; (b) third harmonic ratio.

3.3.3 $Q_0(\omega)$ Asymptotic Solution

A low strain asymptotic solution of Q_0 is derived. The asymptotic shear stress for each entanglement pair network is integrated using Equations 3.25-3.26 for the third harmonic ($n = 3$).

The real third harmonic intensity for each entanglement is given as,

$$I'_{3,ij} = G_N^0 [I'_{3,ij}{}^{DRCS} + I'_{3,ij}{}^{CCR} + I'_{3,ij}{}^{FE}] \gamma_0^3 + O(\gamma_0^5) \quad (3.35)$$

$$I'_{3,ij}{}^{DRCS} = \frac{De^{ij^3}(1-r^{ij})[(6+22r^{ij})De^{ij^3} - (6+2r^{ij})De^{ij}]}{6(1+De^{ij^2})(1+4De^{ij^2})(1+4De^{ij^2}r^{ij^2})(1+9De^{ij^2})}$$

$$I'_{3,ij}{}^{CCR} = \frac{\beta^j De^{ij^3} [b^i(1-r^{ij})-1] [(3+14r^{ij})De^{ij^3} - (5+2r^{ij})De^{ij}]}{6(b^i-1)(1+De^{ij^2})^2(1+4De^{ij^2}r^{ij^2})(1+9De^{ij^2})}$$

$$I'_{3,ij}{}^{FE} = \frac{-De^{ij^4}r^{ij}[6De^{ij^4}r^{ij} - (7+10r^{ij})De^{ij^2} + 1]}{2(b^i-1)(1+De^{ij^2})^2(1+4De^{ij^2}r^{ij^2})(1+9De^{ij^2})}$$

and the imaginary third harmonic intensity,

$$I''_{3,ij} = G_N^0 [I''_{3,ij}{}^{DRCS} + I''_{3,ij}{}^{CCR} + I''_{3,ij}{}^{FE}] \gamma_0^3 + O(\gamma_0^5) \quad (3.36)$$

$$I''_{3,ij}{}^{DRCS} = \frac{-De^{ij^3}(1-r^{ij})[12De^{ij^4}r^{ij} - (11+12r^{ij})De^{ij^2} + 1]}{6(1+De^{ij^2})(1+4De^{ij^2})(1+4De^{ij^2}r^{ij^2})(1+9De^{ij^2})}$$

$$I''_{3,ij}{}^{CCR} = \frac{-\beta^j De^{ij^3} [b^i(1-r^{ij})-1] [6De^{ij^4}r^{ij} - (7+10r^{ij})De^{ij^2} + 1]}{6(b^i-1)(1+De^{ij^2})^2(1+4De^{ij^2}r^{ij^2})(1+9De^{ij^2})}$$

$$I''_{3,ij}{}^{FE} = \frac{-De^{ij^4}r^{ij}[(3+14r^{ij})De^{ij^3} - (5+2r^{ij})De^{ij}]}{2(b^i-1)(1+De^{ij^2})^2(1+4De^{ij^2}r^{ij^2})(1+9De^{ij^2})}$$

As with the first harmonic ratios in Equations 3.32-3.33, the Deborah number De^{ij} is defined in

Table 3.1. The scaled stretch time r^{ij} appearing in Equations 3.35-3.36 is defined as,

$$r^{ij} = \frac{(b^i-1)\tau_S^i}{b^i\tau_D^{ij}} \quad (3.37)$$

and the scaled stretch time is rewritten in terms of dimensionless groups in Table 3.2.

Table 3.2 Definition of r^{ij} for each free and attached chain entanglement pair

i, j pair	r^{ij}
f, f	$\frac{2(b^f - 1)r^f}{b^f}$
f, a	$\frac{(c + 1)(b^f - 1)r^f}{cb^f}$
a, f	$\frac{(c + 1)(b^a - 1)r^a}{cb^a}$
a, a	$\frac{2(b^a - 1)r^a}{cb^a}$

The third harmonic intensities for each entanglement may be separated into three terms arising from the following effects: double reptation with chain stretch (DRCS), convective constraint release (CCR) and finite extensibility (FE). Since both De^{ij} and r^{ij} are finite and non-zero, the DCRS term will always remain non-zero. However, if CCR is neglected (i.e. $\beta^j = 0$) or the chains are considered Gaussian with infinite extensibility (i.e. $b^i \rightarrow \infty$), the CCR and FE terms will respectively drop out of Equations 3.35-3.36. Combining the third harmonic contributions from various entanglement types into the mixing rule given in Equations 3.27-3.28 yields the third harmonic intensity. Finally, combining the total first and third harmonic intensities into Equation 3.31 yields the asymptotic solution for Q_0 , which is discussed here.

The zero-strain intrinsic nonlinearity Q_0 is a frequency dependent parameter. Unlike the linear viscoelastic moduli which depend on ϕ_a and c alone, Q_0 is sensitive to the CCR parameters. The effect of c on Q_0 for the matrix and composites with $\phi_a = 0.1$ is shown in Figure 3.9 using the asymptotic solution. Results of numerical simulations using FT rheology are presented with the asymptotic solutions.

In Figure 3.9, for weak attachment with $c = 5$, Q_0 is found to be higher for the composite than for the matrix up to $De = 1$. Above $De = 1$, the two curves merge onto a high Deborah number plateau, similar to the linear viscoelastic modulus in Figure 3.1(a). For strong attachment with $c = 20$, a peak appears in Q_0 at $De = 0.08$, with a minimum near $De = 0.2$. The peak is due to the relaxation of entanglements with attached chains, whereas the minimum results from the destruction of these entanglements.

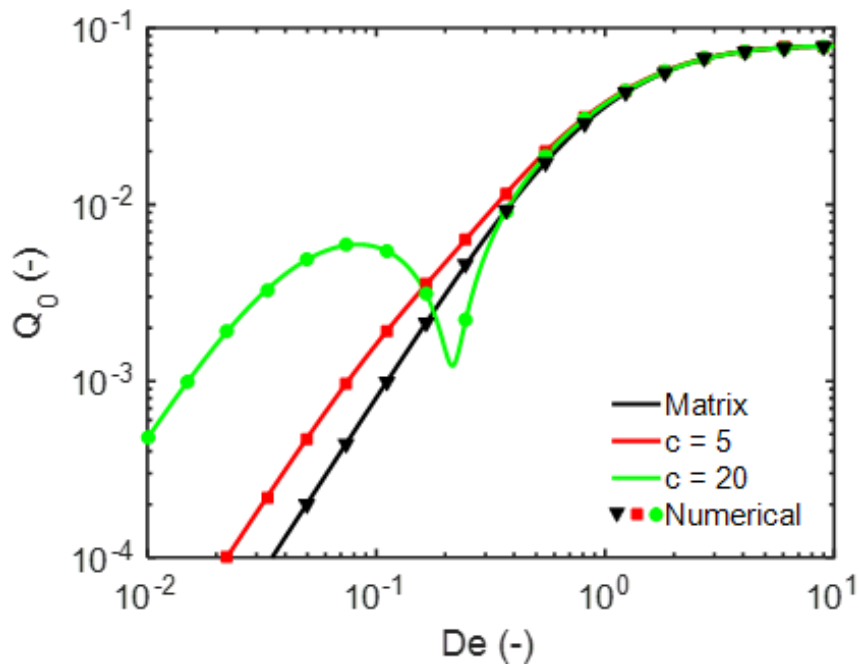


Figure 3.9 Asymptotic solutions of Q_0 showing effect of c for $\phi_a = 0.1$ and $\beta^a = \beta^f = 1$. Results of simulations are also plotted for comparison.

The minimum is observed only for well separated relaxation times- when the particle-polymer interactions are strong. However, this is not unique to the double reptation averaging scheme used in this work.

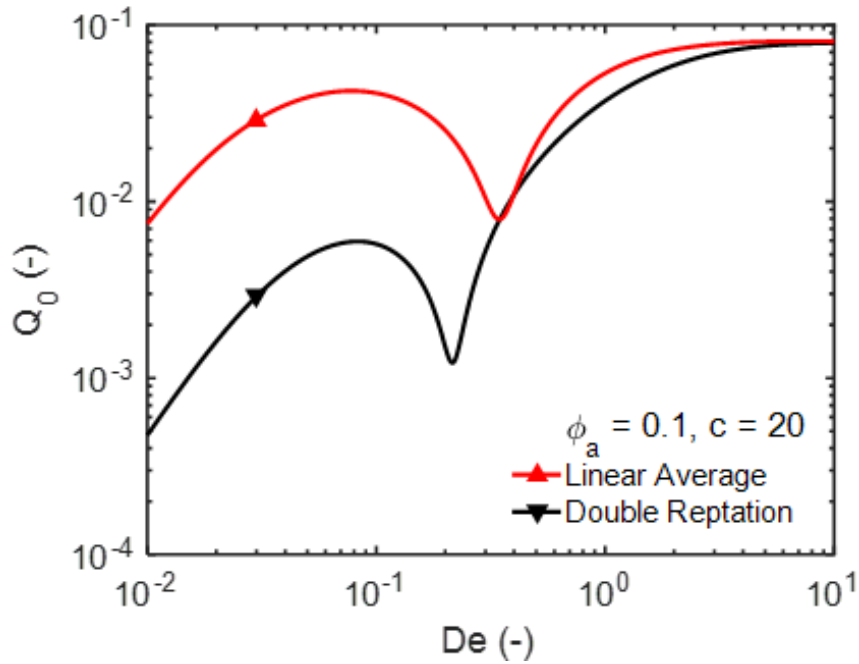


Figure 3.10 Comparison of Q_0 plots obtained from linear averaging (Equation 3.1) and double reptation (Equation 3.4) mixing rules for composites with $\phi_a = 0.1$, $c = 20$ and $\beta^a = \beta^f = 1$.

A comparison of Q_0 between double reptation averaging used in this work and the linear averaging presented by Sarvestani[61] is made for $\phi_a = 0.1$ and $c = 20$, shown in Figure 3.10. Both linear averaging and double reptation generate a peak in Q_0 . The nonlinearity predicted by linear averaging in Equation 3.1 is higher than by double reptation in Equation 3.4 because the weighting is higher in Equation 3.1.

In an effort to illustrate the differences between having uniform CCR rates and independent CCR rates, plots of Q_0 are compared for increasing various volume fraction of attached chains, with c fixed at 20. These plots are shown in Figure 3.11 for nanocomposites with uniform CCR rates ($\beta^a = \beta^f = 1$) in Figure 3.11(a) and independent CCR rates ($\beta^a = 5$, $\beta^f = 1$) in Figure 3.11(b). The Q_0 curves in Figure 3.11 rise in magnitude with increasing volume fraction of attached chains regardless of the chosen CCR parameters.

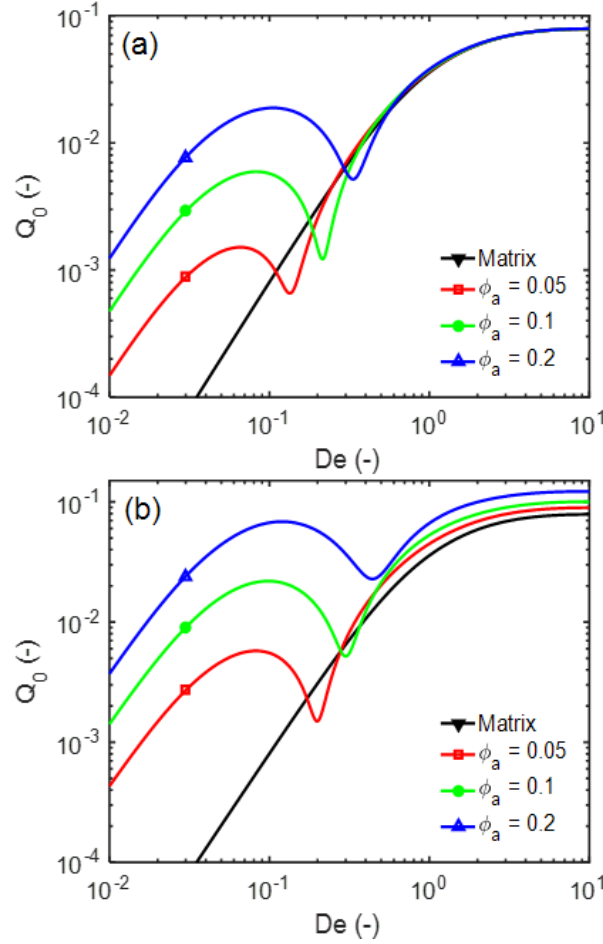


Figure 3.11 Asymptotic solution of Q_0 for $c = 20$ and (a) uniform CCR rates, $\beta^f = \beta^a = 1$ and (b) independent CCR rates, $\beta^f = 1$, $\beta^a = 5$.

For $\beta^a = \beta^f$ in Figure 3.11(a), all curves merge to a high De plateau above $De = 1$. This is consequence of $\sigma^{fa} = \sigma^{af}$ resulting in equal nonlinear contributions to Q_0 . For $\beta^a > \beta^f$, the plateau at large De is also raised in magnitude with increasing volume fraction of attached chains, due to an increase in nonlinearity from σ^{fa} entanglements shown in Figure 3.8(b). The increased relaxation of σ^{fa} entanglements due to an increase in the CCR rate in the attached chain environment shifts the nonlinearity $I_{3/1}$ to lower Deborah numbers, resulting in an increase in the Q_0 plateau. Hassanabadi et. al.[7] report that Q_0 for EVA nanocomposites with low loadings of clay was greater than Q_0 for the matrix at larger Deborah numbers (ca. $De \approx 1.25$). Based on the

results of Figure 3.11(b), only when the attached chain CCR rates are faster than CCR rates for free chains, can the nonlinearity of the composite be greater than that of the matrix. This shows that for $\beta^a > \beta^f$, faster flows, indicated by higher Deborah numbers, have a greater convective effect on the nanoparticles resulting in the particle-attached chains contributing more to the nonlinearity for all Deborah numbers.

To further illustrate that the nonlinear behavior in nanocomposites is more sensitive to independent CCR rates than uniform CCR rates, the peak magnitude Q_0 at low Deborah numbers relative to the Q_0 plateau at high Deborah numbers is calculated for $c = 20$ over varying ϕ_a values. This ratio is plotted in Figure 3.12(a) against values of $\beta^a = \beta^f$ and in Figure 3.12(b) against varying β^a with β^f fixed at 1. For all choices of $\beta^a = \beta^f$ presented in Figure 3.12(a), the relative nonlinearity is independent of the CCR rate, showing only an increase with increasing ϕ_a . However, Figure 3.12(b) shows an increase in the relative nonlinearity with increasing β^a which is amplified by an increase in ϕ_a . By increasing β^a and the CCR rate of the attached chain environment, the σ^{aa} and σ^{fa} entanglement networks dominate the nonlinear response.

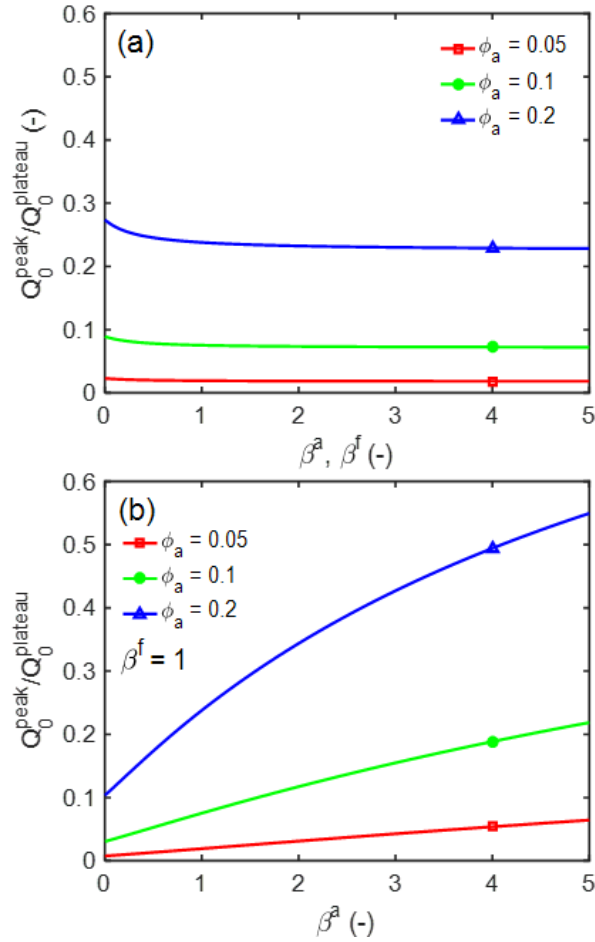


Figure 3.12 The low De maximum of Q_0 relative to the high De plateau of Q_0 for $c = 20$ with (a) uniform CCR rates, varying $\beta^a = \beta^f$ and (b) independent CCR rates, varying β^a with fixed $\beta^f = 1$.

3.4 Conclusions

A new nonlinear viscoelastic model is developed in this work for entangled polymer chain networks with attachments to nanoparticle surfaces. The stress contributions of different types of entanglements are averaged in a double-reptation framework with independent convective constraint release parameters for particle-attached chains and free chains. The nonlinearity here may be attributed to the breakup of entanglements between particle-attached and free chains. Entanglements with the particle-attached chains lead to the greatest extent of nonlinearity; this is

further intensified by slower relaxation dynamics and an increase in the fraction of attached chains present in the system.

Numerical simulations of strain sweep tests under LAOS flows are performed and analyzed using Fourier transform rheology to compare the nonlinearity between nanocomposites and unfilled polymers. Several measures are used to describe the nonlinearity: the onset of strain softening in the elastic modulus as well as the magnitude and strain dependence of $I_{3/1}$ and Q . The trends in the zero-strain intrinsic nonlinearity Q_0 are also investigated using a low-strain asymptotic solution of the model.

The onset of strain softening in the low frequency plateau region is seen to be particularly sensitive to the strength of polymer-particle attachment or c . The predicted nonlinearity for cases where the particle-chain attachment is strong (large c) displays several distinct features. When the CCR parameters are identical for attached chains and free chains, the nonlinearity including strain softening and a strain overshoot in Q are predicted. Specifically, there is an increase in the power law exponent of $I_{3/1}$ with strain amplitude corresponding to an overshoot in Q at low Deborah numbers ($De \approx 2/c$) when the CCR parameters are chosen to be equal for both chain types. When the CCR parameter for attached chains is larger than for the free chains, the predicted nonlinearity displays no overshoot in Q .

The choice of higher CCR parameter for attached chains is motivated by reports in the literature that the attached chains are stretched near the particle surface during flow, leading to fewer entanglements.[52] This effect is modeled here using a faster CCR rate for attached chains than for free chains. The latter aspect leads to a higher Q_0 for the composite compared to the matrix at all Deborah numbers. However, when the CCR rates are equal, the same degree of nonlinearity is predicted for the composite and the matrix at high Deborah numbers. Hence in

LAOS flows, faster convective constraint release of attached chain entanglements leads to quicker breakup of the entanglement network resulting in higher nonlinearities predicted for nanocomposite systems.

CHAPTER 4

FOURIER TRANSFORM RHEOLOGY OF POLYPROPYLENE-LAYERED SILICATE NANOCOMPOSITES

4.1 Introduction

Polymer layered-silicate nanocomposites have been of practical interest for reinforcing the polymer matrix leading to an increase in both stiffness and toughness of manufactured products.[65] Economic factors and commercial availability make clay and other layered-silicates an attractive choice for both industry and academia. The abundance of literature on the processing of these materials also offer a means to fine tune the desired final composite properties by tailoring the interactions between the polymer and filler phases.[38, 66, 67] Additional interactions between particles are also present with high filler concentrations resulting in a percolated filler network.[68-70] Though the filler network dominates the rheological properties, it can often lead to a brittle material due to early breakup of the network at large deformations i.e. the Payne effect.[40, 46, 71] Similar improvements in the rheology have been shown at low loadings when improved dispersion of the nanofiller.[38, 72]

In general, two criteria are needed for good dispersion: intercalation of the polymer chains and delamination of the silicate layers.[49, 69, 73] Montmorillonite clay, a 2:1 phyllosilicate, is one example of a layered silicate filler used in making nanocomposites. Montmorillonite exists naturally in stacks of nanolayers having a dimension of 1 nm thickness and an aspect ratio around 200. To promote intercalation of the polymer matrix, the gallery spacing is first increased through a cation exchange process, substituting the sodium cations for larger molecular weight surfactant.[57, 74] Surface treatment of the nanoclay through silane addition then provide

chemically reactive sites for the polymer matrix or an energetically similar compatibilizer resulting in particle-attached chains.[38, 66] These particle-attached chains have reduced mobility due to their attachment and with sufficient molecular weight, are free to entangle with the matrix chains to form an entanglement network which demonstrates a liquid-to-solid transition in the rheological response.[33, 37, 47]

The linear viscoelastic effect of particle-attached entanglements on the melt rheology for layered-silicate nanocomposites has been characterized extensively. Most notably is the observed increase in the dynamic shear moduli at low frequencies due to the slower dynamics of attached chains.[33, 37] When exposed to increasing deformations, these entanglements also lead to an earlier observed nonlinear response similar to the Payne effect for percolated filler networks.[58] In recent years, the nonlinear response has been probed using large amplitude oscillatory shear (LAOS) flows in order to relate the nonlinear behavior to the dynamics and morphology of various complex fluids, including nanocomposites.[4]

Much of the literature concerning LAOS flows of nanocomposites is focused on loadings above the percolation threshold.[6, 7, 25] Arguably the most sensitive method to quantify the nonlinearities in LAOS flows is through Fourier transform (FT) rheology, whereby the non-sinusoidal stress waveform in the nonlinear regime is Fourier transformed into higher order harmonics.[5, 13, 14] Normalizing the third harmonic intensity with the first harmonic yields $I_{3/1}$, a characteristic measure in FT rheology. Hassanabadi et. al.[7] used FT rheology to determine the nonlinear $I_{3/1}$ ratio for ethyl vinyl acetate (EVA) composites using both carbon nanotubes (CNT) and montmorillonite clay and found that with increasing filler loading, particle-particle interactions raised the nonlinearity in magnitude. The quadratic scaling of $I_{3/1}$ with strain amplitude observed for the matrix, a trend found in many unfilled polymer systems, was no longer

observed for composites where particle-particle interactions were dominant. Similar trends in FT rheology for highly filled nanocomposites are reported confirming the particle-particle effect on the nonlinear response.[6, 25]

The aim of this work is to quantify the nonlinear response of particle-attached entanglements in dilute polypropylene montmorillonite clay nanocomposites under LAOS flows using FT rheology. This study also tests LAOS flows over a range of frequencies to characterize both the strain and frequency dependence of the nonlinear FT rheology parameters. At the frequencies chosen, the nonlinear response due to entanglement breakup of both particle-polymer and polymer-polymer interactions are explored.

4.2 Experimental

4.2.1 Materials

Polypropylene (PP) homopolymer matrix (trade name: PP4792E1) with a melt flow rate (MFR) of 2.7 g/10 min (ASTM D1238, 230°C, 2.16kg load) was obtained from ExxonMobil. A maleic anhydride grafted polypropylene-polyethylene (PP-g-MA) copolymer (trade name: PO1015) with an MFR of 150 g/10 min (ASTM D1238, 230°C, 2.16kg load) and a maleic anhydride (MA) content of 0.42% was purchased from ExxonMobil and used as a compatibilizer. The polypropylene homopolymer and compatibilizer were then melt mixed with an organically modified montmorillonite (OMMT) clay. The OMMT (trade name: Nanomer I.44P) was obtained from Nanocor. The OMMT is produced by the manufacturer with a quaternary onium surfactant with two C-18 tails through a cation exchange process to increase interparticle spacing between the clay galleries and increase exfoliation during processing. To improve compatibility of the clay with the matrix, a vapor-phase silylation technique was employed to treat the clay surfaces with 1% by weight of aminoalkyldimethoxysilane.[75] The combined effect of silylation and

compatibilizer lead to the formation of particle-attached chains which have reduced chain dynamics relative to the matrix chains.

4.2.2 Sample Preparation

Nanocomposites were prepared with both 3 and 5wt% of clay with a ratio of PP-g-MA to OMMT held at a 1:1 compatibilizer to clay by weight. A summary of the materials used in this study is found in Table 4.1.

Table 4.1 Formulations for Different Nanocomposites

Sample	Polypropylene (PP4792E1)	Maleic anhydride grafted PP (PO1015)	Organically modified montmorillonite clay (I.44P)
PP	100 wt%	-	-
PPNC3	96 wt%	3 wt%	3 wt%
PPNC5	90 wt%	5 wt%	5 wt%

Polymer nanocomposites were melt blended in a Leistritz twin screw extruder. A masterbatch of 54:23:23 PP:PP-g-MA:OMMT was first extruded at 200 RPM and 180°C. The resulting extrudate was then cooled and pelletized. Masterbatch pellets were then let-down with PP and extruded to achieve the desired clay concentrations. Polymer nanocomposite pellets were compression molded into 75x75x1 mm plaques at 200°C using a Wabash compression molding machine. The plaques were then used for rotational rheometry testing.

4.2.3 Linear Rheology

Steady and dynamic shear tests were performed in an ARES rotational rheometer with a 2K FRTN1 torque transducer from TA instruments. Tests were conducted using 25 mm parallel plates in a forced convection oven under a nitrogen atmosphere at 200°C. Before each test, samples were loaded into the rheometer using a gap-closing test procedure controlled by the rheometer software to remove loading effects and achieve reproducible data. Plates had an initial gap setting

of 2.05 mm where samples were loaded and allowed to melt for 2 min. After melting, the gap was closed to 1.05 mm uniformly over 500 sec. The sample was then trimmed, and the plates were then further closed to 1 mm over 25 sec at which point a 10 min annealing stage began. The total sample loading time with annealing was approximately 20 min. Dynamic time sweep tests at 1 rad/s and 1% strain confirmed that the transients in modulus were minimized and reproducible for each nanocomposite tested.

The linear region was determined through small angle oscillatory shear (SAOS) strain sweep tests at 1 rad/s from strains of 0.1-100% with 7 points per decade. For all samples, frequency sweep tests at a strain amplitude of 1% were conducted from 0.01-100 rad/s with 7 points per decade at 200°C.

4.2.4 Nonlinear Rheology

Large amplitude oscillatory shear (LAOS) tests used the same loading procedure as for the linear testing of polymer nanocomposites. Several low frequencies ranging from 0.1-10 rad/s were tested from 30-300% strains with 7 points per decade with 5 cycles per strain. This cycle number was chosen to prevent thermal degradation for low frequencies, where the testing time was much longer. Additionally, the deformation history was kept constant across all frequencies. In all strain sweep tests, the total testing time was kept under 1 hour which was verified through time sweep tests as a thermally stable operating window.

4.2.5 Fourier Transform Rheology

To interpret LAOS results, Fourier transform (FT) rheology was employed.[13] Raw voltages of torque (stress), angular displacement (strain) and force were acquired from the rheometer using a 16-bit resolution high-speed data acquisition (DAQ) card (PCIe-6341 X series,

National Instruments) with a 100 kS/sec/channel sampling rate. A lab-written MATLAB code for data acquisition and post processing was used.

The advantage of FT rheology is in its ability to determine nonlinearities that develop in the stress waveform. To reduce systematic noise from the rheometer, oversampling of the raw voltages acquired through the DAQ card was necessary to improve the signal-to-noise (S/N) of the Fourier transformed stress waveform.[11, 14] The oversampling number is the number of raw voltage data points “boxcar averaged” into a single data point, defined here as,

$$N_o. \equiv \frac{\pi F_s}{n \omega_0} \quad (4.1)$$

where F_s is the DAQ sampling frequency, ω_0 is the testing frequency and n is the maximum observable harmonic. Wilhelm et. al.[14] suggested that the maximum harmonic is doubled in the oversampling number as to prevent oversampling of the nonlinear stress response. It should be noted that at the time FT rheology was introduced, oversampling or “boxcar averaging” of the stress waveform was performed during data acquisition. In this work, we have eliminated the need for “on-the-fly” averaging and instead oversample the data after testing has completed. This then allows for an optimum oversampling number to be determined during post-processing so as to achieve large S/N ratios.

A full review on FT Rheology and LAOS techniques is available elsewhere.[5] In this work, three nonlinear parameters are of particular importance: the relative third harmonic ratio $I_{3/1}$, the nonlinear parameter Q and the zero-strain intrinsic nonlinearity Q_0 .

The ARES rheometer used in this study is equipped with a separated motor-transducer (SMT), meaning the bottom plate displaces the sample and the top plate measures the resulting torque. The deformation applied is sinusoidal,

$$\gamma = \gamma_0 \sin(\omega_0 t) \quad (4.2)$$

where γ and γ_0 are the strain and strain amplitude, respectively. The resulting stress is mathematically represented by a Fourier series,

$$\sigma = \sum_{n, odd} \sigma_n \sin(n\omega_0 t + \delta_n) \quad (4.3)$$

where σ_n and δ_n are the Fourier coefficients and phase angles, respectively. In the linear regime, only the first harmonic ($n = 1$) is observed. In the nonlinear regime, higher order harmonics appear resulting in a non-sinusoidal stress waveform. It is the increase in the third harmonic ($n = 3$) from which the nonlinear FT rheology parameters are derived. The relative third harmonic is defined as,

$$I_{3/1}(\omega, \gamma_0) \equiv \frac{\sigma_3}{\sigma_1} \quad (4.4)$$

It has been shown mathematically throughout the literature[5, 9, 76] that the n^{th} harmonic of stress, when expanded as a power series in strain, is related to γ_0^n . Therefore, the relative third harmonic ratio $I_{3/1}$ scales quadratically with strain. These trends were also observed experimentally in neat systems.[10, 12] However, deviations from a slope of 2 have been reported for composites,[7] strain hardening systems,[77] strain stiffening suspensions,[78] and long chain branching.[79]

In an effort to develop a frequency dependent nonlinear parameter to remove the strain dependence of $I_{3/1}$, Hyun and Wilhelm[10] first developed a new nonlinear parameter,

$$Q(\omega, \gamma_0) = \frac{I_{3/1}}{\gamma_0^2} \quad (4.5)$$

At low strains a monotonic value is observed resulting in the final nonlinear parameter Q_0 ,

$$Q_0(\omega) = \lim_{\gamma_0 \rightarrow 0} Q(\omega, \gamma_0) \quad (4.6)$$

Where the zero-strain intrinsic nonlinearity Q_0 is now a frequency dependent parameter which is sensitive to both system morphology and relaxation dynamics. Experimentally, the Q_0 was shown to be sensitive to the percolation threshold in composites when the filler loading was increased, and particle-particle interactions dominated the rheology.[6, 7] In addition, well separated maxima in Q_0 at low and high frequencies were observed for comb-type polymers which corresponded to the polymer backbone and arm relaxation times.[10] The same sensitivity in Q_0 to relaxation dynamics was later shown numerically using constitutive models such as the model.[9]

4.3 Results and Discussion

4.3.1 Dynamic Frequency Sweep Tests

Ren et. al.[38] compounded PP/OMMT composites using the same organically modified filler and compatibilizer used in this study, with a different polypropylene matrix having a higher melt flow rate. It was proposed that two attachment sites are available for the dimethoxy groups: covalent linkages at the clay edge and hydrogen bonding in the clay galleries. The resulting imide linkage between the silylated clay and PP-g-MA compatibilizer lead to the formation of particle-attached chains. Entanglements with particle-attached chains generate an increased linear viscoelastic response in both the storage and loss moduli at low frequencies for PP/OMMT nanocomposites compared with the PP matrix as shown in Figure 4.1.

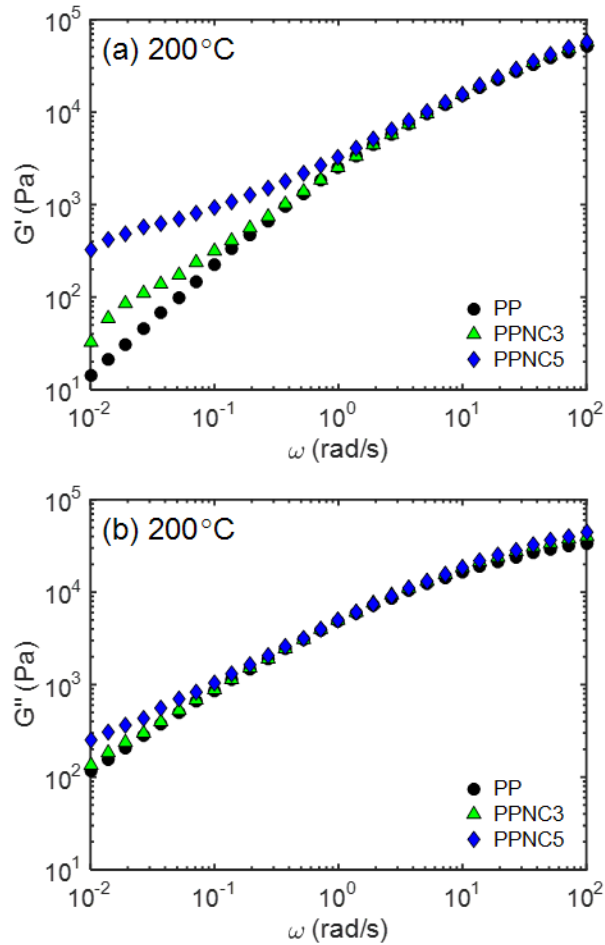


Figure 4.1 (a) Storage modulus and (b) loss modulus of nanocomposites with varying loading and the matrix.

For highly filled systems, particle-particle interactions have been reported to dominate the linear viscoelasticity at low frequencies due to the formation of a filler network.[40, 69, 70] The composites studied here have low concentrations where no filler network is present, though the possibility for chain bridging exists. However, the increase in storage modulus in Figure 4.1(a) at low frequencies is primarily attributed to the entanglements with particle-attached chains.

4.3.2 Fourier Transform Rheology

The entanglement network formed by particle-attached chains was tested under LAOS flows and the nonlinear response quantified with FT rheology. Oversampling of the stress

waveform is needed to achieve high S/N ratios. The oversampling number in eq. (1) must be large enough to reduce the electronic noise from the rheometer, but small enough as to not average out the true nonlinear response of the polymer.[11] For neat systems, the deviation from electronic noise to the true nonlinear response is typically marked by a quadratic dependence of $I_{3/1}$ with strain amplitude. However, power-law scaling less than 2 have been reported for various systems, most notably in branched polymers[8, 10, 12] and highly loaded nanocomposites.[6, 7] In this study, strain sweep tests at a fixed frequency of 1 rad/s were first tested for both composites and matrix across two regimes: SAOS (linear) and LAOS (nonlinear). The resulting storage modulus and nonlinear parameters are presented in Figure 4.2.

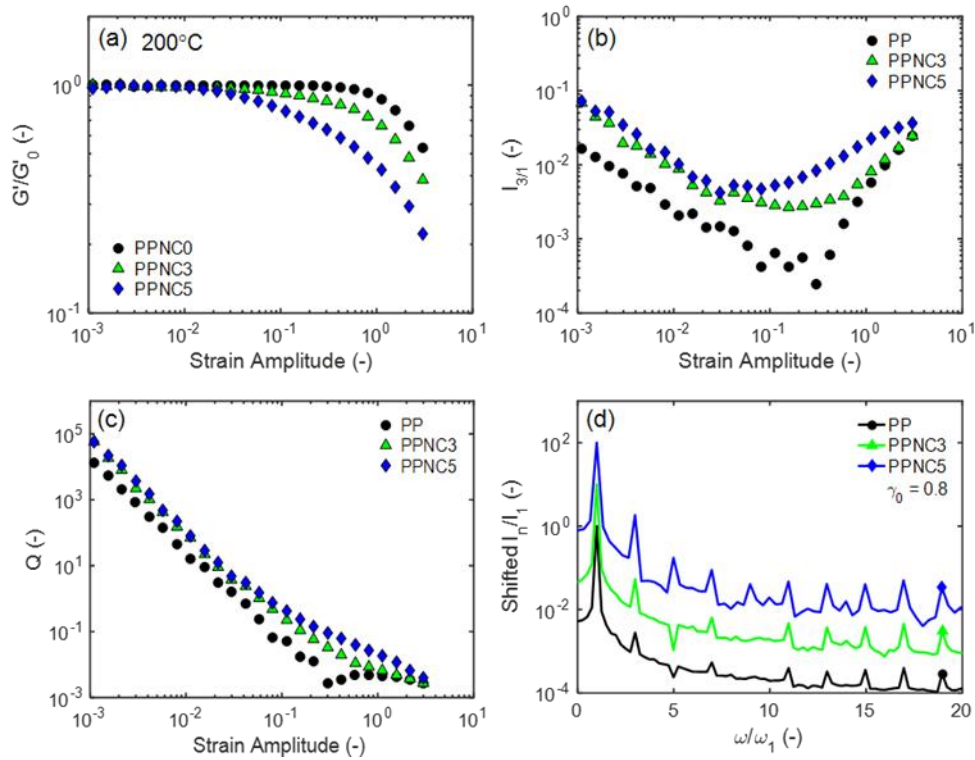


Figure 4.2 Dynamic storage modulus for composites and matrix at 200°C for (a) 1 rad/s with corresponding (b) $I_{3/1}$ parameter (c) Q parameter and (d) relative intensities acquired using FT rheology at $\gamma_0 = 0.8$. Relative intensities shift factors are 1, 10, 100 for PP, PPNC3, and PPNC5, respectively.

The onset of nonlinearity is observed from the storage modulus in Figure 4.2(a) for composites at $\gamma_0 = 0.04$ and 0.02 for 3wt% and 5wt% composites, respectively, compared to the matrix onset amplitude at $\gamma_0 = 0.4$. However, these strains are less clear in the nonlinear $I_{3/1}$ parameter in Figure 4.2(b). At lower strain amplitudes in the SAOS regime the electronic noise dominates the nonlinearity. For the matrix, a quadratic dependence with strain amplitude at $\gamma_0 = 0.3$ is clearly observed marking the true nonlinear response. It has been suggested to consider strains with $I_{3/1} > 0.005$ as the starting point for the nonlinear analysis[5], however this criterion fails for the nanocomposites tested here. In the nanocomposites, a region exists where the $I_{3/1}$ is nearly independent with strain due to the competing effects of the true nonlinear response and electronic noise from the rheometer. For this study, this plateau in $I_{3/1}$ is considered the noise level criterion and only strains above this level are considered.

Nanocomposites do not show a quadratic scaling behavior in $I_{3/1}$ at large strains above the defined noise threshold. As consequence, no plateau region is observed for Q in Figure 4.2(c) for nanocomposites. Based on the results of Figure 4.2(b), it was determined that strain amplitudes above $\gamma_0 = 0.3$ were less affected by noise and thus only these strains were considered for LAOS testing. Validation of the oversampling method are represented by shifted intensities from Fourier transform of the stress waveform in Figure 4.2(d) resulting in large S/N ratios of 10,000:1.

The storage modulus for the composites and matrix under LAOS testing are presented in Figure 4.3.

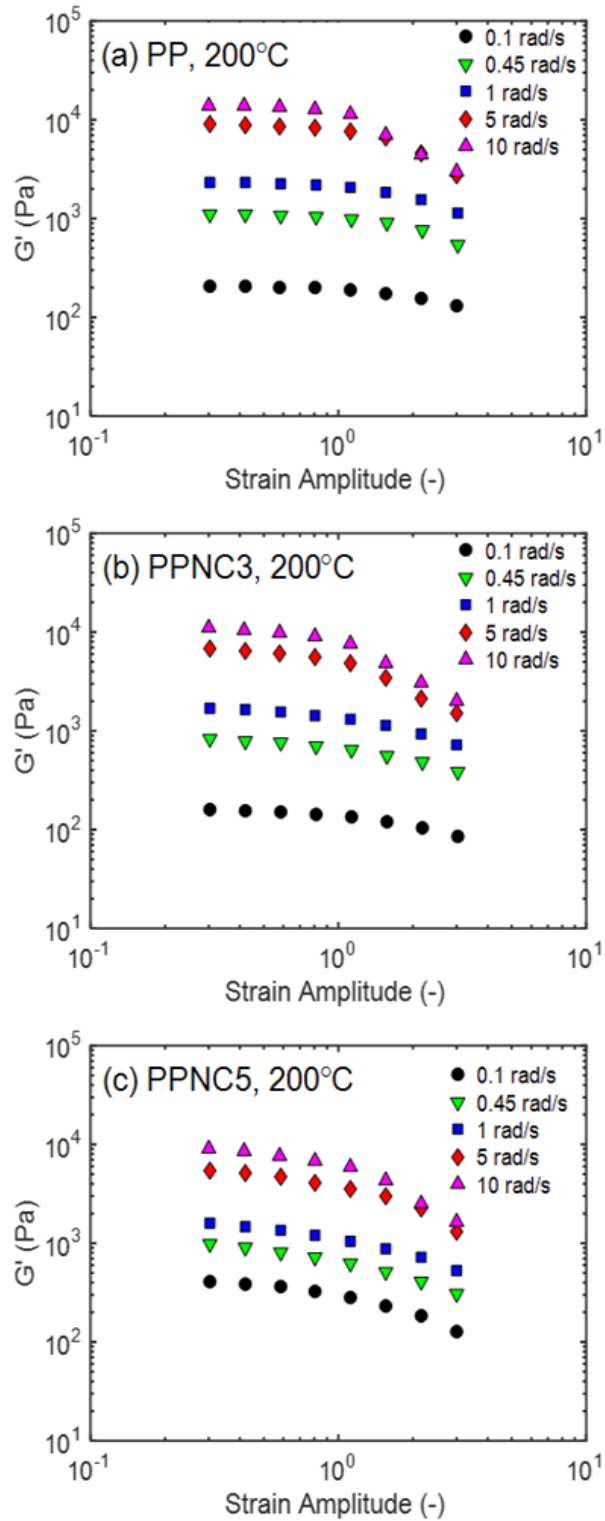


Figure 4.3 Dynamic storage modulus against strain amplitude at various frequencies for (a) matrix (b) 3wt% clay nanocomposite and (c) 5wt% clay nanocomposite.

The dynamic storage modulus presented in Figure 4.1 showed the largest variation at low frequencies where particle-polymer interactions were dominant. This variation is also observed with strain amplitude in Figure 4.3 for 0.1 rad/s in composites compared to the matrix. Here the composites show an earlier onset of nonlinearity and an increase in the degree of strain softening with increasing filler loadings as compared to the matrix. This behavior is similar to the Payne effect, where an earlier onset of nonlinearity and increase in strain softening is due to the breakup of a filler network. For dilute systems, as in the nanocomposites presented in Figure 4.3(b,c), the Payne effect is associated with the breakdown of entanglement networks formed by particle-attached chains.[58]

The corresponding relative third harmonic $I_{3/1}$ ratio for frequencies tested in Figure 4.3 are presented in Figure 4.4. Both composites in Figure 4.4(b,c) show a greater nonlinear response over the matrix Figure 4.4(a) indicated by a larger $I_{3/1}$ magnitude. The $I_{3/1}$ magnitude for the matrix increases with increasing frequency which is typically observed for unfilled polymer systems.[10] However, this trend is not observed in nanocomposites, where instead an increase in frequency leads to a decrease in the magnitude of $I_{3/1}$ especially in the low frequency regime where particle-attached entanglements dominate the rheology. For all samples, the nonlinearity collapses at frequencies above 5 rad/s with the PPNC3 composite in Figure 4.4(b) and matrix in Figure 4.4(a) showing similar nonlinear behavior. This suggests that entanglements with particle-attached chains are removed at higher frequencies and the nonlinear response is due to polymer-polymer interactions. This also corresponds with linear viscoelastic results in Figure 4.1, where the moduli are equal for the nanocomposites and matrix. A slightly higher nonlinearity is still observed at higher frequencies for the PPNC5 case in Figure 4.4(c) which may be due to hydrodynamic interactions caused by the increase in the number of particles present.

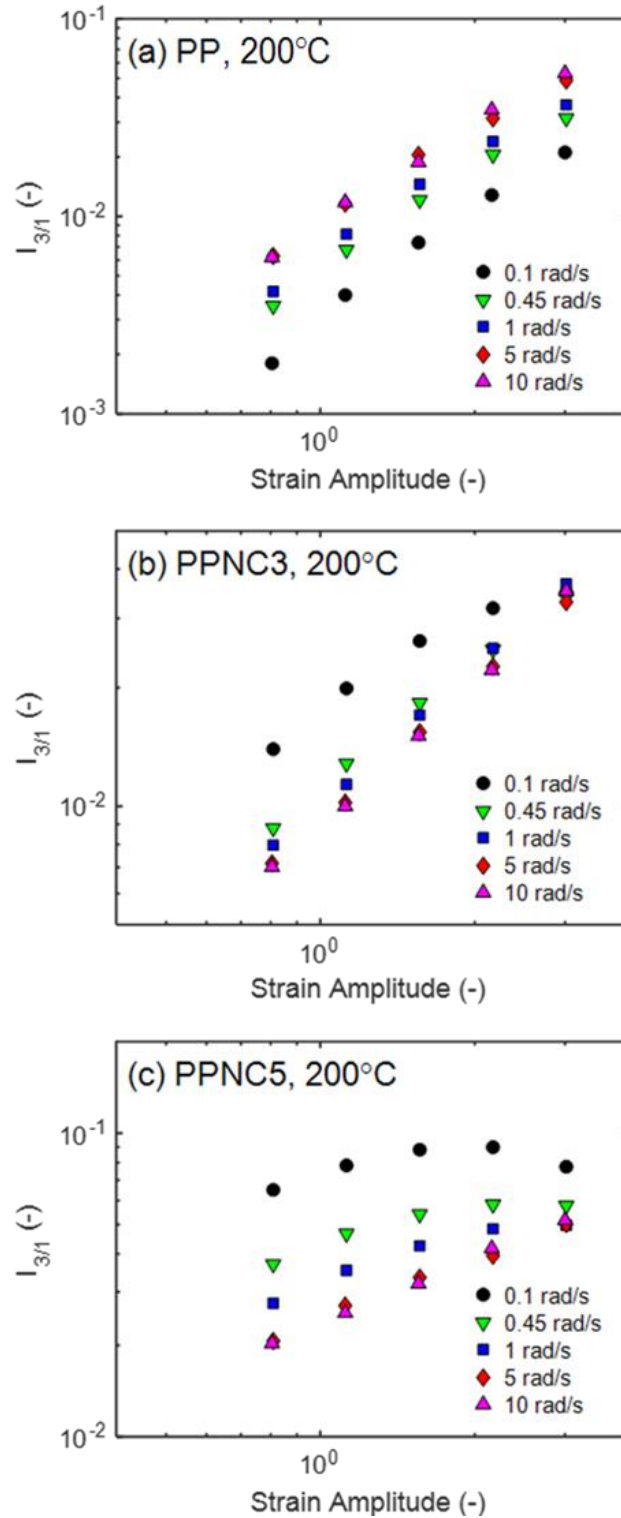


Figure 4.4 Relative third harmonic ratio against strain amplitude at various frequencies for (a) matrix (b) 3wt% clay nanocomposite and (c) 5wt% clay nanocomposite.

The value of Q defined in Equation 4.5 was determined as an intermediate step to acquire Q_0 and is presented in Figure 4.5. As consequence of the quadratic scaling in $I_{3/1}$ with strain amplitude for the matrix in Figure 4.4(a), a plateau in Q at strain amplitudes near $\gamma_0 = 0.5$ is observed for all frequencies. The monotonic value of Q is directly followed by a decrease in magnitude with increasing strain amplitude. However, only a decrease in Q with increasing strain amplitude is observed for the nanocomposites in Figure 4.5(b,c). Even over a larger strain amplitude range in Figure 4.2(c), no clear plateau in Q exists for the nanocomposites tested here due to limitations in the rheometer. When Hyun and Wilhelm[10] originally defined Q_0 they suggested that the true value was obtained by averaging the plateau region of Q over several strain amplitudes. While this was possible for monodisperse unfilled polymer systems, the lack of a plateau clearly presents a challenge for determining Q_0 in nanocomposites with strong particle-particle and particle-attached interactions. Hassanabadi et. al.[7] also did not observe a plateau in Q over several strain amplitudes for ethyl vinyl acetate nanocomposites filled with montmorillonite clay. Values of Q_0 were calculated in this work by setting it equal to the value of Q at $\gamma_0 = 0.5$ for all samples across all frequencies. These effective Q_0 values are plotted against frequency in Figure 4.6.

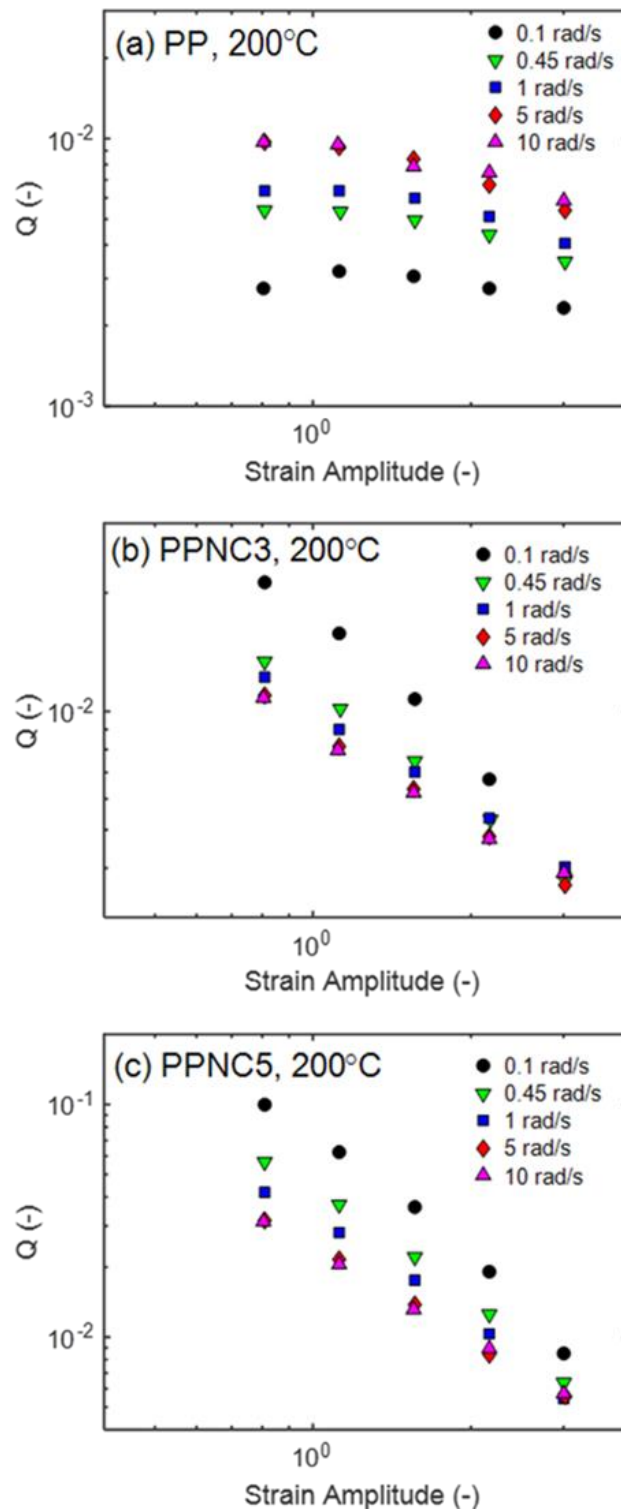


Figure 4.5 Nonlinear parameter Q against strain amplitude at various frequencies for (a) matrix (b) 3wt% clay nanocomposite and (c) 5wt% clay nanocomposite.

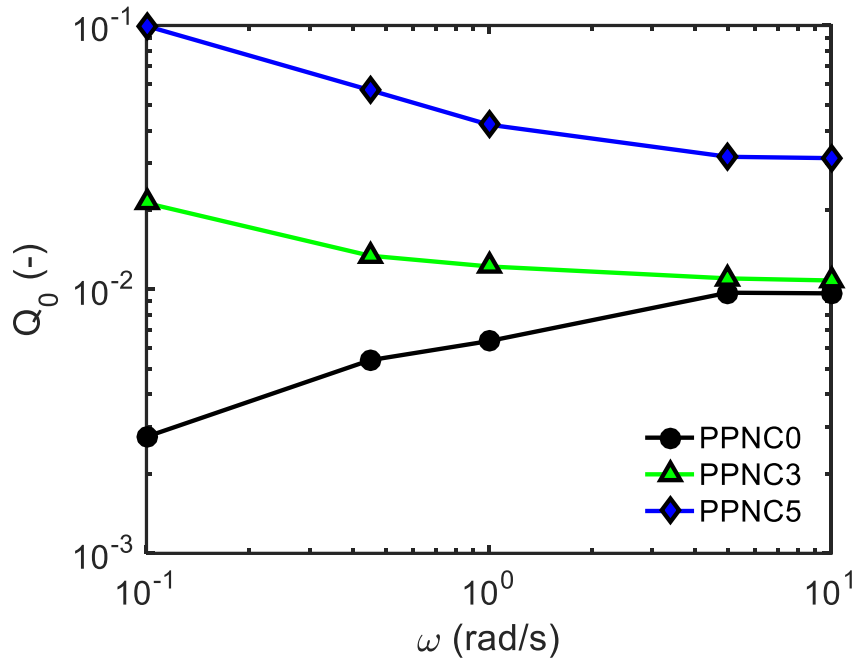


Figure 4.6 Frequency dependence of $Q_0 \equiv Q(\gamma_0=0.5)$ for nanocomposites and matrix.

While this may not be the true Q_0 value, it does provide a means for comparing the nonlinear frequency dependence between composites and the matrix. As with the trends in $I_{3/1}$, Q_0 decreases with increasing frequency while the opposite effect is observed for the matrix. Ahirwal et. al.[6] tested the frequency dependence of Q_0 for polyethylene nanocomposites filled with multiwalled carbon nanotubes and found that above the percolation threshold, Q_0 decreased with increasing frequency due to the breakup of the filler network. Without a filler network present, the decrease in Q_0 is associated to the entanglement breakup of particle-attached chains suggesting that FT rheology is sensitive to the surface treatment of the clay and reaction with compatibilizer. This is further supported by the monotonic decrease of PPNC3 towards the matrix asymptote, where only polymer-polymer entanglements exist. An increase in clay loading lead to an overall increase in Q_0 , though the trends between both nanocomposites are nearly identical.

4.4 Conclusions

Polypropylene-layered silicate nanocomposites with filler loadings below the percolation threshold were investigated under LAOS flows. Surface modification of the organically modified montmorillonite clay filler with silane treatment created reactive sites for attachment with a maleic anhydride grafted polypropylene with sufficient molecular weight to entangle with the polypropylene matrix. The resulting particle-attached chain entanglements led to an increase in the linear viscoelastic storage moduli at low frequencies suggesting a reduction in chain mobility and slower relaxation dynamics. The nonlinear response of the nanocomposites was investigated using FT rheology and quantified by the relative third harmonic ratio $I_{3/1}$ and Q_0 . In the unfilled polypropylene matrix, the $I_{3/1}$ followed a quadratic scaling with increasing strain amplitudes and increased in magnitude with increasing frequency. However, both nanocomposites displayed an $I_{3/1}$ with a power law scaling less than 2 and a decrease in the magnitude with increasing frequency. These trends resulted in Q_0 increasing with increasing frequency for the polypropylene matrix while a decrease with increasing frequency was found for both nanocomposites. This suggests that Q_0 was sensitive to the entanglement network breakup formed by the slower relaxing particle-attached chains. An increase in filler concentration also increased the magnitude of Q_0 while preserving the decrease with increasing frequency.

CHAPTER 5

EFFECTS OF REACTIVE OLIGOMER ADDITIVES ON MELT RHEOLOGY OF NYLONS: FOURIER TRANSFORM RHEOLOGY

5.1 Introduction

Successful rubber toughening of polyamide blends has been extensively studied in the literature to improve the elastomeric properties of polyamide matrix through increases in impact strength and increase in elongation at break[80, 81]. However, polyamides generally are generally incompatible with natural rubber fillers leading to poor morphological structures and reduced mechanical properties[82]. Reactive compatibilization has been frequently used to promote compatibility with the dispersed rubber phase using maleated elastomers which react with the amine end groups and create a block copolymer with increased adhesion to the rubber phase[83].

Large amplitude oscillatory shear flows combined with Fourier transform rheology is sensitive to polymer morphology and topology[5]. In the case of polymer blends, it has been used to detect the miscibility of polymer blends containing nanocomposites[19-21] as well as detecting the small morphological changes due to the addition of small droplets of a dispersed phase[84].

In this study polyamide blends reacted with an elastic oligomeric functionalized rubber are investigated under large amplitude oscillatory shear. With the rheology of polyamides suggesting a viscous dominant response, the aim of this study is to see what changes appear in the nonlinear behavior with the addition of oligomer. Fourier transform rheology and stress decomposition techniques are identified as the best techniques for quantifying this effect.

5.2 Experimental

5.2.1 Materials

Polyamide copolymer with an 80:20 wt% ratio of nylon-6 to nylon-6,6 was obtained from ExxonMobil. The copolymer was produced via a continuous polymerization process and received in pelletized form. Blends consisting of the PA copolymer with an anhydride functionalized oligomer were produced by ExxonMobil using 5 and 10 wt% oligomer. Two oligomeric polyisobutylene succinic anhydrides (PIBSA) with varying molecular weights ($M_w = 750, 1000$) were obtained by Dover Chemicals.

5.2.2 Blend Preparation

Blends consisting of 5 and 10 wt% oligomer were received from ExxonMobil after melt mixed with polyamide copolymer via extrusion and pelletized. Blends produced in lab using PIBSA were melt mixed in a Haake RheoDrive batch mixer at 80 rpm for 15 minutes with Banbury blades. Polyamide copolymer and blends were then compression molded into square molds of dimension 75x75x1 mm at 240°C in a Wabash compression molding machine. Samples were vacuum dried for 3 days before testing, to ensure all moisture was removed.

5.2.3 Dynamic Shear Rheology

Rheological measurements were performed in an ARES (TA Instruments) strain-controlled rheometer using a 25 mm parallel plate geometry. Linear viscoelastic frequency sweeps were conducted at 230°C and $\gamma_0=0.03$ from $\omega = 0.1 - 100$ rad/s at 7 frequencies per decade. Strain sweep tests extending from small angle oscillatory shear (SAOS) flows to large amplitude oscillatory shear (LAOS) flows were conducted at 230°C and 1 rad/s from $\gamma_0 = 0.05 - 5$ with 7 strains per decade and 5 cycles per strain amplitude.

5.2.4 Nonlinear Analysis

LAOS flows were interpreted using Fourier transform (FT) rheology[11, 13, 14] with a home-written MATLAB code. Data acquisition from the ARES rheometer was performed using a 16-bit resolution high-speed data acquisition (DAQ) card (PCIe-6341 X series, National Instruments) with a 100 kS/sec/channel sampling rate. The stress was Fourier transformed using the fast Fourier transform algorithm to get the higher order harmonics,

$$\sigma = \sum_{n,odd} \sigma_n \sin(n\omega t + \delta_n) \quad (5.1)$$

Where σ_n and δ_n are the Fourier intensity and phase angles corresponding to the n harmonic. The nonlinear parameter $I_{3/1} = \sigma_3/\sigma_1$ was used to determine the degree of nonlinearity.

Stress decomposition methods[16] were implemented to decompose the total stress into elastic and viscous stresses using the Fourier intensities and phase angles in Equation 5.1,

$$\sigma' = \sum_{k=0}^{\infty} \sigma_{2k+1} \cos(\delta_{2k+1}) \sin[(2k + 1)\omega t] \quad (5.2)$$

$$\sigma'' = \sum_{k=0}^{\infty} \sigma_{2k+1} \sin(\delta_{2k+1}) \cos[(2k + 1)\omega t] \quad (5.3)$$

Stress decomposition results were combined with Lissajous-Bowditch curves to qualitatively describe the nonlinear behavior.

5.3 Results and Discussion

5.3.1 Linear Viscoelasticity

The linear viscoelastic frequency sweep for polyamide blends mixed with 5 wt% and 10 wt% PIBSA oligomer is shown in Figure 5.1.

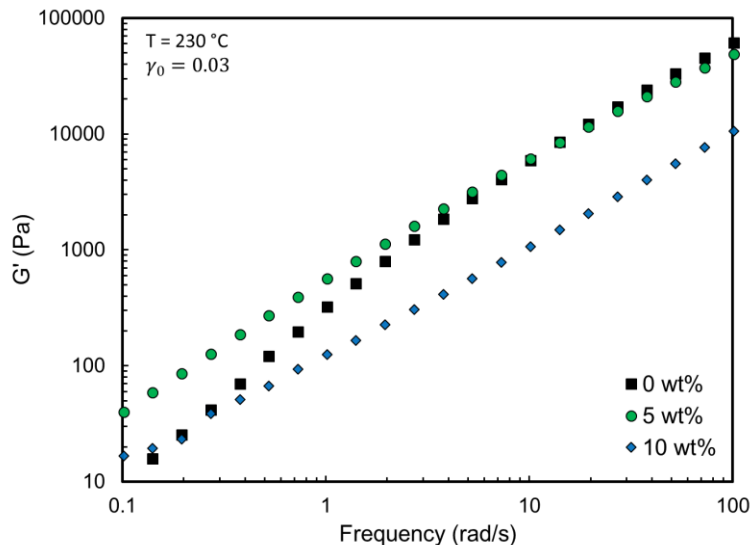


Figure 5.1 Dynamic storage modulus comparing effect of oligomer addition

The linear viscoelastic data is sensitive to the morphological changes due to the addition of oligomer. With 5 wt% oligomer addition, the polymer blend exhibits a greater solid-response to deformation, particularly at lower frequencies. This response can be attributed to the reactive compatibilization between the nylon copolymer matrix and the PIBSA oligomer. Further addition of oligomer to 10 wt % leads to an elastic modulus much less than the matrix response. While the same extent of reaction is expected, the excess PIBSA must phase separate to form a dispersed region of lower viscosity due to the low molecular weight. Nonlinear rheology was used to further classify the morphology of the system.

5.3.2 *Nonlinear Viscoelasticity*

LAOS flows were used to quantify the morphological changes through reactive compatibilization leading to observed nonlinearities in the stress. One technique is to use Lissajous plots for a qualitative inspection on the viscoelastic behavior of the stress. From linear viscoelastic experiments, the low frequency regime where $\omega = 0.1$ rad/s show the greatest variation between blends and matrix. As frequency increased, the 5 wt% blend asymptotically approached the matrix

behavior, suggesting that the oligomer slows the relaxation dynamics at low frequencies only. The Lissajous and elastic stresses determined from Equation 5.2 are presented for $\omega = 0.1$ rad/s in Figure 5.2(a) and $\omega = 1$ rad/s in Figure 5.2(b).

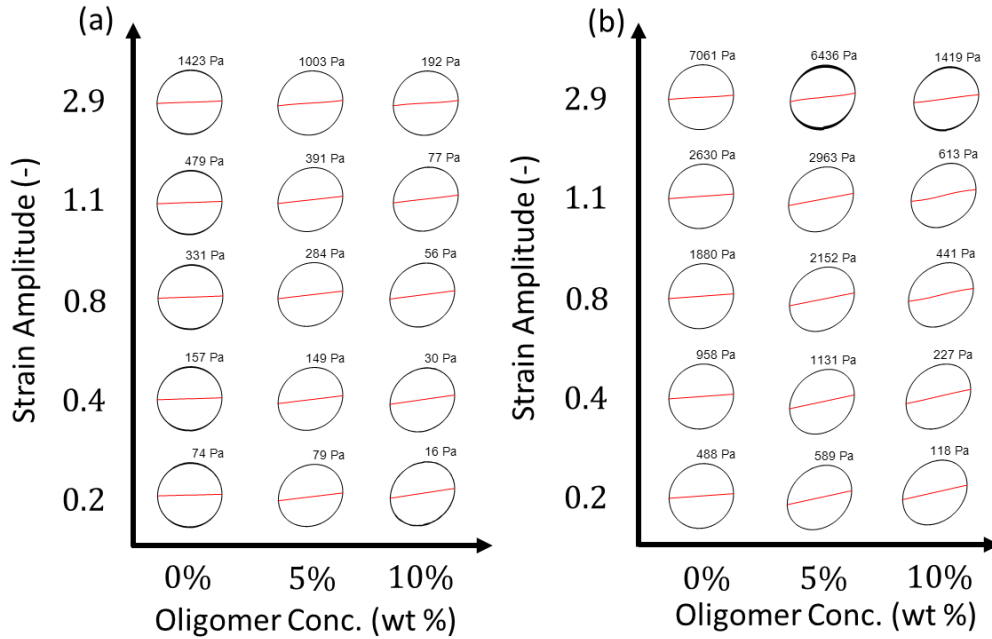


Figure 5.2 Lissajous curves with corresponding elastic stresses for varying oligomer concentration and strain amplitude at (a) $\omega = 0.1$ rad/s, and (b) $\omega = 1$ rad/s.

For both frequencies, it is clear that the elastic behavior is increased by oligomer. This is indicated by the transition to an ellipsoidal behavior in the stress waveform from a nearly viscous response by the matrix. Inspection of the elastic stress also shows this increase in elastic behavior through an increase in slope, where the matrix elastic stress is nearly flat. Though a similar elastic behavior is observed for the oligomer containing blends, the shear stress is significantly reduced for the 10 wt% case.

A quantitative analysis may be made onto the magnitude of elastic stress buildup in each system. First, the waveforms plotted in Figure 5.2 are instead mapped to the time-domain and compared in Figure 5.3.

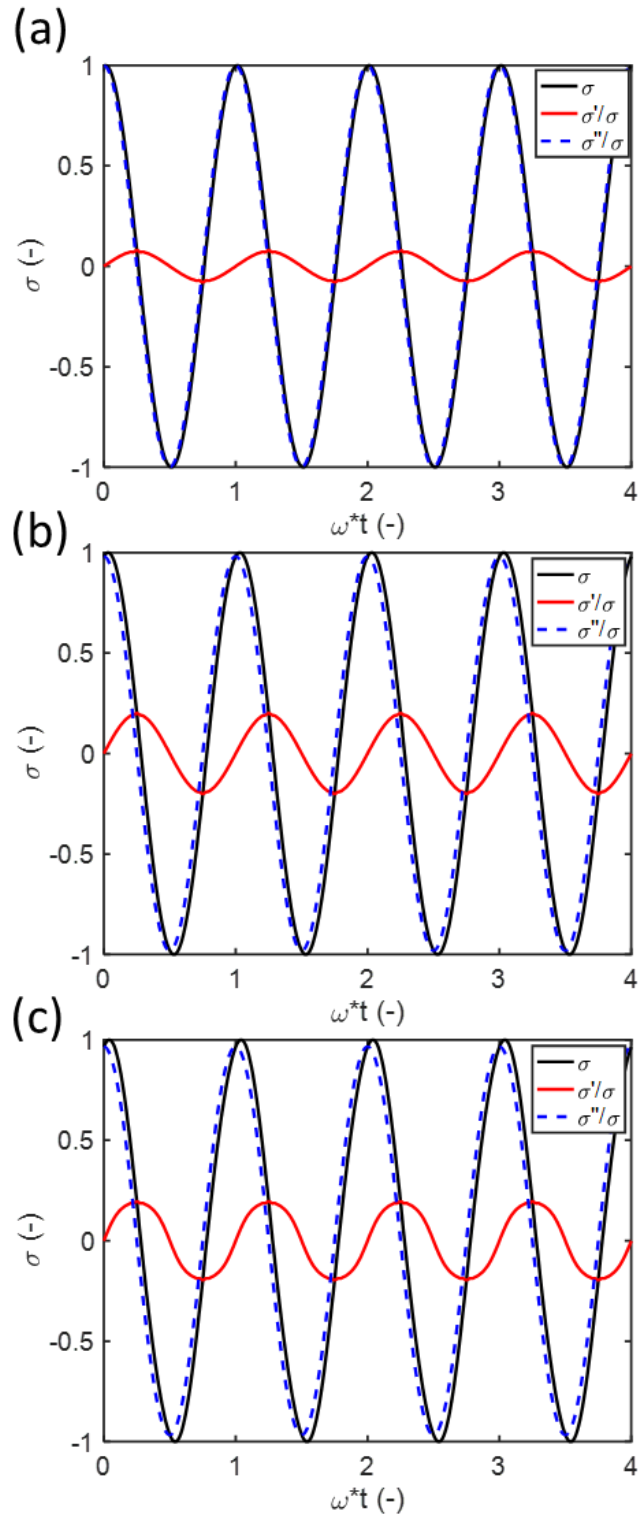


Figure 5.3 Elastic and viscous stress waveforms at $\gamma_0=1.14$ and $\omega=1$ rad/s for (a) nylon copolymer matrix (b) 5 wt% oligomer and (c) 10 wt% oligomer.

The viscous waveform in Figure 5.3 is similar to the overall shear stress waveform for all samples indicating the response is viscous dominant. It is clear that upon addition of oligomer, the elastic contribution increases over the matrix response due to the increase in elastic stress magnitude. The magnitude however, is similar between the oligomer cases though the waveforms have completely different shapes. The maximum elastic stress was determined for each material and plotted against strain amplitude for $\omega = 1$ rad/s in Figure 5.4.

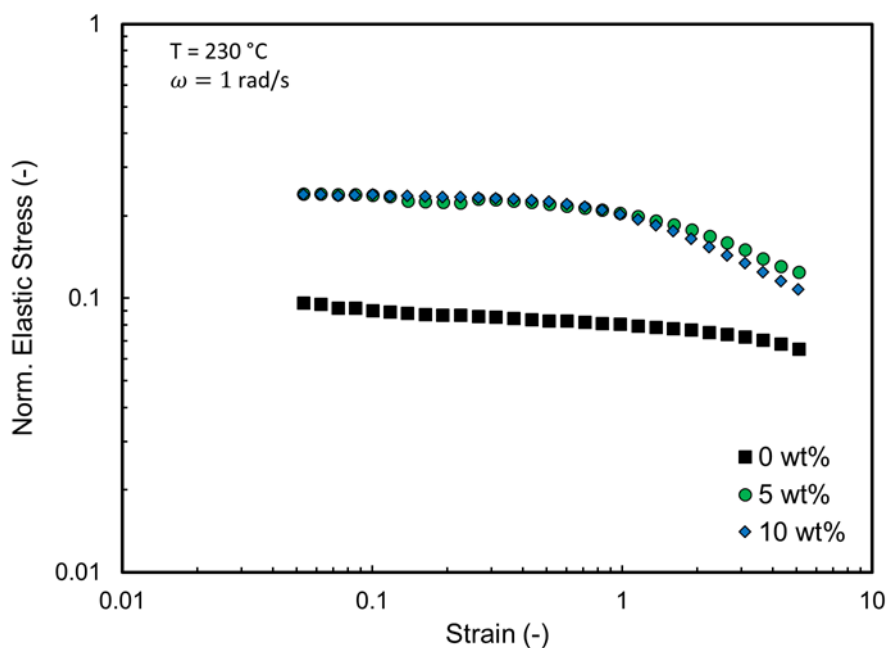


Figure 5.4 Normalized elastic stress against strain amplitude for $\omega = 1$ rad/s.

The contribution to the elastic stress is indeed greater for the oligomer containing blends. Interestingly enough, though the shear stress is significantly lower for the 10 wt% oligomer containing blend, as shown in Figure 5.2(b), the relative increase in elasticity is independent of the oligomer concentration, suggesting that it is dependent more so on the copolymer structure formed between the amide linkages formed through reactive compatibilization. More evidence is needed to determine this with certainty.

A final look into the effect that reactive compatibilization has on the nonlinear response is the influence it has on the $I_{3/1}$ parameter. This is shown for $\omega = 1$ rad/s in Figure 5.5.

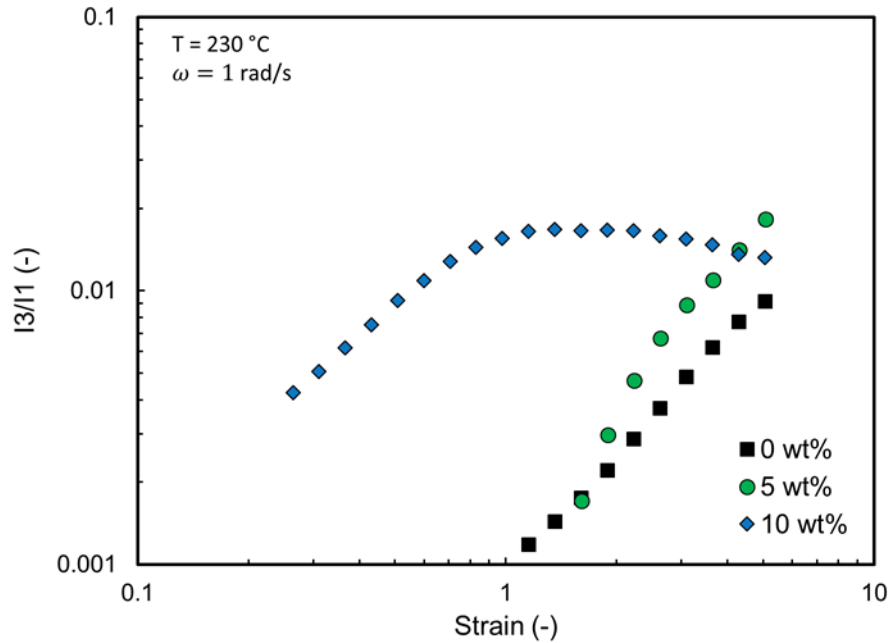


Figure 5.5 Effect of oligomer addition on the nonlinear $I_{3/1}$ parameter for $\omega = 1$ rad/s.

The most pronounced effect the oligomer addition has on the nonlinearity is observed through the $I_{3/1}$ parameter. A slight increase is observed in the nonlinearity for 5 wt% oligomer addition, though the dependence on strain is the same. At this point it has been speculated that the 10 wt% oligomer containing blends were fully reacted to the nylon copolymer, leaving excess oligomer available to phase separate. If this is indeed the case, then the $I_{3/1}$ shows a remarkable sensitivity to the dispersed oligomer phase, leading to an earlier onset of nonlinearity. The plateau region in $I_{3/1}$ extends through a wide strain amplitude range suggesting that the dispersed phase is unable to contribute beyond $\gamma_0 = 1$. Reasons for this are still unexplained. Though it is clear that the degree of reactive compatibilization can in some way be quantified using LAOS.

5.4 Conclusions and Recommendations

The effect of reactive compatibilization of nylon copolymer with an elastomeric PIBSA oligomer was investigated using LAOS flows. Fourier transform rheology and stress decomposition techniques showed that while an excess of oligomer led to the lowest shear stress, the relative elasticity was independent of the oligomer concentration. This suggests that the elastic stress was dominated by the amide linkages formed in the matrix phase and had no dependence on the potential dispersed phase. The suggestion that a dispersed phase exists was concluded by remarkable differences in the nonlinear $I_{3/1}$ parameter, where excess oligomer led to an earlier onset of nonlinearity and a greater nonlinear over a wide range of strain amplitudes. Suggestions for this research include the direct testing of amide linkages either through FT-IR methods or titration techniques. This should answer if there is indeed an excess amount of oligomer present. Further suggestions would include the imaging of these blends to determine if regions of phase separation are observable.

CONCLUSIONS AND RECOMMENDATIONS

6.1 Conclusions

This research focused on investigating the nonlinear rheology of complex fluids using large amplitude oscillatory shear (LAOS) flows. These flows were analyzed using several techniques including: Lissajous-Bowditch curves to plot stress versus strain waveforms, Fourier transform rheology to determine higher harmonic contributions to the stress, and stress decomposition to evaluate the elastic and viscous stress contributions in the nonlinear regime.

The rheological properties associated with polymer nanocomposites can be directly related to both the microstructure as well as the type of interactions present in the system. Three types of interactions are possible in nanocomposites: particle-particle, particle-polymer, and polymer-polymer. The particle-particle interactions are dependent on the size and concentration of the filler phase. For highly loaded nanocomposites, a critical concentration is reached, known as the percolation threshold, for which a filler network forms. The filler network is known to dominate the rheology through elastic (solid-like) responses. However, the processing range of these systems is limited since at large deformations the filler network breaks down leading to a transition into the nonlinear regime. The breakdown of the filler network with increasing deformations is known as the Payne effect.

When nanocomposites are surface treated to promote compatibility with the matrix chains, stronger particle-polymer interactions dominate the rheology. These interactions lead to hindered chain mobility near the interface of the filler, resulting in slower relaxation times and an increase in the viscoelastic moduli at low frequencies. Consequently, the improved interactions between

the polymer matrix and the filler particles lead to increases in the nanocomposite properties such as improved mechanical strength, barrier properties and strain hardening behavior. These improvements also require less filler due to the strong entanglement networks which form between particle-attached chains and the polymer matrix chains. As with the breakdown of the filler network, the entanglement network formed by the slower relaxing particle-attached chains can also break down, leading to a similar Payne effect response.

The dynamics of these dilute nanocomposites containing strong entanglement networks with particle attached chains was a major subject in this work. Fourier transform rheology on LAOS flows has been shown throughout the literature as a very sensitive method to determine polymer morphology, microstructure, and relaxation dynamics. However, relating the trends found in nonlinear rheology to the dynamics of the tested material has always been a major challenge. This motivated the development of the nonlinear viscoelastic model for polymer nanocomposites presented in this work. Relating linear relaxation mechanisms (double reptation) and nonlinear relaxation mechanisms (convective constraint release and chain retraction) to trends observed in FT rheology resulted in a way to describe the nonlinearities in terms of chain dynamics.

Three nonlinear parameters in FT rheology were used to quantify the effect of entanglement networks formed by particle-attached chains: the relative third harmonic $I_{3/1}$, the nonlinear parameter Q and the zero-strain intrinsic nonlinearity Q_0 . Through numerical simulations and asymptotic expressions, the predicted nonlinearities in the viscoelastic nanocomposite constitutive model were explored. The nonlinear behavior was found to be dependent on three parameters: the strength of attachment (i.e. slower particle-attached reptation dynamics), the volume fraction of attached chains, and the CCR parameter.

Convective constraint release had been previously derived in an effort to prevent constitutive models from over predicting the shear thinning behavior at larger shear rates. Since this mechanism depends on the flow rate, it was uniformly applied to all polymer chains present in a system resulting in the same stress relaxation, regardless of the polymer architecture or attachment to nanoparticles. Thus, the idea of independent CCR parameters was introduced here so as to allow faster removal of entanglements made with particle-attached chains. Only when the CCR rate of particle-attached chains is larger than the free matrix chains, do the trends in the nonlinear parameters, particular Q_0 , match with experiment.

Large amplitude oscillatory shear tests on polypropylene layered-silicate nanocomposites were conducted to test the validity of the model presented in this work. Particle-attached chains were created using a silane treated montmorillonite nanoclay reacted with a maleic anhydride grafted polypropylene. The PP-g-MA was of substantial molecular weight to extend into the PP matrix and form multiple entanglements. The reduced chain mobility due to attachment with the nanoclay was confirmed through linear viscoelastic frequency sweeps. There, an increase in the viscoelastic moduli at low frequencies was reported for nanocomposites containing both 3 and 5 wt% in a 1:1 PP-g-MA : clay ratio. Nanocomposites were subjected to multiple frequencies over a range of strain amplitudes extending well into the nonlinear region. As predicted by the viscoelastic model, the polypropylene nanocomposites experienced a decrease in nonlinearity with increasing frequency, characterized by a decrease in both $I_{3/1}$ and Q_0 . The unfilled matrix showed the opposite trend, having an increase in nonlinearity with increasing frequency. This implied that the hindered chain mobility led to an earlier breakup of the particle-attached entanglement network resulting in a nonlinear response that was governed by polymer-polymer interactions alone.

The final project was concerned with the reactive compatibilization of an elastomeric oligomer, PIBSA, with nylon copolymer. The nylon copolymer was found to have a viscous dominant response in its rheology. However, due to the elastic nature of PIBSA, it was speculated that the reaction with nylon would in some way impart some elastic behavior to the resulting blend. These blends were characterized using LAOS flows combined with FT rheology and stress decomposition methods. The stress decomposition showed that an equivalent elastic response was observed, independent of the oligomer concentration. However, the decrease in shear stress for the largest oligomer concentration of 10 wt% implied that excess oligomer was phase separated from the blend. Upon inspection of the $I_{3/1}$ parameter, the 5 wt% and nylon copolymer had similar magnitudes in their nonlinearity; the strain amplitude onset of nonlinearity was also comparable. However, in the presence of excess oligomer, the 10 wt% case had the largest $I_{3/1}$ magnitude with an onset of nonlinearity an order of magnitude earlier than the other cases. This suggested that FT rheology was sensitive to the morphology of polymer blends and could be used to determine at what concentration phase separation would occur.

6.2 Recommendations

The present work has explored the dynamics of polymer nanocomposites in both a theoretical and experimental framework for LAOS flows. One of the most useful parameters in describing the relaxation and breakup of the particle-attached entanglement network is the zero-strain intrinsic nonlinearity, Q_0 . This parameter is a frequency dependent parameter, though acquiring it experimentally is tedious. Strain sweep tests from medium to large amplitudes must be performed for many frequencies if a high resolution Q_0 curve is desired. Each test requires a new sample, which can be challenging if the material is only available in low quantities. Therefore, a recommendation is to investigate nonlinear frequency sweeps as a way to evaluate the relaxation

phenomena. Most LAOS setups are unable to accomplish this task due to the “on-the-fly” oversampling of the stress and strain waveforms. Since oversampling depends on the excitation frequency, most LAOS frameworks are unable to change the oversampling number “on-the-fly”. However, by oversampling after the experiment is complete as is done in this work, proper oversampling can be done on the waveforms acquired from a large amplitude frequency sweep test.

BIBLIOGRAPHY

BIBLIOGRAPHY

1. Graessley, W.W., *Polymer liquids and networks: structure and properties*. 2003, New York, NY: Garland Science.
2. Graessley, W.W., *Polymeric liquids and networks: dynamics and rheology*. 2003, New York, NY: Garland Science.
3. Giacomin, A.J. and J.M. Dealy, *Using large-amplitude oscillatory shear*, in *Rheological Measurement*, A.A. Collyer and D.W. Clegg, Editors. 1998, Springer Netherlands: Dordrecht. p. 327-356.
4. Hyun, K., S.H. Kim, K.H. Ahn, and S.J. Lee, *Large amplitude oscillatory shear as a way to classify the complex fluids*. *J. Non-Newtonian Fluid Mech.*, 2002. **107**(1-3): p. 51-65.
5. Hyun, K., M. Wilhelm, C.O. Klein, K.S. Cho, J.G. Nam, K.H. Ahn, S.J. Lee, R.H. Ewoldt, and G.H. McKinley, *A review of nonlinear oscillatory shear tests: Analysis and application of large amplitude oscillatory shear (LAOS)*. *Prog. Polym. Sci.*, 2011. **36**(12): p. 1697-1753.
6. Ahirwal, D., H. Palza, G. Schlatter, and M. Wilhelm, *New way to characterize the percolation threshold of polyethylene and carbon nanotube polymer composites using Fourier transform (FT) rheology*. *Korea-Aust. Rheol. J.*, 2014. **26**(3): p. 319-326.
7. Hassanabadi, H.M., M. Wilhelm, and D. Rodrigue, *A rheological criterion to determine the percolation threshold in polymer nano-composites*. *Rheol. Acta*, 2014. **53**(10-11): p. 869-882.
8. Hoyle, D.M., D. Auhl, O.G. Harlen, V.C. Barroso, M. Wilhelm, and T.C.B. McLeish, *Large amplitude oscillatory shear and Fourier transform rheology analysis of branched polymer melts*. *J. Rheol.*, 2014. **58**(4): p. 969-997.
9. Hyun, K., W. Kim, S.J. Park, and M. Wilhelm, *Numerical simulation results of the nonlinear coefficient Q from FT-Rheology using a single mode pom-pom model*. *J. Rheol.*, 2013. **57**(1): p. 1-25.
10. Hyun, K. and M. Wilhelm, *Establishing a new mechanical nonlinear coefficient Q from FT-rheology: first investigation of entangled linear and comb polymer model systems*. *Macromolecules*, 2009. **42**(1): p. 411-422.
11. van Dusschoten, D. and M. Wilhelm, *Increased torque transducer sensitivity via oversampling*. *Rheol. Acta*, 2001. **40**(4): p. 395-399.
12. Wagner, M.H., V.H. Rolón-Garrido, K. Hyun, and M. Wilhelm, *Analysis of medium amplitude oscillatory shear data of entangled linear and model comb polymers*. *J. Rheol.*, 2011. **55**(3): p. 495-516.

13. Wilhelm, M., *Fourier-transform rheology*. Macromol. Mater. Eng., 2002. **287**(2): p. 83-105.
14. Wilhelm, M., P. Reinheimer, and M. Ortseifer, *High sensitivity Fourier-transform rheology*. Rheol. Acta, 1999. **38**(4): p. 349-356.
15. Cho, K.S., K. Hyun, K.H. Ahn, and S.J. Lee, *A geometrical interpretation of large amplitude oscillatory shear response*. J. Rheol., 2005. **49**(3): p. 747-758.
16. Cho, K.S., K.W. Song, and G.S. Chang, *Scaling relations in nonlinear viscoelastic behavior of aqueous PEO solutions under large amplitude oscillatory shear flow*. J. Rheol., 2010. **54**(1): p. 27-63.
17. Ewoldt, R.H., A.E. Hosoi, and G.H. McKinley, *New measures for characterizing nonlinear viscoelasticity in large amplitude oscillatory shear*. J. Rheol., 2008. **52**(6): p. 1427-1458.
18. Du, L., M. Namvari, and F.J. Stadler, *Large amplitude oscillatory shear behavior of graphene derivative/polydimethylsiloxane nanocomposites*. Rheol. Acta, 2018. **57**(5): p. 429-443.
19. Salehiyan, R., H.Y. Song, W.J. Choi, and K. Hyun, *Characterization of effects of silica nanoparticles on (80/20) PP/PS blends via nonlinear rheological properties from Fourier transform rheology*. Macromolecules, 2015. **48**(13): p. 4669-4679.
20. Salehiyan, R., H.Y. Song, and K. Hyun, *Nonlinear behavior of PP/PS blends with and without clay under large amplitude oscillatory shear (LAOS) flow*. Korea-Aust. Rheol. J., 2015. **27**(2): p. 95-103.
21. Salehiyan, R., Y. Yoo, W.J. Choi, and K. Hyun, *Characterization of morphologies of compatibilized polypropylene/polystyrene blends with nanoparticles via nonlinear rheological properties from FT-rheology*. Macromolecules, 2014. **47**(12): p. 4066-4076.
22. Hassanabadi, H.M., M. Abbasi, M. Wilhelm, and D. Rodrigue, *Validity of the modified molecular stress function theory to predict the rheological properties of polymer nanocomposites*. J. Rheol., 2013. **57**(3): p. 881-899.
23. Leblanc, J.L., *Large amplitude oscillatory shear experiments to investigate the nonlinear viscoelastic properties of highly loaded carbon black rubber compounds without curatives*. J. Appl. Polym. Sci., 2008. **109**(2): p. 1271-1293.
24. Leblanc, J.L., *Modeling the strain dependence of torque harmonics as measured through large-amplitude oscillatory shear rheometry*. J. Appl. Polym. Sci., 2012. **126**(2): p. 663-677.
25. Lim, H.T., K.H. Ahn, J.S. Hong, and K. Hyun, *Nonlinear viscoelasticity of polymer nanocomposites under large amplitude oscillatory shear flow*. J. Rheol., 2013. **57**(3): p. 767-789.

26. Dealy, J.M. and R.G. Larson, *Structure and rheology of molten polymers from polymerization to processability via rheology*. 2006, Cincinnati: Hanser Gardner Publications. xiv, 516 p.
27. Degennes, P.G., *KINETICS OF DIFFUSION-CONTROLLED PROCESSES IN DENSE POLYMER SYSTEMS .2. EFFECTS OF ENTANGLEMENTS*. Journal of Chemical Physics, 1982. **76**(6): p. 3322-3326.
28. Doi, M. and S.F. Edwards, *Dynamics of concentrated polymer systems. Part 1.-Brownian motion in the equilibrium state*. J. Chem. Soc., Faraday Trans. 2, 1978. **74**(0): p. 1789-1801.
29. Doi, M. and S.F. Edwards, *Dynamics of concentrated polymer systems. Part 2.-Molecular motion under flow*. J. Chem. Soc., Faraday Trans. 2, 1978. **74**(0): p. 1802-1817.
30. Doi, M. and S.F. Edwards, *Dynamics of concentrated polymer systems. Part 3.-The constitutive equation*. J. Chem. Soc., Faraday Trans. 2, 1978. **74**(0): p. 1818-1832.
31. Doi, M. and S.F. Edwards, *Dynamics of concentrated polymer systems. Part 4.-Rheological properties*. J. Chem. Soc., Faraday Trans. 2, 1979. **75**(0): p. 38-54.
32. Ianniruberto, G. and G. Marrucci, *Convective constraint release (CCR) revisited*. J. Rheol., 2014. **58**(1): p. 89-102.
33. Krishnamoorti, R., I. Banik, and L. Xu, *Rheology and processing of polymer nanocomposites*. Rev. Chem. Eng., 2010. **26**(1-2): p. 3-12.
34. Sinha Ray, S. and M. Okamoto, *Polymer/layered silicate nanocomposites: a review from preparation to processing*. Progress in Polymer Science, 2003. **28**(11): p. 1539-1641.
35. Cassagnau, P., *Linear viscoelasticity and dynamics of suspensions and molten polymers filled with nanoparticles of different aspect ratios*. Polymer, 2013. **54**(18): p. 4762-4775.
36. T.A. Vilgis, G.H., M. Klüppel, *Reinforcement of polymer nano-composites : theory, experiments and applications* 2009, New York: Cambridge University Press.
37. Krishnamoorti, R. and E.P. Giannelis, *Rheology of end-tethered polymer layered silicate nanocomposites*. Macromolecules, 1997. **30**(14): p. 4097-4102.
38. Ren, W.J., A.K. Chaudhary, and K. Jayaraman, *Processing polypropylene nanocomposites with silylated organoclays: coupling at edges versus gallery faces*. Ind. Eng. Chem. Res., 2015. **54**(16): p. 4264-4273.
39. Ren, J.X. and R. Krishnamoorti, *Nonlinear viscoelastic properties of layered-silicate-based intercalated nanocomposites*. Macromolecules, 2003. **36**(12): p. 4443-4451.
40. Cassagnau, P., *Payne effect and shear elasticity of silica-filled polymers in concentrated solutions and in molten state*. Polymer, 2003. **44**(8): p. 2455-2462.

41. Hyun, K., S. Höfl, S. Kahle, and M. Wilhelm, *Polymer motion as detected via dielectric spectra of 1,4-cis-polyisoprene under large amplitude oscillatory shear (LAOS)*. *J. Non-Newtonian Fluid Mech.*, 2009. **160**(2): p. 93-103.
42. Hassanabadi, H.M. and D. Rodrigue, *Relationships between linear and nonlinear shear response of polymer nano-composites*. *Rheol. Acta*, 2012. **51**(11-12): p. 991-1005.
43. Ewoldt, R.H., *Nonlinear viscoelastic materials: bioinspired applications and new characterization measures*, in *Mechanical Engineering*. 2009, Massachusetts Institute of Technology.
44. Giacomini, A.J., P.H. Gilbert, D. Merger, and M. Wilhelm, *Large-amplitude oscillatory shear: comparing parallel-disk with cone-plate flow*. *Rheol. Acta*, 2015. **54**(4): p. 263-285.
45. Klein, C.O., H.W. Spiess, A. Calin, C. Balan, and M. Wilhelm, *Separation of the nonlinear oscillatory response into a superposition of linear, strain hardening, strain softening, and wall slip response*. *Macromolecules*, 2007. **40**(12): p. 4250-4259.
46. Cassagnau, P., *Melt rheology of organoclay and fumed silica nanocomposites*. *Polymer*, 2008. **49**(9): p. 2183-2196.
47. Xu, L., H. Nakajima, E. Manias, and R. Krishnamoorti, *Tailored nanocomposites of polypropylene with layered silicates*. *Macromolecules*, 2009. **42**(11): p. 3795-3803.
48. Aranguren, M.I., E. Mora, J.J.V. DeGroot, and C.W. Macosko, *Effect of reinforcing fillers on the rheology of polymer melts*. *J. Rheol.*, 1992. **36**(6): p. 1165-1182.
49. Vermant, J., S. Ceccia, M.K. Dolgovskij, P.L. Maffettone, and C.W. Macosko, *Quantifying dispersion of layered nanocomposites via melt rheology*. *J. Rheol.*, 2007. **51**(3): p. 429-450.
50. Bailly, M. and M. Kontopoulou, *Linear viscoelastic properties of ethylene-octene copolymer/nanosilica composites investigated over a broad range of frequencies*. *Journal of Rheology*, 2013. **57**(2): p. 407-426.
51. Bailly, M., M. Kontopoulou, and K. El Mabrouk, *Effect of polymer/filler interactions on the structure and rheological properties of ethylene-octene copolymer/nanosilica composites*. *Polymer*, 2010. **51**(23): p. 5506-5515.
52. Holt, A.P., V. Bocharova, S. Cheng, A.M. Kisliuk, B.T. White, T. Saito, D. Uhrig, J.P. Mahalik, R. Kumar, A.E. Imel, T. Etampawala, H. Martin, N. Sikes, B.G. Sumpter, M.D. Dadmun, and A.P. Sokolov, *Controlling interfacial dynamics: covalent bonding versus physical adsorption in polymer nanocomposites*. *ACS Nano*, 2016. **10**(7): p. 6843-6852.
53. Holt, A.P., P.J. Griffin, V. Bocharova, A.L. Agapov, A.E. Imel, M.D. Dadmun, J.R. Sangoro, and A.P. Sokolov, *Dynamics at the polymer/nanoparticle interface in poly(2-vinylpyridine)/silica nanocomposites*. *Macromolecules*, 2014. **47**(5): p. 1837-1843.

54. Holt, A.P., J.R. Sangoro, Y.Y. Wang, A.L. Agapov, and A.P. Sokolov, *Chain and segmental dynamics of poly(2-vinylpyridine) nanocomposites*. *Macromolecules*, 2013. **46**(10): p. 4168-4173.
55. Sarvestani, A.S., *Modeling the solid-like behavior of entangled polymer nanocomposites at low frequency regimes*. *Eur. Polym. J.*, 2008. **44**(2): p. 263-269.
56. Orr, C.A., J.J. Cernohous, P. Guegan, A. Hirao, H.K. Jeon, and C.W. Macosko, *Homogeneous reactive coupling of terminally functional polymers*. *Polymer*, 2001. **42**(19): p. 8171-8178.
57. Shi, H.Z., T. Lan, and T.J. Pinnavaia, *Interfacial effects on the reinforcement properties of polymer-organoclay nanocomposites*. *Chem. Mater.*, 1996. **8**(8): p. 1584-1587.
58. Sternstein, S.S. and A.J. Zhu, *Reinforcement mechanism of nanofilled polymer melts as elucidated by nonlinear viscoelastic behavior*. *Macromolecules*, 2002. **35**(19): p. 7262-7273.
59. Fan, Y.R. and H.Y. Liao, *Experimental studies on the relaxation behavior of commercial polymer melts*. *J. Appl. Polym. Sci.*, 2008. **110**(3): p. 1520-1530.
60. Marrucci, G. and G. Ianniruberto, *Flow-induced orientation and stretching of entangled polymers*. *Philos. Trans. R. Soc. A*, 2003. **361**(1805): p. 677-687.
61. Sarvestani, A.S., *On the emergence of the Payne effect in polymer melts reinforced with nanoparticles*. *Macromol. Theory Simul.*, 2016. **25**(3): p. 312-321.
62. Warner, H.R., *Kinetic-theory and rheology of dilute suspensions of finitely extendible dumbbells*. *Ind. Eng. Chem. Fund.*, 1972. **11**(3): p. 379-387.
63. Hyun, K., E.S. Baik, K.H. Ahn, S.J. Lee, M. Sugimoto, and K. Koyama, *Fourier-transform rheology under medium amplitude oscillatory shear for linear and branched polymer melts*. *J. Rheol.*, 2007. **51**(6): p. 1319-1342.
64. Akcora, P., H. Liu, S.K. Kumar, J. Moll, Y. Li, B.C. Benicewicz, L.S. Schadler, D. Acehan, A.Z. Panagiotopoulos, V. Pryamitsyn, V. Ganesan, J. Ilavsky, P. Thiyagarajan, R.H. Colby, and J.F. Douglas, *Anisotropic self-assembly of spherical polymer-grafted nanoparticles*. *Nat. Mater.*, 2009. **8**(4): p. 354-U121.
65. Okamoto, M., P.H. Nam, P. Maiti, T. Kotaka, N. Hasegawa, and A. Usuki, *A house of cards structure in polypropylene/clay nanocomposites under elongational flow*. *Nano Letters*, 2001. **1**(6): p. 295-298.
66. Choi, Y.Y., S.H. Lee, and S.H. Ryu, *Effect of silane functionalization of montmorillonite on epoxy/montmorillonite nanocomposite*. *Polymer Bulletin*, 2009. **63**(1): p. 47-55.
67. Herrera, N.N., J.-M. Letoffe, J.-P. Reymond, and E. Bourgeat-Lami, *Silylation of laponite clay particles with monofunctional and trifunctional vinyl alkoxysilanes*. *J. Mater. Chem.*, 2005. **15**(8): p. 863-871.

68. Manitiu, M., S. Horsch, E. Gulari, and R.M. Kannan, *Role of polymer-clay interactions and nano-clay dispersion on the viscoelastic response of supercritical CO₂ dispersed polyvinylmethylether (PVME)-Clay nanocomposites*. *Polymer*, 2009. **50**(15): p. 3786-3796.
69. Risse, S., L. Tighzert, F. Berzin, and B. Vergnes, *Microstructure, rheological behavior, and properties of poly(lactic acid)/poly(butylene succinate)/organoclay nanocomposites*. *J. Appl. Polym. Sci.*, 2014. **131**(12): p. 8.
70. Singh, S., A.K. Ghosh, S.N. Maiti, S. Raha, R.K. Gupta, and S. Bhattacharya, *Morphology and rheological behavior of polylactic acid/clay nanocomposites*. *Polym. Eng. Sci.*, 2012. **52**(1): p. 225-232.
71. Alexandre, M. and P. Dubois, *Polymer-layered silicate nanocomposites: preparation, properties and uses of a new class of materials*. *Mater. Sci. Eng. R.*, 2000. **28**(1): p. 1-63.
72. Ghanbari, A., M.-C. Heuzey, P. Carreau, and M.-T. Ton-That, *Morphological and rheological properties of PET/clay nanocomposites*. *Rheol. Acta*, 2013. **52**(1): p. 59-74.
73. Zha, W.B., C.D. Han, H.C. Moon, S.H. Han, D.H. Lee, and J.K. Kim, *Exfoliation of organoclay nanocomposites based on polystyrene-block-polyisoprene-block-poly(2-vinylpyridine) copolymer: Solution blending versus melt blending*. *Polymer*, 2010. **51**(4): p. 936-952.
74. Heinz, H., R.A. Vaia, R. Krishnamoorti, and B.L. Farmer, *Self-assembly of alkylammonium chains on montmorillonite: effect of chain length, head group structure, and cation exchange capacity*. *Chem. of Mater.*, 2007. **19**(1): p. 59-68.
75. Ren, W.J., *Effects of additives on rheology and film blowing of polypropylene/clay nanocomposites*, in *Chemical Engineering and Materials Science*. 2016, Michigan State University.
76. Pearson, D.S. and W.E. Rochefort, *Behavior of concentrated polystyrene solutions in large-amplitude oscillating shear fields*. *J. Polym. Sci. Polym. Phys. Ed.*, 1982. **20**(1): p. 83-98.
77. Hyun, K., K.H. Ahn, S.J. Lee, M. Sugimoto, and K. Koyama, *Degree of branching of polypropylene measured from Fourier-transform rheology*. *Rheol. Acta*, 2006. **46**(1): p. 123-129.
78. Nam, J.G., K.H. Ahn, S.J. Lee, and K. Hyun, *Strain stiffening of non-colloidal hard sphere suspensions dispersed in Newtonian fluid near liquid-and-crystal coexistence region*. *Rheol. Acta*, 2011. **50**(11): p. 925-936.
79. Liu, J., W. Yu, W. Zhou, and C. Zhou, *Control on the topological structure of polyolefin elastomer by reactive processing*. *Polymer*, 2009. **50**(2): p. 547-552.
80. Oshinski, A.J., H. Keskkula, and D.R. Paul, *Rubber toughening of polyamides with functionalized block copolymers .I. nylon-6* *Polymer*, 1992. **33**(2): p. 268.

81. Oshinski, A.J., H. Keskkula, and D.R. Paul, *The role of matrix molecular weight in rubber toughened nylon 6 blends .I. morphology* Polymer, 1996. **37**(22): p. 4891.
82. Tanrattanakul, V., N. Sungthong, and P. Raksa, *Rubber toughening of nylon 6 with epoxidized natural rubber*. Polymer Testing, 2008. **27**(7): p. 794-800.
83. Ahn, Y.C. and D.R. Paul, *Rubber toughening of nylon 6 nanocomposites*. Polymer, 2006. **47**(8): p. 2830.
84. Carotenuto, C., M. Grosso, and P.L. Maffettone, *Fourier transform rheology of dilute immiscible polymer blends: a novel procedure to probe blend morphology*. Macromolecules, 2008. **41**(12): p. 4492-4500.